Études par spectroscopie Raman polarisée des effets photoélectrostrictifs dans LiNbO3 photoréfractif

Ninel Kokanyan

Laboratoire
Matériaux Optiques, Photonique et Systèmes
Ecole Doctorale EMMA

THÈSE

Pour l'obtention du titre de :

DOCTEUR de L'UNIVERSITÉ DE LORRAINE

Spécialité : Physique

Présentée par :

NINEL KOKANYAN

Etudes par spectroscopie Raman polarisée des effets photo-électrostrictifs dans $LiNbO_3$ photoréfractif

---

Thèse soutenue publiquement le 30 janvier 2015 à Metz devant le jury composé de :

M. Mimoun EL MARSSI – Professeur à l'Université de Picardie Jules Verne……...Rapporteur
M. Yannick MUGNIER – Maître de Conférences, HDR à l'Université de Savoie Chambéry Annecy..Rapporteur
M. Bouchta SAHRAOUI – Professeur à l'Université d'Angers……Examinateur
M. Guilhem SIMON – Maître de Conférences à l'Université Pierre et Marie Curie……Examinateur
M. Marco BAZZAN – Maître de Conférences à l'Université de Padoue……Invité
M. Michel AILLERIE – Professeur à l'Université de Lorraine……Invité
M. David CHAPRON – Maître de Conférences à l'Université de Lorraine……Co-directeur de thèse
M. Marc FONTANA - Professeur à l'Université de Lorraine……...Directeur de thèse

---

LMOPS, Supélec – 2 rue Edouard Belin, 57070 METZ, FRANCE

Table of contents

Introduction

In laser physics, particularly in photonics, new materials with improved characteristics are required. In the list of commonly used materials leading position occupy the oxide crystals among which especially highlight the multifunctional crystals with optical, nonlinear optical and other properties. Among these crystals, Lithium Niobate ($LiNbO_3$, LN) is one of the mainly used due to its various applications in optics and quantum electronics.

Lithium Niobate shows one remarkable property, namely photorefractivity, which appears under the illumination with visible or near-infrared light and leads to semi-permanent changes in the index of refraction of the crystal. As known, the dominant mechanism of the photorefraction in $LiNbO_3$ is the bulk photovoltaic effect. Therefore, the photorefractive properties of $LiNbO_3$ in the first instance are defined by the presence of photovoltaic-active ions, belonging to multi-charge transition metal impurities, mainly Fe, as well as Cu, Mn, Ni, etc.

By contrast, the photorefractive property is the main drawback for electro-optics and frequency conversion applications since it causes beam distortion and "optical damage". Therefore many studies concern the resistance to photorefraction by adding to LN an appropriate dopant, such as MgO (at concentrations of 5-6 mol%).

Raman spectroscopy is a powerful technique which provides a number of information about physical or chemical properties of a material. It can give information about the structure defects of the lattice as well. That's why it was interesting to study how the properties of LN can reflect on Raman spectra.

The aim of my study is Raman studies in photorefractive LN and by this way to investigate the peculiarities and consequences of the photorefractive properties on the Raman spectra. Several mechanisms are associated with the photorefractive effect. The question is how these phenomena affect the Raman spectra. We thus need to distinguish the successive consequences of the laser beam input: thermal change, the space charge field, and since LN is piezoelectric the subsequent lattice strain. Therefore we can speak about photo-electrostriction effect. In a complement we study the Zr doping on LN which is a candidate for inhibiting the photorefractive effect.

The thesis consists of four chapters: the first part concerns the structure and general linear and non-linear properties of LN. Among photo-induced effects we describe in more details the photorefractive effect.

The second chapter describes typical Raman spectra characterizing undoped LN crystal. Generalities of Raman spectroscopy and spectrometer with its' characteristics are reported. Then the polarized Raman spectra measured on LN are presented for all possible configurations according to the direction of polarization and Raman selection rules. All observed lines are assigned and compared with expectations according to selection rules. In order to see the polarization influence on the Raman spectra, measurements are performed on congruent LN powder as well as unpolarized spectra of LN crystals. It is underlined that Raman spectra of LN are very sensitive to the polarization direction. These results will serve as references for comparison with data reported in chapter III (Zr doped LN) and chapter IV (Fe doped LN).

In the third chapter, I report Raman spectra on LN samples doped with different concentration of Zr. Results are analyzed by means of classical deconvolution of spectra and statistical chemometrics methods. The results are compared and discussed in terms of site spectroscopy of Zr ions and compared with literature results.

The fourth chapter of the thesis is the investigation of photorefractive effects by polarized Raman measurements on Fe doped LN as a function of time. Photo-induced space charge field can lead to a strain of the lattice due to the piezoelectric property of the crystal. It is shown how mentioned effects can be reflected in Raman spectra. The chapter is divided into two parts: in the first part are reported and analyzed the data obtained by means of forward and backward Raman scattering, pointing out the influence of the beam defocusing on the breaking of Raman selection rules. In the second part the shift of frequency with time of some lines are studied in order to evidence the photorefractive induced strain effect.

Appendix A presents one of our published results that is temperature dependence of Raman spectra and anharmonic behavior of some Raman lines. Appendix B concerns the demonstration of principles of fitting procedure that were performed on all obtained Raman spectra.

CHAPTER I

Lithium Niobate Crystals Properties

I.I – Introduction

Lithium Niobate ($LiNbO_3$, LN) [1] belonging to the ABO3-type ferroelectrics with oxygen octahedra, is a material that does not exist in nature, but since their first synthesis in 1949, they have been intensely studied [2,3]. Lithium Niobate is a key material in photonic technology, characterized by a combination of several favorable properties, such as high nonlinear optical coefficients, wide transparency, established technology for fabricating waveguides, and a periodically poled structures. It is widely used in various applications such as electro-optics, acousto-optics and frequency conversion. LN shows another remarkable property, namely photorefractivity (sometimes called optical damage), which appears under the illumination with visible or near-infrared light and leads to semi-permanent changes in the index of refraction of the crystal. This leads to beam distortion and a drastic decrease of the device efficiency.

Another very interesting property of the crystal is the bulk photovoltaic effect. A feature expressed by some impurities in the material resulting in the generation of photo-induced currents or voltages under certain light incidence.

The structure of $LiNbO_3$ at room temperature (RT) belongs to the rhombohedral (trigonal) space group R3c, with point group 3m. Above the phase transition temperature ($\approx 1150^oC$) the crystal transforms into the centrosymmetric space group R3m. The setting of the crystallographic axes for the trigonal symmetry is not monosemantic. As discussed in the following section there are three choices of axes for $LiNbO_3$, namely, rhombohedral, hexagonal, and orthohexagonal cells. For the structure description or determination as well as for crystallographic aims rhombohedral and hexagonal settings are more suitable. For most applications the orthohexagonal setting, where all axes are mutually orthogonal, is preferable.

The resistance to optical damage can be increased considerably by changing the lithium niobate (LN) composition from congruent (cLN; [Li]/[Nb]=0.94) to stoichiometric (sLN: [Li]/[Nb]=1) or by adding to LN an appropriate dopant. Among the many dopants that have been tested, the most utilized is, at present, MgO that is known to be effective in molar concentrations above 5 mol% . The main problem is that it is very difficult to grow large homogeneous Mg doped LN crystals. Crystals with alternative non-photorefractive ions were recently synthesized with tetravalent ions (Hf^{4+}, Zr^{4+}, etc), which were found to be very efficient with an optical damage threshold around – 2-3mol%.

I.II – Structure of LN crystals and its defects

I.II.1 - Structure of LN crystals

The crystallographic structure of the lithium niobate is rhombohedral with 10 atoms per unit cell (fig I.1). This structure is characterized by parallel planes of oxygen atoms, in a compact arrangement (fig I.1) approximately hexagonal. The latter corresponds to a stack of oxygen octahedra, along the ferroelectric axis (trigonal), by the following sequence Nb□ LiNb□ LiNb□ Li Nb ... (□ represents a vacant site). Li and Nb are displaced from the center of the oxygen octahedron in the direction of the polar axis c.

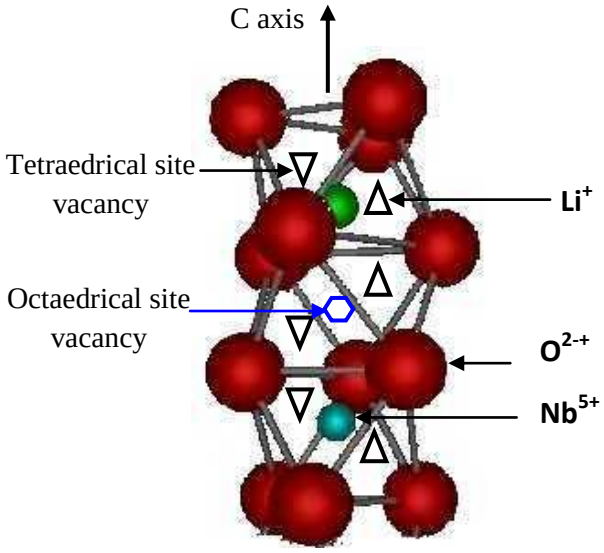

Figure I. 1*– unit cell of LN in FE phase*

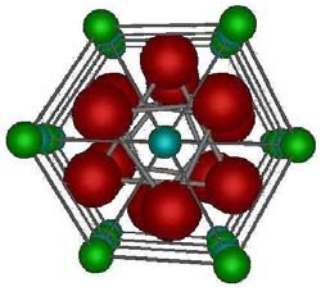

Figure I. 2*– hexagonal compact structure*

In the paraelectric phase (PE) above the Curie temperature Tc≈1150° C, $LiNbO_3$ belongs to the $R\bar{3}_c$ space group and $\bar{3}m$ point group. In this case the Nb atoms come to occupy the centers of the oxygen octahedra. As for Li atoms, they move on the faces of two adjacent oxygen [4] octahedra always keeping the sequence described above Nb□ LiNb□ LiNb□ Li Nb .... The hexagonal unit cell is presented in fig.I.3, including the corresponding hexagonal axes a,b,c and the axes of the cartesian crystal coordinate system X,Y,Z. The cations Li^+ and Nb^{5+} are displaced along the Z axis with respect to their positions above the Curie temperature in the oxygen planes and in the middle between the oxygen planes, respectively.

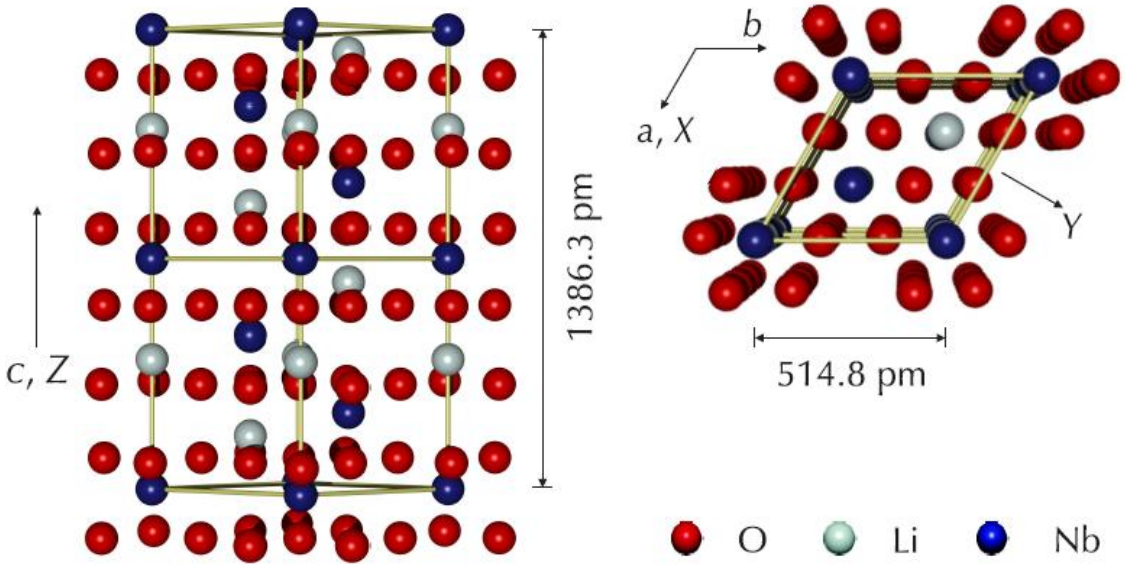

Figure I. 3 *- LN structural presentation with the use of hexagonal axes*

The threefold axis is Z, the Y axis lies in the mirror plane, and the X axis is orthogonal to both of them. The *c*-axis is parallel to the polar Z axis of the crystal, while the X axis is chosen to be parallel to one of the three equivalent crystallographic axes (a) spaced by 120 ° and which are perpendicular to the Z axis and to Y-Z plane. Therefore, the Y-axis is along a plane of symmetry and perpendicular to both X and Z axes [16].

The lattice parameters of $LiNbO_3$ have been studied by several authors. Tables I.1 and I.2 summarize the results obtained by R. Hsu et al. [5].

Lattice parameters			
a = b = 5.148(3) Å	c = 13.863(3) Å	v = 318.2(4) $Å^3$	
Positions of atoms in the lattice (Nb is taken as the origine)			
Nb	0	0	-0.02210(2)
O	0.0475(5)	0.34301(5)	0.0625(5)
Li	0	0	0.2086(4)

Table I. 1 *– Lattice parameters and positions of the atoms in the unit cell of LN [5]*

Interatomic distances in Å	
Nb—Nb	3.765(5)
Nb—O	1.876(4)
	2.130(5)
Nb—Li	3.028(6)
	3.058(2)
	3.372(3)
	3.904(6)
Li—Li	3.765(5)
Li—O	2.063(3)
	2.245(3)
	3.291(2)
	3.449(8)

Table I. 2*– Interatomic distances of a crystal of congruent composition*

The interatomic distances has different values for the same atoms because of taking into account the Li vacancies.

I.II.2 – Stoichiometric and congruent LN

LN crystals are colorless, chemically stable and insoluble in water and organic solvents, and have a high melting point. The chemical reaction used to develop lithium niobate from the $Li_2CO–Nb_2O_5$ system is as follows

$$Li_2CO_3 + Nb_2O_5 \rightarrow 2LiNbO_3 + CO_2 \quad (I.1)$$

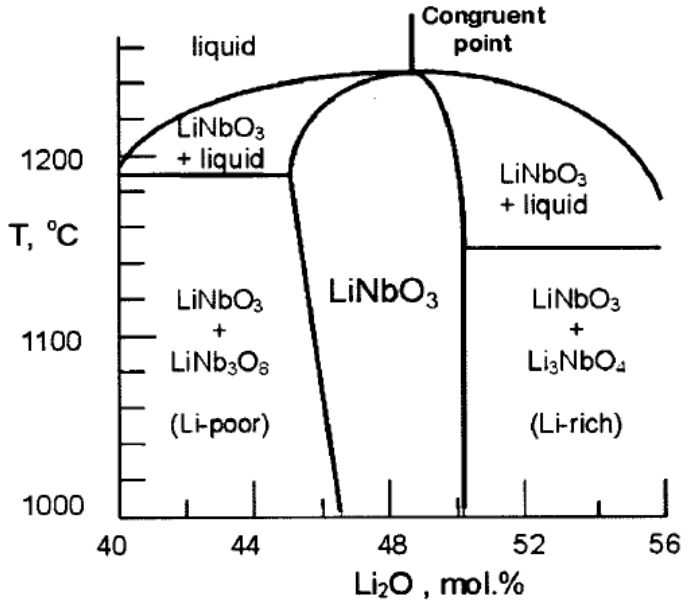

Figure I. 4*- Schematic phase diagram of the Li_2O–Nb_2O_5 of the congruent and stoichiometric composition of LN*

One can see from the phase diagram of the Li_2O-Nb_2O_5 system (figure I.4) that there is one single point where both compositions and crystal are identical through the growth process, this is the congruent composition (48.4-48.6 mol%. Li_2O, [6,7,8]). This composition is easier to achieve than a stoichiometric LN crystal that has ideally equivalent percentages of both Li and Nb species (~ 50 mol%. Li_2O). The composition of the LN is defined by:

$$x_c = \frac{[Li]}{[Li]+[Nb]} \qquad \text{(I.2)}$$

where [Li] and [Nb] are the concentrations of Li and Nb respectively. The commercial congruent $LiNbO_3$ crystals are grown by the usual Czochralski technique by pulling from a melt.

I.II.3 – Defect structure of LN crystals

I.II.3.1 – Intrinsic defects

As we have seen above, the LN crystal can be synthesized with different compositions. Generally, they are deficient in Li (or excess Nb) up to 6%. This deficiency is the cause of the existence of intrinsic defects in the structure of LN that ensures the neutrality

of electric charge. The nature of the defects may be structural vacancies (Li or Nb vacancy), or cations occupying sites other than their own sites in the ideal structure of LN.

I.II.3.2 - Structural defects and models

Lithium deficiency in LN can be described in terms of vacancy cations Li^{+} or Nb^{5+} and shortcomings of oxygen by different mechanisms of charge compensation. To explain the structure of intrinsic defects from the crystals listed as pure LN, three models have been proposed:

a) Oxygen vacancies:

In this model proposed by Fay [9], the structure of LN crystal is given by:

$$[Li_{1-2x}V_{2'x}]_{Li}[Nb]_{Nb}[O_{3-x}V_{x^{oo}}] \qquad \text{(I.3)}$$

The charge neutrality is ensured via oxygen vacancies. Their creation results in a decrease of the density of the material and the lattice parameters. This model was excluded by measurements of lattice parameters and density of samples of different compositions of LN [10]. In fact, this model predicted cell parameters higher for a stoichiometric composition comparing to the congruent, while Lerner et al [10] proved the contrary.

b) Lithium vacancies:

The results obtained by Lerner et al [10] measuring density based on the composition of the crystals were in contradiction with the model of Fay. So they proposed another model to describe the structure of LN based on Li vacancies.

$$[Li_{1-5x}\square_{4x}Nb_x]_{Li}NbO_3 \qquad \text{(I.4)}$$

In this model one can explain the non-stoichiometric by excess of Nb replacing cations in site Li + (antisite Nb, Nb *). The charge compensation is provided via Li vacancies.

c) Niobium vacancies:

Structural investigations carried out by Abrahams and March [11] on congruent crystals and compositions close to stoichiometry, performed using X-ray measurements, have shown that the non-stoichiometric structure can be described by:

$$[Li_{1-5x}Nb_{5x}]_{Li}[Li_{1-4x}\square_{4x}]_{Nb}O_3 \quad \text{(I.5)}$$

It is observed in this model the presence of Nb antisites and vacancy Nb created to ensure the balance of electric charge. But the presence of a gap in highly charged Nb is energetically unstable, as shown by Donnenberg et al [12] with their model. To not to be in contradiction with the Abrahams and March model, they suggested the existence of an ilmenite structure in localized regions of the LN.

I.II.3.3 - Extrinsic defects

Extrinsic defects are due to the presence in the LN matrix of other constituent elements of LN (Li , Nb and O) . These foreign elements may be naturally present in LN and often undesirable, in this case we speak about impurities. And despite all the precautions taken during the development of LN crystals , we can not prevent the presence of impurities .Also, they may be intentionally added to the matrix LN to improve certain physical properties , and in this case we speak about doping. The most common dopants are non photorefractive ions such as Mg , Zn, In, Zr ... to increase the resistance to optical damage or transition metals such as Fe , Mn, Cu ... for photorefractive applications and rare earths Nd , Er , Yb, Dy ... for laser applications.

I.III – Properties of LN crystals

I.III.1 – Ferroelectricity

Ferroelectrics, which concern also LN crystals, are compounds with spontaneous polarization *Ps*, the sign of which can be changed under the influence of an external electrical field [13-15].

The electrical polarization is defined as the average of the dipole moment per unit of volume:

$$P^{(\omega)} = P_L^{(\omega)} + P_{NL}^{(\omega)} \quad \text{(I.6)}$$

where

$$P_L^{(\omega)} = \varepsilon_0 \chi^{(1)} E^{(\omega)} \quad \text{(I.7)}$$

is the linear polarization and $P_{NL}^{(\omega)}$ is the NL polarization induced by sufficiently intense light field. ε_0 = 8.085 × 10^{-12} F/m is the dielectric permittivity of vacuum. $\chi^{(1)}$is the response of the dielectric tensor. In linear optics the response $\chi^{(1)}$ of an isotropic medium is a complex function of frequency and may be expressed as [15]:

$$\chi^{(1)} = \chi_R^{(1)} + i\chi_I^{(1)} \qquad \text{(I.8)}$$

where I and R indices symbolize the real and imaginary parts, respectively.

I.III.2 – Pyroelectric effect

A pyroelectric material shows a change in the spontaneous polarization P_s as a function of temperature. The relationship between the respective variations of ΔP and ΔT is linear, and can be expressed as [16]

$$\Delta P_{LN} = \widetilde{p_{LN}} \cdot \Delta T, \text{ and } \widetilde{p_{LN}} = p_i = \begin{pmatrix} 0 \\ 0 \\ p_3 \end{pmatrix} \qquad \text{(I.9)}$$

where $\widetilde{p_{LN}}$ is the pyroelectric tensor ($p_3 = \Delta P_s/\Delta T = -8.2 nC\,cm^{-1}K^{-1}$ in the case of congruent LN crystal [17-19]. The negative value of p indicates that after cooling, the + c face of the crystal is charged positively.

Any excess or lack in screening charges (σ_{sc} relatively to P_s) leads to the appearance of an electrostatic state thus uncompensated charges: $\rho = \Delta(P_s - \sigma_{sc})$. This generates a strong electric field within the crystal (Fig. I.5), which can have the order of 10^6-10^8 Vcm^{-1} [20,21].

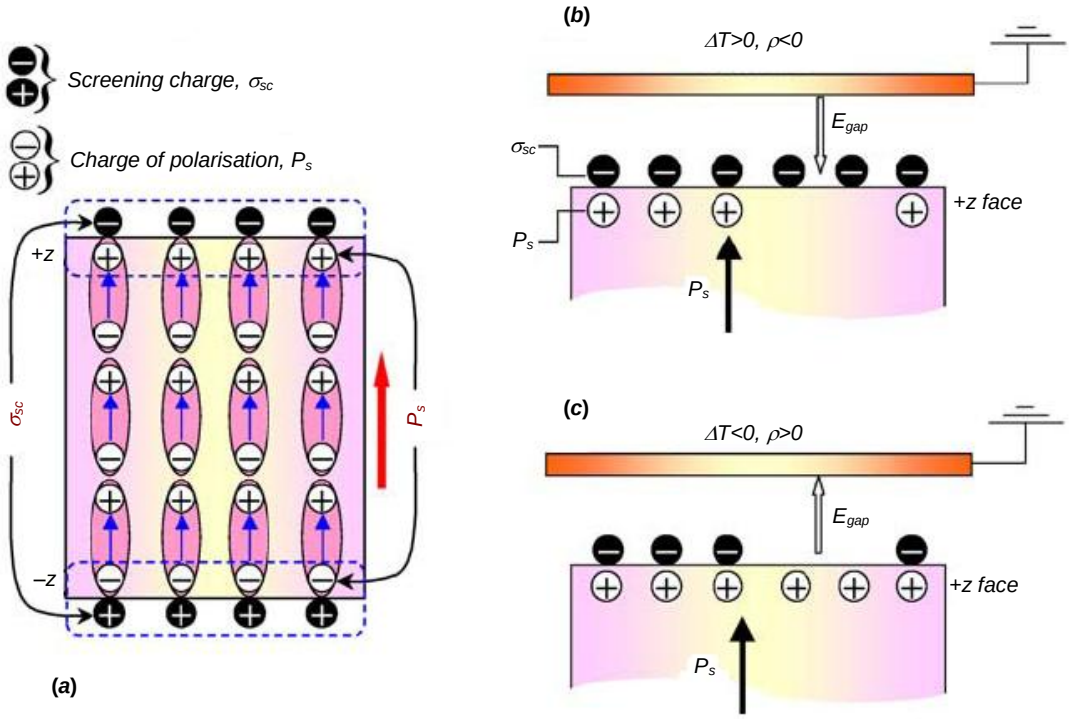

Figure I. 5*- Schematic diagram of the evolution of electrostatic state for charges which are not compensated on the surface of the face + z depending on the temperature [16]: (a) at equilibrium, (b) when the temperature decreases, and (c) when the temperature increases.*

The current generated during this phenomenon, in the case of a laser radiation of intensity I_0 is as following [22]:

$$J^{pyro} = \frac{\partial P_s}{\partial T}\frac{dT}{dt} = \frac{\partial P_s}{\partial T}\frac{I_0(1-\exp(-\alpha d))}{C_p d\rho} \qquad \text{(I.10)}$$

T is the temperature of the crystal, $I_0(1-\exp(-\alpha d))$ is the intensity of the absorbed light, α is the absorption coefficient, d is the thickness of the crystal, C_p is the calorific capacity of LN and ρ is the density. This effect allows us in particular to determine the orientation of the c axis which is the same as the current which affected it. It is important to mention that the E^{pyro}pyroelectric field is often overlooked but can be important during illuminations with high intensities [22]:

$$E^{pyro} = \frac{1}{\varepsilon\varepsilon_0} p\Delta T \qquad \text{(I.11)}$$

Where ε and ε_0 are the dielectric permittivities of LN and vacuum, respectively.

I.III.3 Piezoelectric effect

Piezoelectricity is the phenomenon where the application of a stress on the crystal leads to a variation of the polarization (voltage) between its faces [23]. This is due to the separation of positive and negative charges in the considered medium. The reverse phenomenon also exists: the application of an external electric field induces a change in the shape. And the same piezoelectric tensor is used in both cases [24]. The polarization P generated by the stress σ is described (direct piezoelectric effect) by the following equation [16] in the case of C_{3v} LN symmetry:

$$P_i = \sum_{j,k} d_{i,jk}\sigma_{jk}\,;\ \begin{pmatrix} P_x \\ P_y \\ P_z \end{pmatrix} = \begin{pmatrix} 0 & 0 & 0 & 0 & d_{15} & -2d_{22} \\ -d_{22} & d_{22} & 0 & d_{15} & 0 & 0 \\ d_{31} & d_{31} & d_{33} & 0 & 0 & 0 \end{pmatrix} \begin{pmatrix} \sigma_{xx} \\ \sigma_{yy} \\ \sigma_{zz} \\ \sigma_{yz} \\ \sigma_{zx} \\ \sigma_{xy} \end{pmatrix} \qquad \text{(I.12)}$$

where the notation of Voigt is used for indexing the $d_{i,jk}$ (elements of piezoelectric tensor of third rank) and σ_{jk} (elements of stress tensor of rank 2).

$$i: x=1, y=2, z=3$$

$$jk: xx=1, yy=2, zz=3, zy=yz=4, xz=zx=5, xy=yx=6$$

So the piezoelectric effect can be described by 4 independent coefficients (d_{15}, d_{22}, d_{31}, d_{33}). Piezoelectric applications such as surface wave filters (widely used in telephony) [23] use single crystals of LN due to their strong coupling coefficients and low temperature coefficients.

I.IV – Linear and non-linear optical properties of LN

I.IV.1 – Linear properties

Lithium niobate is a uniaxial birefringent crystal with a higher ordinary refractive index n_o than the extraordinary index of refraction n_e (negative uniaxial) [16]. These refractive indices vary depending on wavelength of the incident electromagnetic wave (EM) [25] and the temperature of the crystal. $n_o=2.29$ and $n_e=2.20$ are refractive indices of ordinarily and

extraordinarily polarized light for LN at the light wavelength 633nm and at room temperature [26].

I.IV.1.1 – Refractive indices and birefringence of LN

The variation (dispersion) of n_o and n_e with laser for LN is given by the Sellmeier's equation [27, 28]. It is used to describe this dependence with the transparency band of LN, 340-4600 nm, and the general expression was determined by U. Schlarb and K. Betzler [28]. The expression is composed of a combination of oscillators contributing to the two refractive indices n_o and n_e. For a composition of between 47 and 50 % mol Li_2O, and on the intervals of wavelength in a range of 400 to 1200 nm, and for temperature range of 50 to 600 K, we have [28]:

$$n_i^2 = \frac{(50+X_c)}{100}\frac{A_{0,i}}{(\lambda_{0,i}+\mu_{0,i}F)^{-2}+\lambda^{-2}} + \frac{(50-X_c)}{100}\frac{A_{1,i}}{(\lambda_{1,i}+\mu_{1,i}F)^{-2}-\lambda^{-2}} - A_{IR,i}\lambda^2 + A_{UV} \quad \text{(I.13)}$$

$$\text{with}: F = f(T) - f(T_0)$$
$$= (T+273)^2 + 4.0238\times10^{-5}\left[\coth\left(\frac{261.6}{T+273}\right)-1\right] - f(T_0). \quad \text{(I.14)}$$

where *i* is the ordinary (o) or extraordinary (e) parts, X_c is the composition of the sample, λ is the wavelength, $A_{0,i}$, $A_{1,i}$ are the forces of two oscillators of Sellmeier, $\lambda_{0,i}$, $\lambda_{1,i}$ are the positions of oscillators, $\mu_{0,I}$ and $\mu_{1,i}$ are coefficients which present the temperature dependence, $A_{IR,i}$ is the contribution of IR (infrared) zone associated to the absorption, A_{UV} is the contribution of plasmons to the index of the refraction, T is the crystal temperature and T_0 is the room temperature.

Figure I.6 illustrates the evolution of n_e and n_o indices for a congruent composition of LN crystal at room temperature. At this temperature, the difference of n_o between the congruent and stoichiometric crystals does not exceed 10^{-3}. In contrast, the n_e index has a clear difference between the two compositions. The n_e index decreases when approaching to the stoichiometry (about 10^{-2}), n_o varies very little as a function of temperature compared to n_e for all compositions. Schlarb and Betzler [29] have experimentally confirmed the expression of Sellmeier's equation in the case of Mg and Zn doped LN crystals.

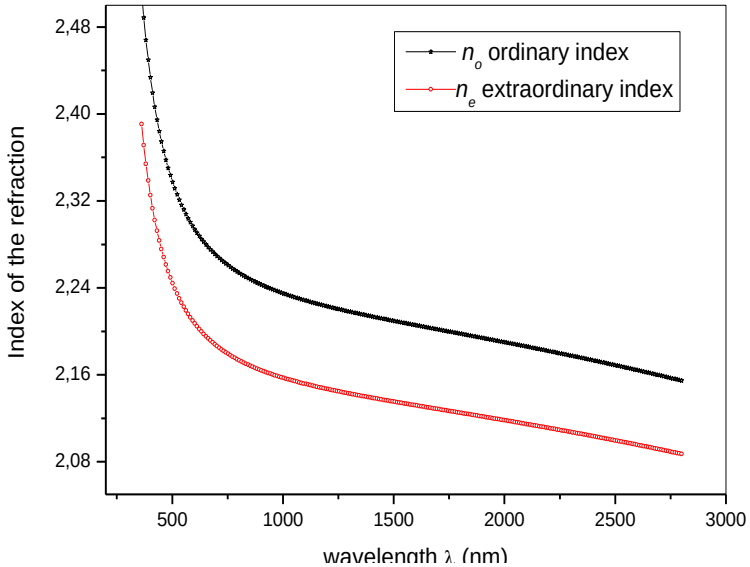

Figure I. 6 *– Dispersion of the indices of refraction of a congtuent LN crystal at room temperature (by equation of Sellmeier)*

I.IV.1.2 – Elasto-optic effect

The elasto-optic effect is a change in the refractive index as a result of strain applied to LN. The relation between the deformation and the refractive index is linear, usually described by [16]:

$$\Delta\left(\frac{1}{n^2}\right)_{ij} = \sum_{k,l} p_{ij,kl}\, s_{kl} \qquad \text{(I.15)}$$

Where $\Delta(1/n^2)_{ij}$ belongs to a tensor of rank 2 describing the changings in the relative dielectric permeability, s_{kl} is the deformation in the plane x_l, and applied along the axis x_k (of a tensor of rank 2), and p_{ijkl} is the effective elasto-optic coefficient that belongs to a tensor of rank 4.

I.IV.1.3 – Linear electro-optic effect (Pockels effect)

The Pockels effect, or linear electro-optical effect (EO), occurs when the refractive index of the crystal is changed in proportion to the applied electric field [30]. This effect can only occur in non centrosymmetric materials. Mathematically, the Pockels effect can be

described by the induced deformation of the ellipsoid of refractive indices in the presence of an electric field, which is defined by:

$$\left[\frac{1}{n_o^2}+r_{12}E_2+r_{13}E_3\right]x_1^2+\left[\frac{1}{n_o^2}+r_{22}E_2+r_{23}E_3\right]x_2^2+\left[\frac{1}{n_e^2}+r_{33}E_3\right]x_3^2 \qquad \text{(I.16)}$$
$$+2r_{42}E_2x_2x_3+2r_{51}E_1x_1x_3+2r_{61}E_1x_1x_2=1$$

where r_{ij} are the effective EO coefficients of LN. The variation factors of x_i (impermeability dielectric components) due to the electric field $E = (E_1, E_2, E_3)$, are linear and are expressed as the following [30]:

$$\delta\left(\frac{1}{n^2}\right)_{ij}=\frac{1}{n_{ij}^2}\bigg|_E-\frac{1}{n_{ij}^2}\bigg|_{E=0}=\sum_k r_{ijk}E_k=\delta B_{ij}(E)$$

$$\text{and } B_{ij}=\left(\frac{1}{\varepsilon_{ij}}\right)=\left(\frac{1}{n^2}\right)_{ij} \qquad \text{(I.17)}$$

$\tilde{r}_{ijk}$ tensor of EO coefficients is a tensor of rank 3 with 27 items. Due to its symmetry, it can be described by 18 independent items, and using Voigt notation (i and j indices) [16], it can be written as following [6x3] matrix:

$$\tilde{r}_{ij,k}=\begin{bmatrix}0 & -r_{22} & r_{13}\\ 0 & r_{22} & r_{13}\\ 0 & 0 & r_{33}\\ 0 & r_{51} & 0\\ r_{51} & 0 & 0\\ -r_{22} & 0 & 0\end{bmatrix} \qquad \text{(I.18)}$$

I.IV.2 – Non-linear properties

The non-linear (NL) response is the part of the polarization induced by intense light beams (such as available with lasers), which depends non-linearly of the optical electric field. The instantaneous polarization can be generated as a NL response by a development in a Taylor series: [31]

$$P(t) = \varepsilon_0(\chi^{(1)}E(t) + \chi^{(2)}E^2(t) + \chi^{(3)}E^3(t) + \cdots) \qquad \text{(I.19)}$$

where ε_0 is the dielectric permittivity in vacuum. The first term represents the linear effects (L), the second term represents the NL effects of 2nd order. By switching to (ω) frequency range, the instant polarization of the 2nd order can be expressed in terms of the components of Fourier of the electric field E (ω) by equation [25]:

$$\begin{aligned} P_i(\omega_3) &= 2\sum_{jk} \chi_{ijk}^{(2)}(\omega_3 = \omega_1 \pm \omega_2)E_j(\omega_1)E_k(\omega_2) \\ &= \sum_{jk} \varepsilon_0 d_{ijk}^{(2)}(\omega_3 = \omega_1 \pm \omega_2)E_j(\omega_1)E_k(\omega_2) \end{aligned} \qquad \text{(I.20)}$$

where the NL optical coefficients belong to a tensor of rank 3. By conservation of energy and moment, the NL optical effects resulting from the last equation are the optical effects of a generation of a sum of frequencies (or a difference, $\omega_1 \neq \omega_2$) [32, 33]:

$$\begin{bmatrix} P_x(2\omega) \\ P_y(2\omega) \\ P_z(2\omega) \end{bmatrix} = 2\varepsilon_0 \begin{bmatrix} 0 & 0 & 0 & 0 & d_{31} & -2d_{22} \\ -d_{22} & d_{22} & 0 & d_{33} & 0 & 0 \\ d_{31} & d_{31} & d_{33} & 0 & 0 & 0 \end{bmatrix} \times \begin{bmatrix} E_x^2(\omega) \\ E_y^2(\omega) \\ E_z^2(\omega) \\ 2E_y(\omega)E_z(\omega) \\ 2E_x(\omega)E_z(\omega) \\ 2E_x(\omega)E_y(\omega) \end{bmatrix} \qquad \text{(I.21)}$$

I.IV.2.1 – Photorefractive effect, defocusing of the beam

The photorefractive effect (PR) was discovered as an optical damage in nonlinear and electro-optic crystals. The effect occurs in the illuminated region of the crystal light as a result of spatial transfer of photocarriers, which are subsequently captured by deep traps and form a space-charge field. This field through the linear electro-optic effect leads to a change in the refractive index of the crystal. The refractive index variations induced by the light have limited the usefulness of non- linear crystals in optical devices. When a crystal is exposed to intense laser radiation, the inhomogeneous variation causes the refractive index distribution thus defocusing the laser beam in the optical components such as modulators and frequency doublers. Generally these changes are retained even after switching off the laser. However,

materials exhibiting a photorefractive effect are found in important applications such as in holography field, and in information storage.

Of special importance for photorefractive effects are optical absorption processes. Pure LN crystal is transparent in the near-IR, the visible, and the near-UV regions up to about 3.8 eV, where the fundamental absorption begins.

Photorefractive effect in LN crystals

As the PR effect is a change of the refractive index of a material caused by an illumination, the photorefractive effect occurs in the illuminated area of the crystal as a result of spatial transfer (drift or diffusion) of photocarriers and their subsequent trapping at deep levels. The trapped carriers form a space-charge field E_{sc}, which due to the linear electro-optic effect leads to changes of refractive index in the non-centrosymmetric crystal.

$$\left(\frac{1}{\varepsilon_{ij}}\right) = \left(\frac{1}{\varepsilon_0}\right) + r_{ijk}E_k \qquad \text{(I.22)}$$

where ε_{ij} and r_{ijk} are components of the tensors of the dielectric permittivity and linear electro-optic effect, respectively, ε_0 is the initial value, E_k is a component of the E_{sc}. Transfer of photo carriers (photocurrent) includes the following components:

$$j = j_{ph.} + j_{drift} + j_{diff} \qquad \text{(I.23)}$$

For dielectric oxides with a wide conduction band for photocarriers it is assumed a zone transfer mechanism. The first term in the above mentioned expression is the bulk photovoltaic current, which is characteristic only for non-centrosymmetric crystals such as LN. In the case of a uniform illumination of the crystal in its volume, the photovoltaic current can be expressed as:

$$j_{ph} = \beta_{ijk}e_j e_k^* I \qquad \text{(I.24)}$$

where e_j and e_k^* are unit vectors of polarization of light waves, $I = |a^2|$ - intensity, β_{ijk} is the complex photovoltaic tensor. In view of the β_{ijk} tensor properties the above mentioned expression can be transformed into

$$j_{ph} = \beta_{ijk}e_j e_k^* I + i\beta_{ijk}e_j e_k^* I = j_L + j_C \qquad \text{(I.25)}$$

where the first and the second terms are so-called linear and circular photovoltaic currents. Linear current is different from zero independently on the polarization of the light, circular current is nonzero for elliptically or circularly polarized light. In the scalar form the photovoltaic current can be presented as:

$$j_{ph}=k_G \alpha I \qquad \text{(I.26)}$$

where k_G is the Glass constant, α the absorption coefficient and I is the intensity. Upon reaching the diffusion-drift equilibrium the stationary (limit) value of the photovoltaic current in the scalar representation can be expressed as:

$$E_{sc} = \frac{j_{ph}}{(\sigma_{ph}+\sigma_d)} = \frac{k_G \alpha I}{(\sigma_{ph}+\sigma_d)} = \frac{k_G \alpha}{A} \qquad \text{(I.27)}$$

where σ_{ph} and σ_d are the photo and dark conductivity, respectively.In LN crystals there are two mechanisms for the transfer of photocarriers. The bulk photovoltaic effect and the diffusion mechanism. However, the predominant mechanism is the photovoltaic, and the light induced refractive index change ($\delta\Delta n$) can be represented by the following expression [34]:

$$\delta\Delta n = R_{eff} E_{sc} = R_{eff} \frac{j_{ph}}{(\sigma_{ph} + \sigma_d)} \qquad \text{(I.28)}$$

where R_{eff} is the effective electro-optic coefficient.

Well-known one center model (figure I.7) of transport in photocarriers in which a transition metal ion with low valence (Fe^{2+}) acts as a donor, and the high-valence ion (Fe^{3+}) as the electron trap [34-36].

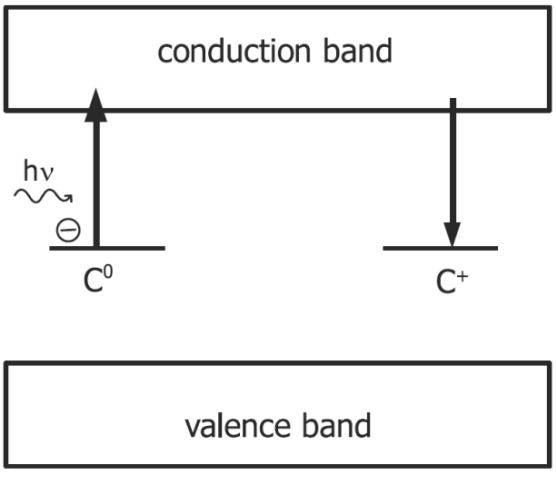

***Figure I. 7**- Photo-induced charge transport schemes. One-center model*

For transferring photocarriers between these centers, the photovoltaic current and photoconductivity are taken into account. This transfer may be represented as:

$$Fe^{2+} + h\upsilon \leftrightarrow Fe^{3+} + e^{-} \qquad \text{(I.29)}$$

In the mentioned model photoconductivity is expressed as:

$$\sigma_{ph} = ne\mu = g\tau e\mu = (qe\mu / h\upsilon)(S_{ph} / \gamma_r)(N_D / N_C)I = A(N_D / N_C)I \qquad \text{(I.30)}$$

where g is the rate of photogeneration, τ is the lifetime of photocarriers in the conduction band, μ is the mobility, q is the quantum yield, α is the absorption coefficient, υ is the velocity of the sound, γ_r is the recombination coefficient, S_{ph} is the probability of photoexcitation of the donor, N_D and N_C are concentrations of donors and traps respectively.

If the photoconductivity is proportional to the concentration of donors (Fe^{2+}) and inversely proportional to the concentration of traps (Fe^{3+}), the photovoltaic current is determined by the process of photogenerated electrons from donors (Fe^{2+}) [35] and is proportional to the concentration of the donor (Fe^{2+}):

$$j_{ph} = \beta I = kS_{ph}[Fe^{2+}]I \qquad \text{(I.31)}$$

It means that $\delta\Delta n$ is proportional to the concentration of Fe^{3+}.

At the first stage the one-center of the photorefractive effect is quite coincide with the experimental data. However, the effects observed in crystals doped with iron at high concentrations , such as sublinear lux-ampere characteristic , it is difficult to fit withthe mentioned model , and it is necessary its correction in the form of descriptions of charge transport through two (or more) central scheme. In the role of an additional ("secondary") shallow level capture photocarriers center Nb_{li}^{4+} was proposed [37]. Schematically photocarriers transfer at the two-center model is shown in figure I.8 [38]:

From the equation (I.28) it is obvious that the photorefractive effect can be reduced by an decrease of photovoltaic current $(j_{ph.v})$ and/or increasing of any conductivity (σ_{ph} or σ_d). Attempts to reduce the photovoltaic current by growing very pure crystals in fact yielded no

results. Significant increase of σ_d and a corresponding decrease of $\delta\Delta n$ was achieved as a result of a strong reduction of the LN crystal or heavily doping. This however leads to a staining of the crystals, which excludes their use in optics.

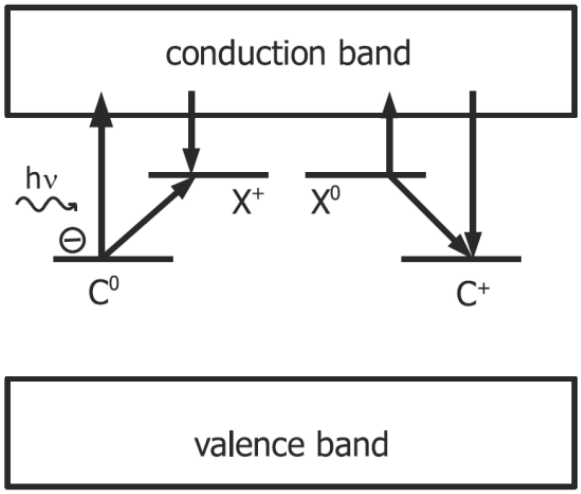

Figure I. 8 *– Photo-induced charge transport schemes. Two-center model*

The suppression of the photorefractive effect by its increasing achieved by doping crystals with so-called non photorefractive impurity ions [39-43]. Doping LN crystals with impurity ions at concentrations above the thresholds resulted in a dramatic suppression of photorefractive effect, reducing the value by two orders of magnitude. It has to be noted, that although the most common non photorefractive ions on these days are Mg ions, it is required a high threshold (5-6 mol% MgO) which leads to a significant reduction in the optical quality of the grown crystals. Among other negative consequences of doping LN crystals with MgO above the thresholds should be noted drop in almost an order of magnitude of the laser damage threshold [44] and the lack of reproducibility of the properties of these crystals.

When a laser beam polarized in z-direction propagates through the LN sample for some time the laser beam expands as it is shown in figure I.9.

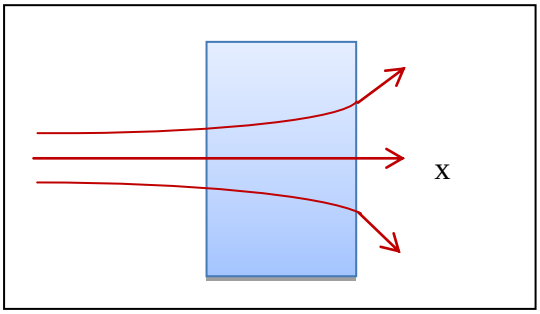

Figure I. 9 *– defocusing of the beam with time in the sample due to the photorefractive properties*

Nippus and Claus [45] investigated this process. They recorded the time dependence of the shape of the laser beam that interacts with the sample. The incident light was polarized once parallel and perpendicular to the optical Z axis. It was shown the intensity decrease of the recorded pattern as well as the intensity decrease of Raman intensity of optical phonons.

I.V - References

[1] K.K. Wong, *"Properties of lithium niobate"*, INSPEC-The Institution of Electrical Engineers, London, U.K. (2002)

[2] A.M. Prokhorov and Yu S. Kus'minov, *"Physics and chemistry of crystalline lithium niobate"* The Adam Hilger Series on Optics and Optoelectronics, Adam Hilger, Bristol and New York (1990)

[3] B.T. Mathias and J.P. Remeika, "*Ferroelectricity in the ilmenite structure*" Phys. Rev. 76, 1886 (1949)

[4] S. C. Abrahams, E. Buehler, W. C. Hamilton, S. J. Lapaca "*Ferroelectric lithium tantalite – III. Temperature dependence of the structure in the ferroelectric phase and the para-electric structur at 940K",* J. Phys. Chem. Solids, 34, 521, (1973)

[5] R. Hsu, E. N. Maslen, D. du Boulay, N. Ishizawa*, "Synchrotron X-ray Studies of $LiNbO_3$ and $LiTaO_3$",* Acta. Cryst. B 53, 191, (1997)

[6] P. F. Bordui, R. G. Norwood, C. D. Bird, G. D. Calvert, *"Compositional uniformity in growth and poiling of large-diameter lithium niobate crystals*" J. Cryst. Growth 113, 61, (1991)

[7] I. Baumann, P. Rudolph, D. Krab, R. Schalge, *"Orthoscopic investigation of the axial optical and compositional homogeneity of Czochralski grown LiNbO3 crystals"* J. Cryst. Growth 128, 903, (1993)

[8] Yu. S. Kurminov, Kristallografia 40, 1034, (1995)

[9] H. Fay, W. J. Alford, H. M. Dess, "*Dependence of second-harmnoic phase-matching temperature in LiNbO3 crystals on melt composition"* Appl. Phys. Letters 12, 89, (1968)

[10] P. Lerner, C. Legras, P. J. Duman, *"Stoechiométrie des monocristaux de métaniobate de lithium"* J. Cryst. Growth 3-4, 231, (1968)

[11] S. C. Abrahams, P. March *"Defect structure dependence on composition in Lithium Niobate"* Acta. Crystallogr. B 42, 61, (1986)

[12] H. Donnenberg, S. M. Tomlinson, C. R. A. Catlow, O. F. Shirmer "*Computer-simulation studies of extrinsic defects in LiNbO3 crystals"* Phys. Rev. B 44, 4877, (1991)

[13] C.J.F. Böttcher, "*Theory of electric polarization*" J. Electrochem. Soc. 121, 221C, (1974)

[14] W.D. Johnston, Jr, "*Optical index damage in $LiNbO_3$ and other pyroelectric insulators*" J. Appl. Phys. 41, 3279 (1970)

[15] K. Kitamura, Y. Furukawa, K. Niwa, V. Gopalan and T.E. Mitchelli, "*Crystal growth andlow coercive field 180° domain switching characteristics of stoichiometric $LiTaO_3$*" Appl. Phys. Lett. 73, 1073 (1998)

[16] R.S. Weis and T.K. Gaylord, "*Lithium niobate: Summary of physical properties and crystal structure*" Appl. Phys. A 37, 191 (1985)

[17] A. Savage, "*Pyroelectricity and spontaneous poarization in $LiNbO_3$*" J. Appl. Phys. 37, 3071 (1990)

[18] C. Kittel, "*Physique de l'état solide*" Dunod, Paris (1998)

[19] E.M. Bourim, C.-W. Moon, S.-W. Lee, V. Sidorkin and I.K. Yoo, "*Pyroelectric electron emission from –Z face polar surface of lithium niobate monodomain single crystal*" J. Electroceramics 17, 479 (2006)

[20] B. Rosenblum, P. Braunlich and J.P. Carrico, "*Thermally stimulated field emission from pyroelectric $LiNbO_3$*" Appl. Phys. Lett.25, 17 (1974)

[21] G. Rosenman, D. Shur, Ya. E. Krasik and A. Dunaevsky, "*Electron emission from ferroelectrics*" J. Appl. Phys. 88, 6109 (2000)

[22] M. Moustefa, "*Etude des phénomènes photo-induits sur les cristaux de niobate de lithium ($LiNbO_3$) purs et dopés par des caractérisations optiques et électro-optiques*" Thesis in physiques, University of Paul-Verlaine, (2003)

[23] E. Dieulesaint et D. Royer, "*Propagation et génération des ondes élastiques*" Techniques de l'Ingénieur, Traité d'Electronique **E** 3 210, 1 (2001)

[24] J.F Ney, "*Physical properties of crystals: their representation by tensors and matrices*", Oxford – Clarendon press (1985)

[25] X. Zhang, "*High-repetition-rate femtoseconde optical parametric oscillators based on KTP and PPLN*" Dissertation, Marburg/Lahn – Germany (2002)

[26] Y. Furukawa, M. Sato, F. Nitanda, and K. Ito."*Growth and characterization of MgO-doped LiNbO3 for electro-optic devices"* J. Cryst. Growth 99, 832, (1990)

[27] G.J. Edwards and M. Lawrence, "*A temperature dependant dispersion equation for congruently grown lithium niobate*" Opt. Quant. Electron. 16, 373 (1984)

[28] U. Schlarb and K. Betzler, "*Refractive indices of lithium niobate as a function of temperature, wavelength, and composition: A generalized fit*" Phys. Rev. B 48, 15613 (1993)

[29] U. Schlarb and K. Betzler, "*Influence of the defect structure on the refractive indices and Mg-doped lithium niobate*" Phys. Rev. B 50, 751 (1994)

[30] A. Yariv and A.P. Yeh, "*Optical waves in crystals: propagation and control of laser radiation*" J. Wiley and Sons, Corp.: New-York (1984)

[31] P.A. Franken, A.E. Hill, C.W. Peters and G. Weinreich, "*Generation of optical harmonics*" Phys. Rev. Lett.7, 118 (1961)

[32] M. Houé and P.D. Townsend, "*An introduction to methods of periodic poling for second-harmonic generation*" J. Phys. D: Appl. Phys. 28, 1747 (1995)

[33] D.A. Kleinman, "*Nonlinear dielectric polarization in optical media*" Phys. Rev. 126, 1977 (1962)

[34] Lines M.E. and Glass A.M. "*Principles and application of ferroelectrics and related materials*". Clarendon Press, Oxford (1977)

[35] Kratzig E. and Schirmer O.F. "*Photorefractive centers in electro-optic crystals*", In: Gunter P.

and Huignard J.P. (Ed), "*Photorefractive materials and their applications*" I, Topics in Applied Physics, Springer - Verlag, Berlin, Heidelberg, Ney York 61, 131, (1988)

[36] Kukhtarev N.V., Markov V.B., Odulov S.G., Soskin M.S., Vinetskii V.L. "*Holographic storage in electrooptic crystals*". – Ferroelectrics 22, 949, (1979)

[37] Jermann F. and Otten J. "*Light induced charge transport in* $LiNbO_3:Fe$ *at high intensities*" JOSA B 10, 2085 (1993)

[38] Jermann F., Simon M. and Kratzig E. "*Photorefractive properties of congruent and stoichiometric lithium niobate at high light intensities*" J. Opt. Soc. Am. B 12, 2066 (1995)

[39] Zhong Gi-Guo, Jin J. and Wu Zh.-K. *"Measurement of optically induced refractive index damage of lithium niobate doped with different concentration of* MgO " Proc. 11-th Intern, Quantum Electr, Conf. IEEE, 631, (1980)

[40] Bryan D.A., Gerson R. and Tomaschke H.E. "*Increased optical damage resistance in lithium niobate*" Appl. Phys. Lett. 44, 847 (1984)

[41] Volk T.R., Pryalkin V.I. and Rubinina N.M. "*Optical-damage-resistant* $LiNbO_3$ *:Zn crystal*" Optics Letters 15, 996, (1990)

[42] Volk T.R. and Rubinina N.M. "*A new optical damage resistant impurity in lithium niobate crystals*" Indium -Ferroelectrics lett. 14, 37 (1992)

[43] Yamamoto J.K., Kitamura K., Iyi N., Kimura S., Furukawa Y. and Sato M. "*Increased optical damage resistance in* Sc_2O_3 *-doped* $LiNbO_3$ " Appl.Phys.Letts. 61, 2156, (1992)

[44] Furukawa Y., Yokotani A., Sasaki T., Yoshida H., Nitanda F., Sato M., Kunio Yoshida. *"Investigation of bulk laser damage threshold of lithium niobate single crystals by Q-switched pulse laser"* J. Appl. Phys. 69, 3372, (1991)

[45] M.Nippus, R. Claus "*The influence of photorefractive index change on Raman scattering intensities in LiNbO3"* Z. Naturforschung 33a, 924, (1978)

CHAPTER II
Polarized Raman spectroscopy on single LN crystals

II.I – Introduction

Generalities on inelastic scattering and Raman spectroscopy are shortly presented. Then Raman spectra on Lithium Niobate crystal are shown for all possible directions of polarization of the incident and scattered light. It is underlined that the Raman spectra of this material are very sensitive to the polarization direction. All spectra lines are attributed to the different TO and LO phonons according to the configuration and selection rules. This assignment of Raman lines will serve as standard references for the following chapters.

II.II – Raman spectroscopy, generalities

The phenomenon of inelastic scattering of light was first postulated by Smekal [1] in 1923 and then observed experimentally in 1928 by Raman and Krishnan [2]. Since then the phenomenon has been referred to as a Raman spectroscopy. And in 1930 the Nobel Prize in Physics was awarded to Sir Venkata Raman "for his work on the scattering of light and for the discovery of the effect named after him".

Raman spectroscopy [3] then became a powerful spectroscopic technique for characterizing the molecular composition and structure of a material. Raman scattering results from the light-matter interaction and provides the access to molecular and crystal vibrations (phonons). The Raman technique consists of focusing with lens (or microscope objective) a monochromatic light beam on the sample in order to collect the scattered light. This light is collected by means of a further lens (the same lens in the case of a backscattering) and analyzed by a spectrometer. This technique complements infrared spectroscopy [4] which also allows to study the vibrational modes of a material. It has a wide variety of applications in physics and materials chemistry. This is one of the few methods to obtain a characterization of a chemical material in wide ranges of temperatures. In addition, it requires only a very small amount of material without prior preparation. It is also possible, if one has a reference to estimate the concentrations of chemical species constituting the compound.

II.II.1 – Phonons, Raman scattering

A phonon [5] describes a quantum (elementary packet) of vibration in a crystalline solid. A vibration mode of the crystal, defined frequency v, assigns or gain energy per amount of energy hv, where h is Planck's constant. This amount is considered as a quasi-particle, that is a fictive particle associated to the vibration. There are generally two types of phonons: acoustic phonons and optical phonons. The first typically correspond to sonic or ultrasonic waves in the network. They correspond to the vibration modes for which the positive and negative ions on adjacent sites of the lattice create electric dipole moment oscillating with time.

In order to highlight the origin of the frequencies of vibration of a crystal lattice, it will be sufficient to illustrate the vibrations of a diatomic chain. The crystal lattice containing a couple of atoms (of masses m and M) reproduces periodically through the lattice parameter a.

If we use the equations of motion according to displacements x between atoms, the x coordinate may admit solutions for the n-th atom, it can be formed [6]:

$$x_n = A\sin(qna - \omega t) \qquad \text{(II.1)}$$

This equation describes a progressive wave of the pulsation $\omega = 2\pi\nu$ and the wave vector $\vec{q}$, such as: $q = 2\pi / \lambda$. So:

$$\omega^2 = \Lambda\left(\frac{1}{m}+\frac{1}{M}\right) \pm \Lambda\left[\left(\frac{1}{m}+\frac{1}{M}\right)^2 - \frac{4}{mM}sin^2(qa)\right] \qquad \text{(II.2)}$$

where Λ is the force constant and is associated with bands between atoms. Fig. II.1 shows that ν frequency appears as a sinusoidal function of q, with the period $2\pi/a$ (the range from $-\pi/a$ to π/a is called the Brillouin 1st zone). We are interested in optical phonons. In the center of the Brilloin zone, where $q \approx 0$ and $\lambda \approx \infty$, all atoms vibrate in the phase, and on the other hand the optical branch has a positive $\omega(0)$ frequency and the acoustical branch has a frequency which is null. In a contrast, on the edge of the zone, $q \approx \frac{\pi}{a}$ and $\lambda \approx 2a$, the ions vibrate in the opposite phases and the optical and acoustical branches have the positive $\omega\left(\frac{\pi}{a}\right)$ frequency.

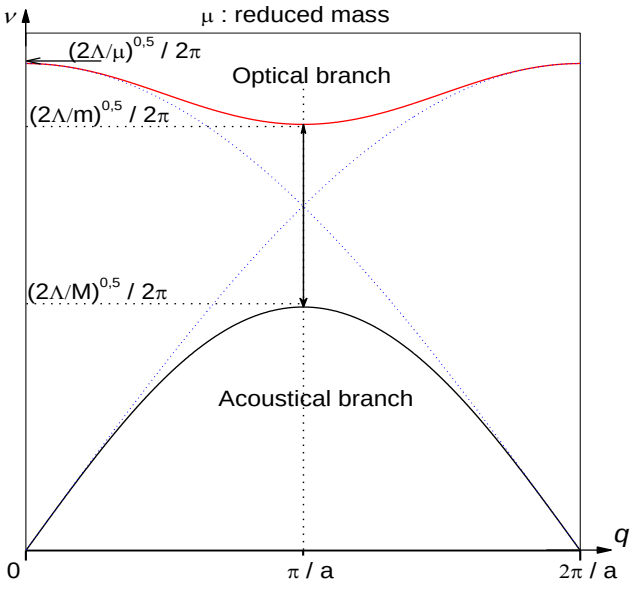

Figure II. 1 *– Dispersion of the frequencies of longitudinal vibrations of a diatomic chain.*

Raman scattering [8] is a non-linear process (NL) wherein an incident photon creates or annihilates one or more quasi-particles (phonon) and is distributed with a different energy. However, the interaction between matter and the excitation from monochromatic light radiation (laser) leads to elastic scattering (or Rayleigh scattering) and inelastic scattering with exchange of energy and change of the frequency. This inelastic scattering is called Raman scattering and is associated with optical phonons, while that the acoustical phonons are associated with the Brillouin scattering [7, 8]. A Raman spectrum consists of two symmetrical parts other than the frequency ν_0 of excitation beam, one called Raman Stokes, the other anti-Stokes Raman depending on the sign of the exchange (fig. II.3). A simplified energy diagram illustrating these concepts is shown in fig. II.4.

A light wave $\vec{E}_i$ with ω_i frequency and wave vector $\vec{k}_i$, passing through a crystal, can be scattered in all directions. In this case two processes are possible:

1. the frequency of the scattered wave may remain unchanged, it is the Rayleigh scattering (elastic scattering)
2. the frequency of the scattered wave can be modified by interactions with optical phonons (inelastic scattering) this is the Raman effect. In this case, the exchange process can create a phonon energy (Stokes scattering) or destroy one phonon (anti-Stokes scattering).

The conservation of energy and the quantity of movement in the Raman interaction lead to the establishment of selection rules for the first order scattering:

$$\hbar\omega_i = \hbar\omega_d \pm \hbar\Omega \qquad \text{(II.3)}$$

and

$$\hbar\overrightarrow{k_\iota} = \hbar\overrightarrow{k_d} \pm \hbar\vec{K} \qquad \text{(II.4)}$$

where $\overrightarrow{k_\iota}$ and ω_i characterize the incident photon, $\overrightarrow{k_d}$ and ω_d the scattered photon and $\vec{K}$ and Ω characterize the created or annihilated phonon by scattering.

By fixing the direction of the incident photons but also of scattered photons (to the detector), the spatial configuration adopted in an experiment (scattering has an angle of 90^o or backscattering) imposes the direction of wave vector $\vec{K}$ of the phonon whose creation or annihilation induced inelastic scattering of photons (fig. II.2).

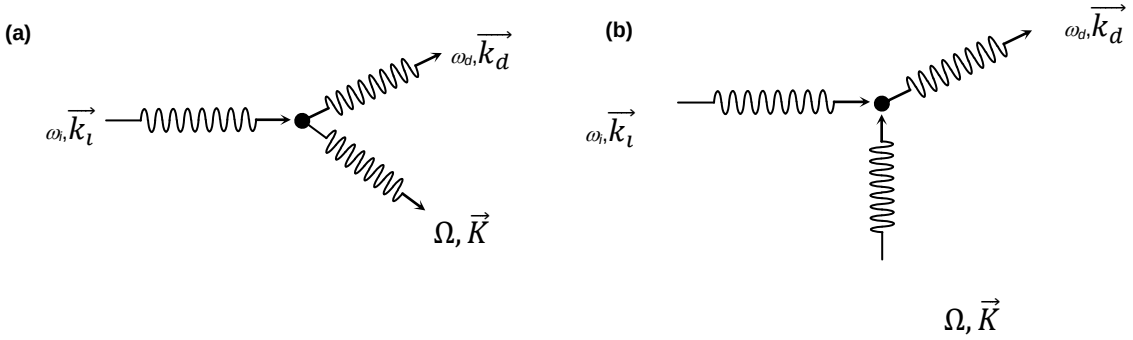

Figure II. 2 *- Raman scattering process Stokes (a) and Anti-Stokes (b).*

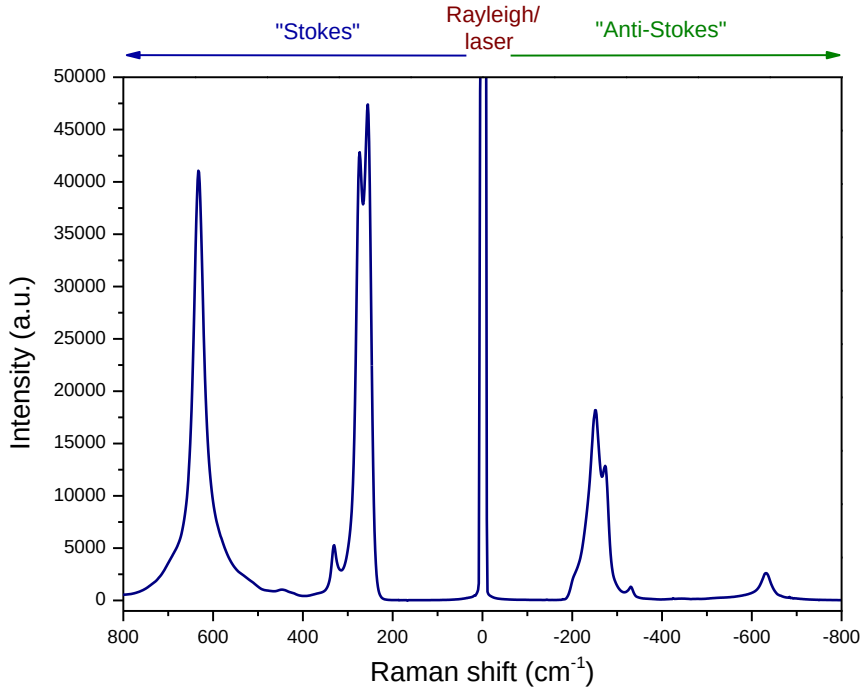

Figure II. 3*– Raman spectra illustrating Stokes and anti-Stokes scattering*

The mechanism of scattering can be described in a simple schematic way:

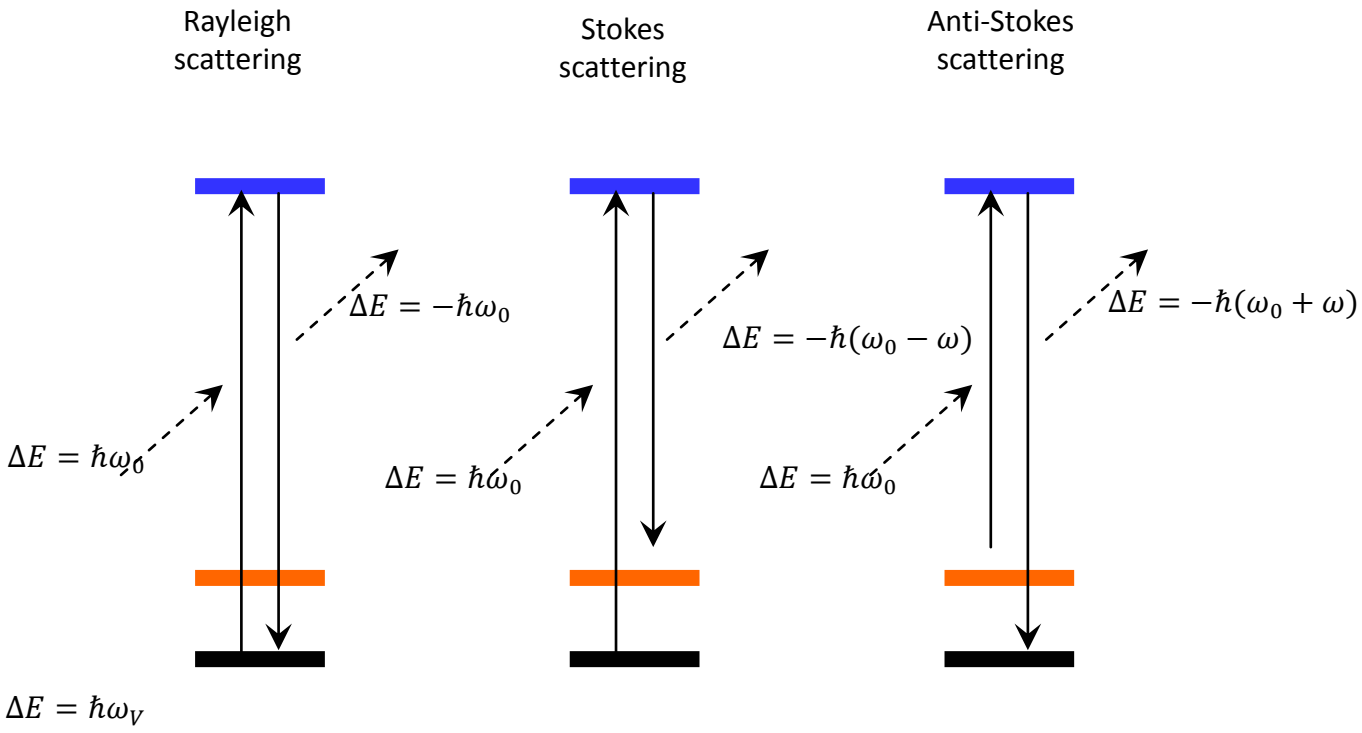

Figure II. 4*- interaction between a photon and the material characterized by the vibrational energy levels*

If we consider the field of the laser by the following form:

$$\vec{E} = \vec{E}_0 \cos(\omega t) \qquad \text{(II.5)}$$

And the displacement associated to the phonon by:

$$u = u_0 \cos(\Omega t) \qquad \text{(II.6)}$$

The induced electrical dipole will be presented as:

$$\vec{\mu} = \alpha\vec{E} + \frac{1}{2}\beta\vec{E}\vec{E} + \frac{1}{6}\gamma\vec{E}\vec{E}\vec{E} + \cdots \qquad \text{(II.7)}$$

where α is the tensor of the polarizability, β is the tensor of hyper-polarizability, γ is the tensor of the second hyper-polarizability. The first term of equation II.7 corresponds to the Raman scattering, the second one to the hyper-Raman scattering e t c.

In practice $\alpha \gg \beta \gg \gamma$, so $\mu \approx \alpha E$, which means:

$$\begin{cases} \mu_x = \alpha_{xx}E_x + \alpha_{xy}E_y + \alpha_{xz}E_z \\ \mu_y = \alpha_{yx}E_x + \alpha_{yy}E_y + \alpha_{yz}E_z \\ \mu_z = \alpha_{zx}E_x + \alpha_{zy}E_y + \alpha_{zz}E_z \end{cases} \quad \text{(II.8)}$$

In the case of the polarized wave, we have $E_x \neq 0$ and μ_x, μ_y, μ_z can be other than zero, the direction of the induced dipole will be thus different to the direction of the incident electric field. The polarization of the scattered light can be different to the polarization of the incident light. The development of the polarizability around the position of the equilibrium can be described as:

$$\alpha(u) = \alpha_0 + \frac{\partial\alpha}{\partial u}\Big|_{u_0} u + \cdots \quad \text{(II.9)}$$

$$\vec{\mu} = \left(\alpha_0 + \frac{\partial\alpha}{\partial u}\Big|_{u_0} u\right)\vec{E} = (\alpha_0 + \alpha_1 u)\vec{E} \quad \text{(II.10)}$$

The incident field $E = E_0\cos(\omega_0 t)$, thus:

$$\vec{\mu} = \left(\alpha_0 + \frac{\partial\alpha}{\partial u}\Big|_{u_0} u\right)E_0\cos(\omega_0 t) \quad \text{(II.11)}$$

II.II.2 – Selection rules

The intensity of the scattered radiation can be calculated from the average of the power radiated by the induced oscillating dipole. It can be expressed as:

$$I_R \propto |\vec{e}_i M_R \vec{e}_d|^2 \quad \text{(II.12)}$$

where $\vec{e}_i$ is the polarization of the incident wave, $\vec{e}_d$ is the polarization of the scattered wave and M_R is the Raman tensor which presents the dependence of the modulation of the polarizability:

$$M_R = \alpha_1 = \frac{\partial\alpha}{\partial u} \quad \text{(II.13)}$$

The symmetries of the system as well as vibration modes fix the form of the Raman tensor. The selection rules are presented as $\left.\frac{\partial \alpha}{\partial u}\right|_{u_0} \neq 0$, which means that the mode is only active in Raman only when the mentioned condition exists.

Concerning the Stokes and anti-Stokes scattering, scattered intensity depends on the involved population levels. This population is defined by the Bose-Einstein factor:

$$n(\omega) = \frac{1}{e^{\frac{\hbar\omega}{k_B T}} - 1} \qquad \text{(II.14)}$$

where k_B is the constant of Boltzmann.

For the vibrational mode *j*, the dependence of the scattered Raman intensity in different thermal population factors, $n(\omega_j) + 1$ and $n(\omega_j)$ for the Stokes and anti-Stokes processes respectively, implies that the corresponding intensities are different, and their relationship is determined by Boltzmann factor:

$$\frac{I_{anti-Stokes}(\omega_j)}{I_{Stokes}(\omega_j)} = \frac{n(\omega_j)}{n(\omega_j)+1} = e^{-\frac{\hbar\omega}{k_B T}} \qquad \text{(II.15)}$$

Three types of scatterings are available:

I) backscattering at 180 ° (angle between incident laser and scattered beam)
II) scattering at right angle 90 °
III) forward scattering

Several configurations are possible depending on the type of the scattering. A(αβ)B(Ā) where A and B are the directions of the incident and scattered waves, α and β show the direction of the polarization of each beam respectively. In the x y z axis system three geometries and twelve configurations are possible for each type of scattering. (AB) is called the scattering plane, Raman active modes are called transverse optical (TO) and longitudinal optical (LO) modes according to its polarization is perpendicular or parallel to the direction of phonon propagation (or wave vector transfer).

II.II.3 – Application on the Lithium Niobate crystals

The analysis of the vibrational modes of Lithium Niobate (LN) can be simplified by taking into account its symmetry properties. Indeed, at room temperature LN is uniaxial and belongs to the C3v space group or 3m symmetry group [9, 10]. The unit cell contains 10 atoms and is rhomboedral which involves 30 degrees of freedom. The irreducible representations of the optical vibrational modes at the center of the Brillouin zone $q \approx 0$, are given by:

$$\Gamma = 4A_1(Z) + 9E(X) + 9E(Y) + 5A_2 \qquad \text{(II.16)}$$

Modes of A_1 and E symmetry are active in Raman [11-13] and infrared (IR), while modes of A_2 symmetry are inactive in Raman and IR. The non-zero components associated to the Raman tensor are given by:

$$A_1(Z) = \begin{pmatrix} a & 0 & 0 \\ 0 & a & 0 \\ 0 & 0 & b \end{pmatrix} \quad E(X) = \begin{pmatrix} 0 & c & d \\ c & 0 & 0 \\ d & 0 & 0 \end{pmatrix} \quad E(Y) = \begin{pmatrix} c & 0 & 0 \\ 0 & -c & d \\ 0 & d & 0 \end{pmatrix} \qquad \text{(II.17)}$$

where the letters X, Y and Z are the directions of polarizations of the modes referring to the crystallographic axes, whereas the components of the tensor refer to the rectangular coordinate system x, y, and z. Expected modes for LN crystal according to selection rules in backscattering and forward Raman are given in tables II.1 and II.2:

Configuration	**Expected modes according to selection rules**
$X(YY)\overline{X}$	A_1(a)[TO]+E(-c)[TO]
$X(YZ)\overline{X}$	E(d)[TO]
$X(ZY)\overline{X}$	E(d)[TO]
$X(ZZ)\overline{X}$	A_1(b)[TO]
$Y(XX)\overline{Y}$	A_1(a)[TO]+E(c)[LO]
$Y(XZ)\overline{Y}$	E(d)[TO]

$Y(ZX)\overline{Y}$	E(d)[TO]
$Y(ZZ)\overline{Y}$	A_1(b)[TO]
$Z(YX)\overline{Z}$	E(c)[TO]
$Z(XY)\overline{Z}$	E(c)[TO]
$Z(XX)\overline{Z}$	A_1(a)[LO]+E(c)[TO]
$Z(YY)\overline{Z}$	A_1(a)[LO]+E(-c)[TO]

Table II 1*– Expected modes according to Raman selection rules in backscattering*

Configuration	**Expected modes according to selection rules**
X(YY)X	A_1(a)[TO]+E(-c)[TO]
X(YZ)X	E(d)[TO]
X(ZY)X	E(d)[TO]
X(ZZ)X	A_1(b)[TO]
Y(XX)Y	A_1(a)[TO]+E(c)[LO]
Y(XZ)Y	E(d)[TO]
Y(ZX)Y	E(d)[TO]
Y(ZZ)Y	A_1(b)[TO]
Z(YX)Z	E(c)[TO]
Z(XY)Z	E(c)[TO]
Z(XX)Z	A_1(a)[LO]+E(c)[TO]
Z(YY)Z	A_1(a)[LO]+E(-c)[TO]

Table II 2*– Expected modes according to Raman selection rules in forward scattering*

Configuration	**Expected modes according to selection rules**
X(ZZ)Y	A_1(b)[TO]
X(ZX)Y	E(d)[TO+LO]
X(YZ)Y	E(d)[TO+LO]

X(YX)Y	E(c)[TO+LO]
X(ZY)Z	E(d)[TO]
X(ZX)Z	Quasi-modes
X(YY)Z	E(-c)[TO] + Quasi-modes
X(YX)Z	Quasi-modes
Z(XZ)Y	E(d)[TO]
Z(YX)Y	E(c)[TO]
Z(YZ)Y	Quasi-modes
Z(XX)Y	Quasi-modes

***Table II 3**– Expected modes according to Raman selection rules in scattering at 90^o*

In the configuration at 90^o quasi-modes appear, which means that phonons are not purely of a A_1 or E symmetry and/or have frequency intermediate between frequencies of TO and LO modes [14]. The indication E[TO+LO] means that the modes E[TO] and E[LO] can be simultaneously present. Within our study we found out that according to above tables there is no necessity to perform the measurements for scattering at 90^o because by the use of results on backscattering (or forward scattering Raman measurements) it was possible to obtain in principle all E[TO], E[LO], A_1[TO] and A_1[LO] modes.

According to the calculation of normal modes by Caciuc *et al*. [15] $A_1[TO_1]$ phonon is associated to the out of phase [16] motion of Nb and O ions along the ferroelectric z axis, $A_1[TO_2]$ is associated to the vibration of Li and O ions along the opposite direction to z axis and A1[TO4] corresponds to a stretching motion of oxygen octahedra (Figure II.5).

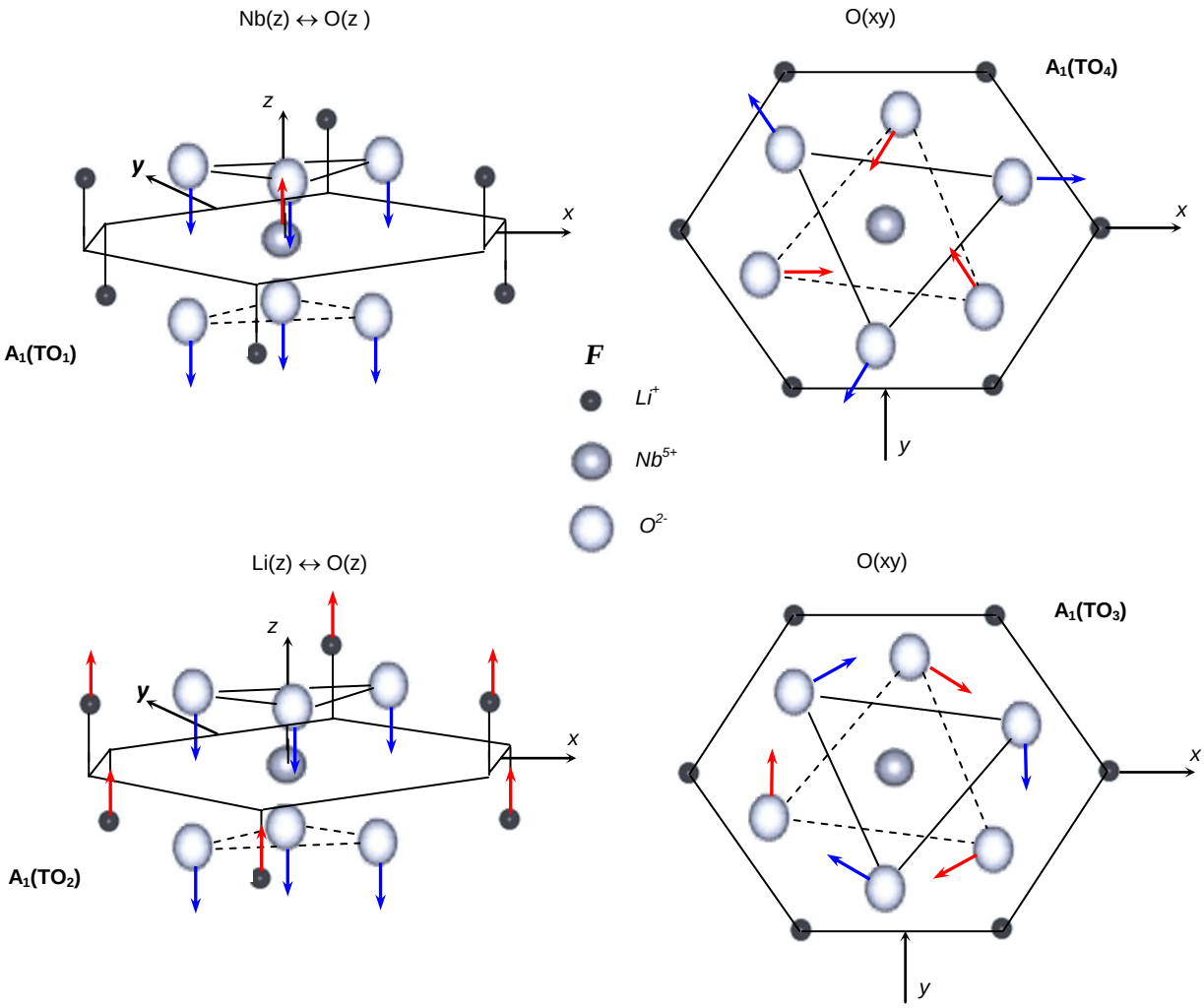

Figure II. 5– *Representation of different A_1[TO] vibrations in LN [17]*

$A_1[TO_3]$ is associated to the rigid rotation of the oxygen octahedra arount z. The motion associated with E phonons is more complicated since it involves generally Li, Nb and various O ions. Only 3 modes as follows can be simply described.

$E[TO_1]$ mode (as the mode $A_1[TO_1]$) is associated to the vibration of Nb/O in B site, and the $E[TO_6]$ mode (as the mode $A_1[TO_2]$) is associated to the vibration of Li/O in A site and the $E[TO_8]$ (as the mode $A_1[TO_4]$) corresponds to a stretching motion of oxygen octahedra.

Now after these generalities on Raman scattering and selection rules applied to LN, I will describe Raman data obtained on undoped congruent LN crystal by means of back scattering within various configurations.

II.II.4 – Characteristics on Raman spectrometer

A Raman spectrometer includes (1) a laser source, (2) a sample holder, (3) optics for a collection of the scattered light and coupling with the spectrum analyzer (spectrometer), (4) spectrometer, (5) a very sensitive light detector, and (6) electronics for acquisition and treatment of spectral data (Fig.II.6).

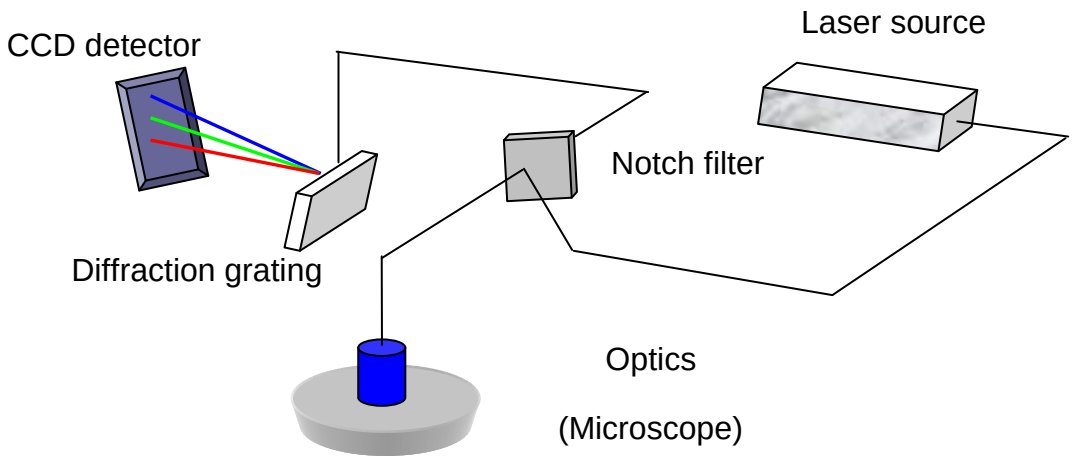

Figure II. 6– *Principle of Raman spectrometer*

To carry out required measurements for our research the spectrometer Horiba JobinYvon ARAMIS (Fig. II.7) was utilized which has automated wavelength selection up to 4 lasers and a

filters, adapted for each laser sources: 405nm (diode), 532 (diode) and 785nm (diode) lasers and an internal He-Ne 632.8 nm laser. Spectrometer is also equipped with a confocal microscope which gives a possibility to analyze the focal point. Different objectives (5x, 10x, 50x, 100x) lead to observe and realize the measurements of different volumes of the sample. There is a possibility to polarize the incident and scattered light (linear and circular). It is possible to perform a mapping on the surface, in depth or in volume of the sample. For all measurements presented in thesis, a calibration procedure was done using a Silicon wafer.

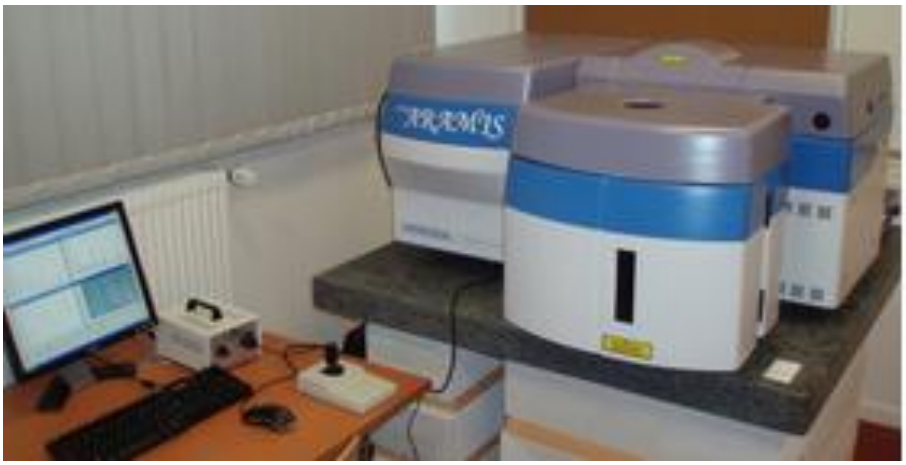

***Figure II. 7**– Raman spectrometer (Horiba JobinYvon ARAMIS)*

II.III – Features of Raman spectra on a crystal of Lithium Niobate

The Raman spectra are specific to the material under study and each line corresponds to a movement of atoms in the crystal lattice. Here Raman lines corresponding to 1st order scattering are described by Lorentzian. The model of Lorentz oscillator is used to describe the response of a damped harmonic oscillator, taking into account the effect of the temperature due to the population factor of Bose-Einstein. We report here our results obtained in various configurations of polarized Raman scattering.

II.III.1 – A_1[TO] modes

We expect to obtain four A_1[TO] modes for the $Y(ZZ)\overline{Y}$ configuration according to Raman selection rules.

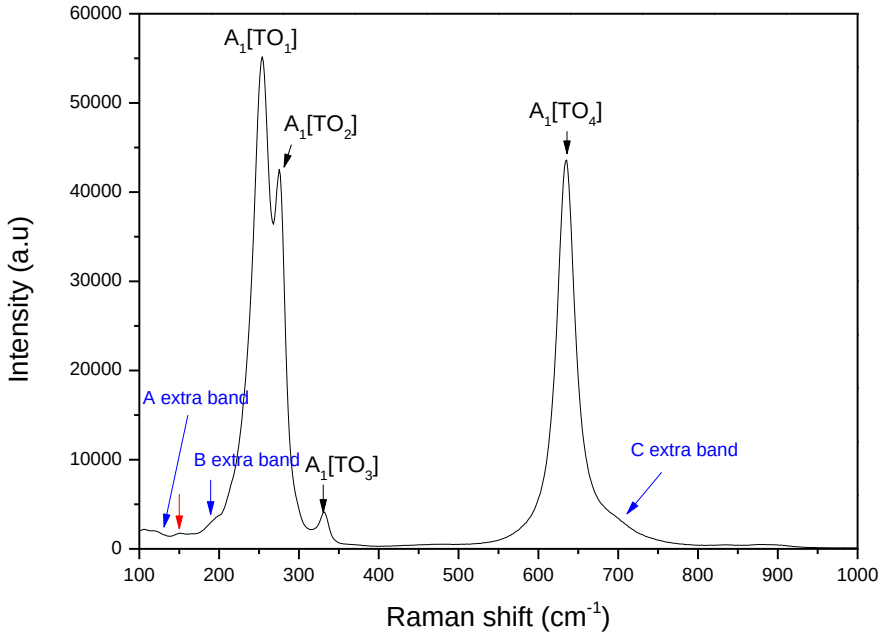

Figure II. 8– *Raman spectrum of $A_1[TO]$ modes measured in $Y(\boldsymbol{ZZ})\overline{\boldsymbol{Y}}$configuration for congruent LN sample at room temperature. By a red arrow in the figure it is mentioned a leakage of the E[TO1] mode*

The peaks were fitted using the Lorentzian function by *fityk* software (Appendix B) so the values of frequencies of each mode were obtained, and are given in the Table II.4.

Mode	***at 93K (cm^{-1})***	***at 300K (cm^{-1})***	***Kaminow et al. (cm^{-1}) (300K)***
$A_1[TO_1]$	256.5	251.6	253.4
$A_1[TO_2]$	278 .5	274	276.7
$A_1[TO_3]$	334.3	331.7	333.6
$A_1[TO_4]$	634.7	631.4	633.3

Table II 4– *Frequencies of $A_1[TO]$ modes of congruent LN obtained at 93K, 300K and comparison with values by Kaminow et al. [18]*

Wide extra bands are detected around 121 cm^{-1} (A), around 194cm^{-1} (B) and 701cm^{-1} (C). These extra bands are attributed to two-phonon scattering, probably due to a breaking of selection caused by the presence of intrinsic defects, which always are present in the LN

crystal of congruent composition. The intensities of extra bands increase with temperature much faster than the lines of the first order, as it is shown in the fig. II.9.

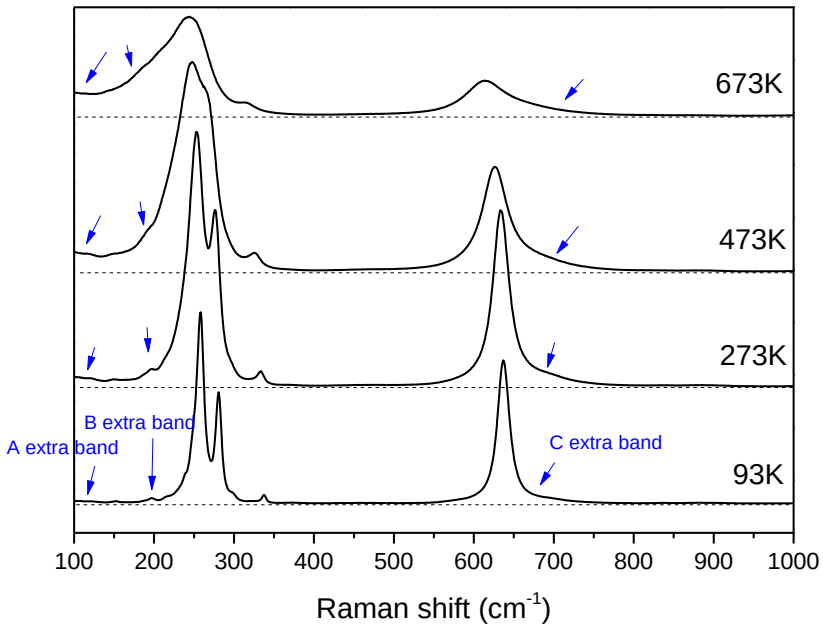

***Figure II. 9**- Raman spectra of $A_1[TO]$ modes measured in $Y(\boldsymbol{ZZ})\overline{\boldsymbol{Y}}$configuration for congruent LN sample as a function on temperature*

Another proof is given by the measurements at low temperature. While the first order Raman lines are narrow and better separated, the extra bands nearly disappear in the spectrum $Y(ZZ)\overline{Y}$ recorded at 93K as illustrated in the figure II.10.

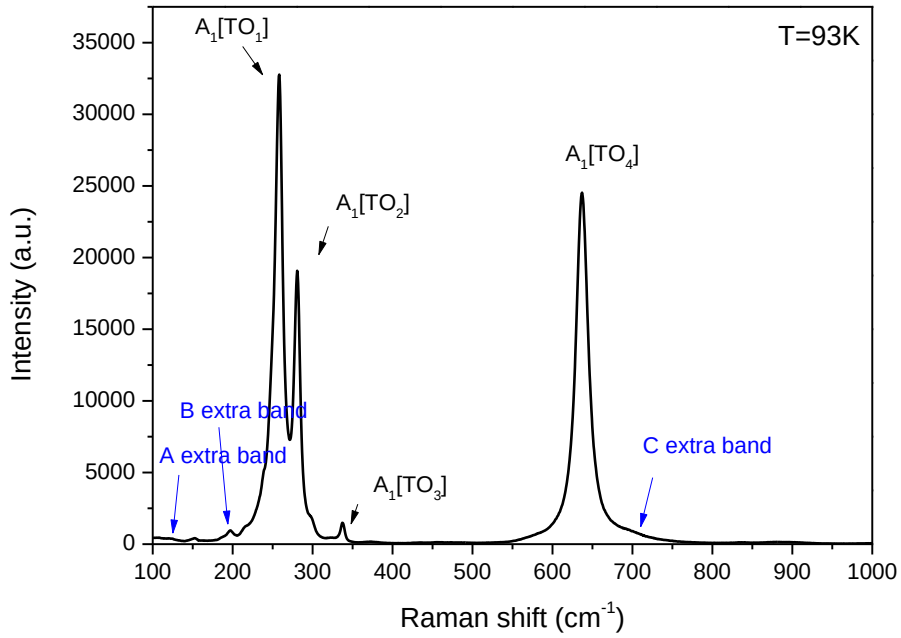

Figure II. 10– *Raman spectrum of $A_1[TO]$ modes measured at 93K in $\boldsymbol{Y}(\boldsymbol{ZZ})\overline{\boldsymbol{Y}}$ configuration for congruent LN sample*

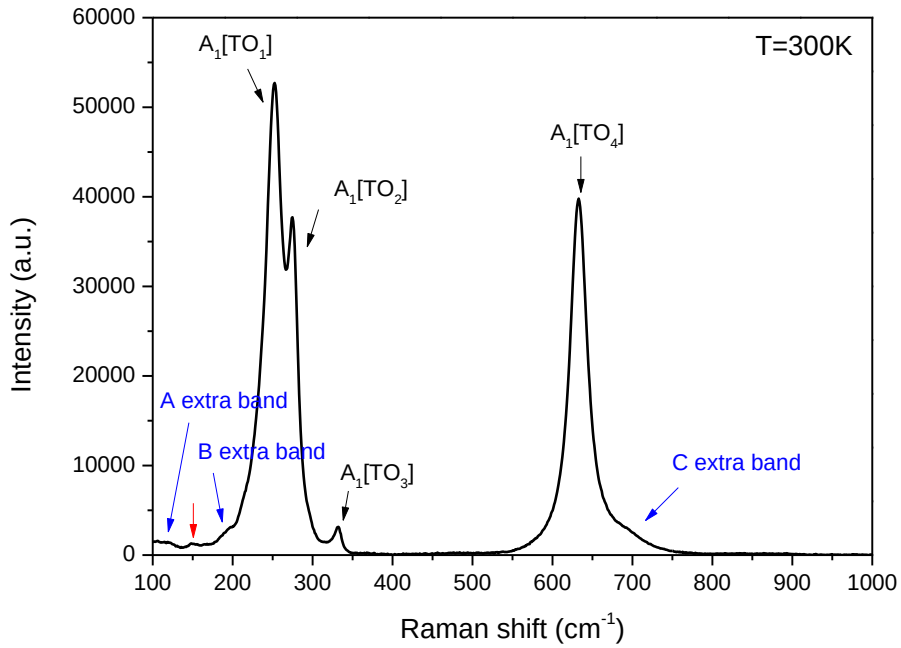

Figure II. 11– *Raman spectrum of A1[TO] modes measured in $\boldsymbol{X}(\boldsymbol{ZZ})\overline{\boldsymbol{X}}$configuration for congruent LN sample obtained at room temperature*

The same Raman modes (A_1[TO]) are detected for the configuration $X(ZZ)\overline{X}$ as expected according to selection rules (Fig. II.11).

II.III.2 – E[TO] modes

Raman lines corresponding to E[TO] modes can be detected in several configurations. Some of them are strictly equivalent (since X=Y) but in some cases a different activation is expected according to the involved polarizability tensor component ($XZ \neq XY$).

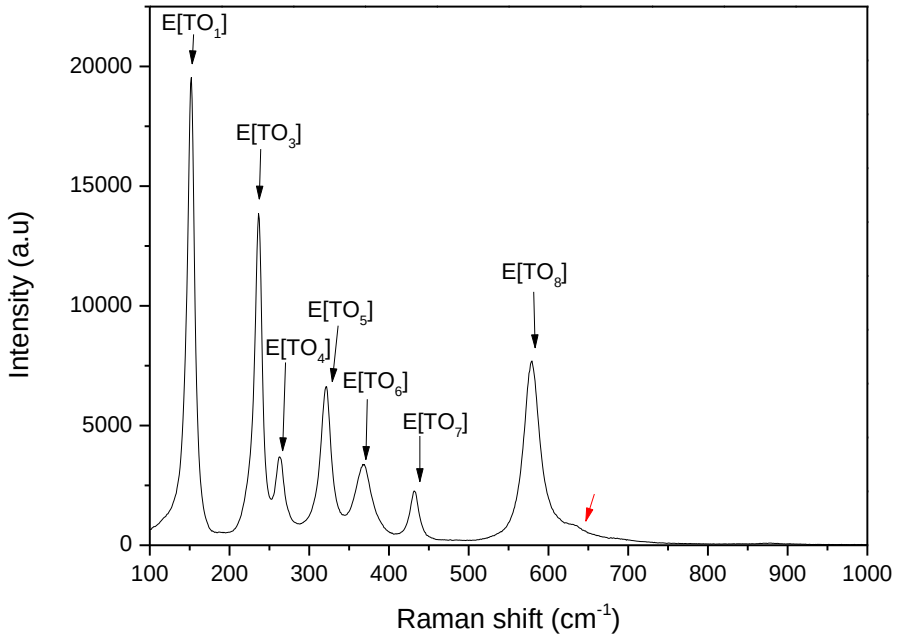

Figure II. 12– *Raman spectrum of E[TO] modes measured in* $\boldsymbol{Y(ZX)\overline{Y}}$ *configuration for congruent LN sample. There is a leakage of the mode A_1[TO_4] mode shown by a red arrow (see below the origins of appearance of leakages)*

Raman spectrum recorded in the configuration $Y(ZX)\overline{Y}$ and $Y(XZ)\overline{Y}$ are shown in the figures II.12 and II.13. Seven lines are clearly detected instead of nine which are expected. The modes E[TO_2] and E[TO_9] are absent.

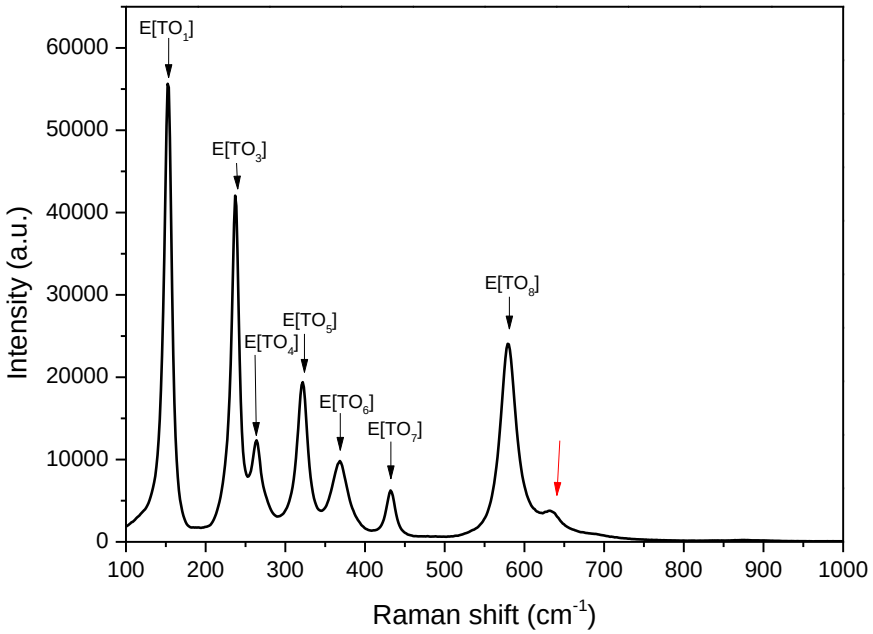

***Figure II. 13**– Raman spectrum of E[TO] modes measured in $\boldsymbol{Y(XZ)\overline{Y}}$ configuration for congruent LN sample.*

Comparing the intensities of the lines A_1[TO] and E[TO] carried out for the configurations $Y(ZZ)\overline{Y}$ and $Y(ZX)\overline{Y}$ one can notice that the intensity of A_1[TO] modes are nearly 3 times higher than the intensity of E[TO] modes.

Spectra obtained for the configurations $X(ZY)\overline{X}$ and $X(YZ)\overline{X}$ are identical to those with the Y direction of propagation. By a contrast, spectra in the configurations $Z(XY)\overline{Z}$ and $Z(YX)\overline{Z}$ the E[TO] modes are slightly different (figs.II.14, II.15). Here component *c* of the Raman tensor (instead of *d*) is involved in the scattering and observation of E[TO] lines. The spectra exhibit several differences compared with those above. At first the two missing lines are now detected.

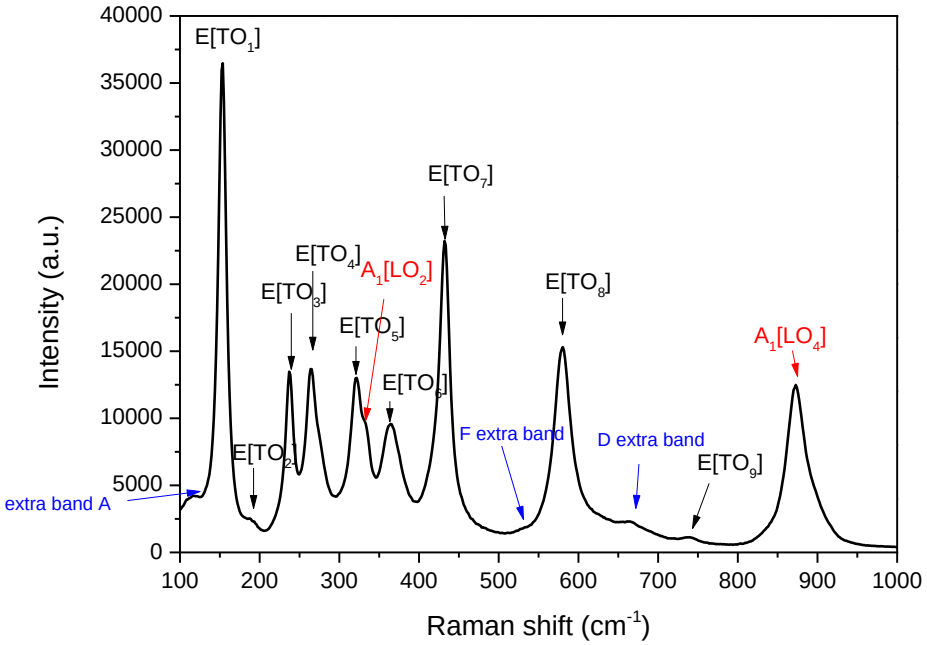

Figure II. 14– *Raman spectrum of E[TO] modes measured for* $\boldsymbol{Z(XY)\overline{Z}}$ *configuration for congruent LN sample*

There are leakages of $A_1[LO_2]$ and $A_1[LO_4]$ modes and additional extra bands (A,F and D) in the spectra. It has to be mentioned that in the case of leakage due to the misorientation of the polarization when there are Raman lines of the other symmetry it has to be detected all of them: for example in the case of fig.II.14, due to the misorientation of polarizers (or with respect of polarizers) along X or Y, we can also observe the modes $A_1[LO]$ and E[TO] corresponding to the configuration $Z(XX)\overline{Z}$ or $Z(YY)\overline{Z}$. In fig.II.14 we obtain $A_1[LO_2]$ and $A_1[LO_4]$ as they are the most intense among the lines recorded in configurations $Z(XX)\overline{Z}$ or $Z(YY)\overline{Z}$.

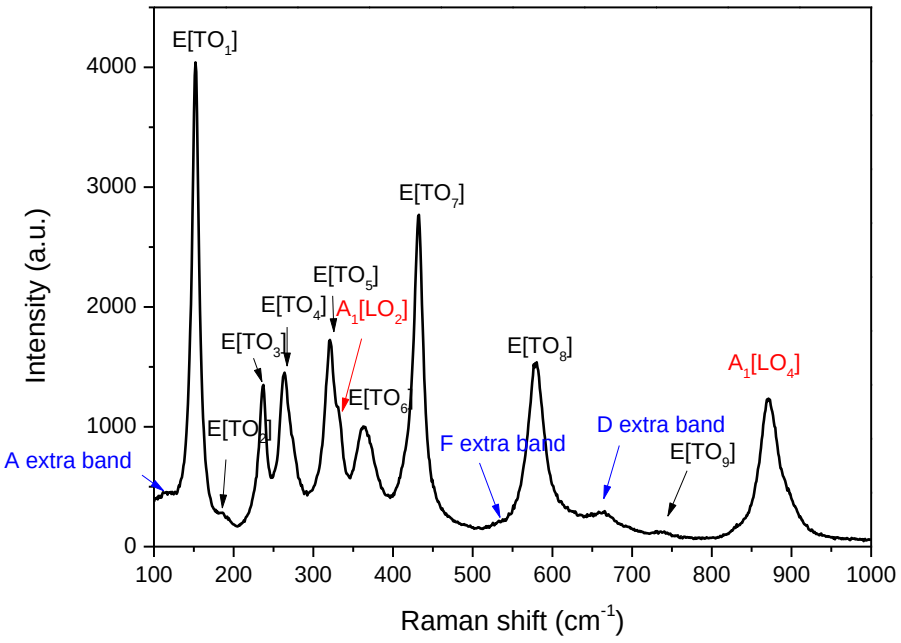

Figure II. 15– *Raman spectrum of E[TO] modes measured for* $\boldsymbol{Z(YX)\bar{Z}}$ *configuration for congruent LN sample*

Modes	***At 93K (cm^{-1})***	***At 300K (cm^{-1})***	***Ridah et al. (cm^{-1}) (300K)***
E[TO_1]	151.6	150.8	152.8
E[TO_2]	187	186	177.3
E[TO_3]	236.4	235.8	238.3
E[TO_4]	260.6	260	264.2
E[TO_5]	322.4	321	321.9
E[TO_6]	370.6	368	369.5
E[TO_7]	432.1	431.6	432.4
E[TO_8]	579.8	578.3	580.0
E[TO_9]		738	609.8

Table II 5 - *Frequencies of E[TO] modes measured at 93K and 300K for* $\boldsymbol{Y(XZ)\bar{Y}}$ *and* $\boldsymbol{Z(XY)\bar{Z}}$ *configurations for congruent LN sample. Results are compared with values reported by Ridah et al. [16]*

If compared with results reported by Ridah et al. on a stoichiometric crystal it can be noted that, except for the lines TO_2 and TO_9 introduced and detectable with difficulties, the frequency at the same temperature is always smaller in the congruent crystal than in the stoichiometric sample.

II.III.3 – A_1[LO] modes

According to Raman selection rules and by contrast to A1[TO] modes there isn't any Raman configuration that allows to observe only A_1[LO] modes. They are present in combination with other modes here (E[TO] lines), as for the configurations Z(XX)$\overline{Z}$ and Z(YY)$\overline{Z}$. The four expected A_1[LO] modes are detected (figure II.16):

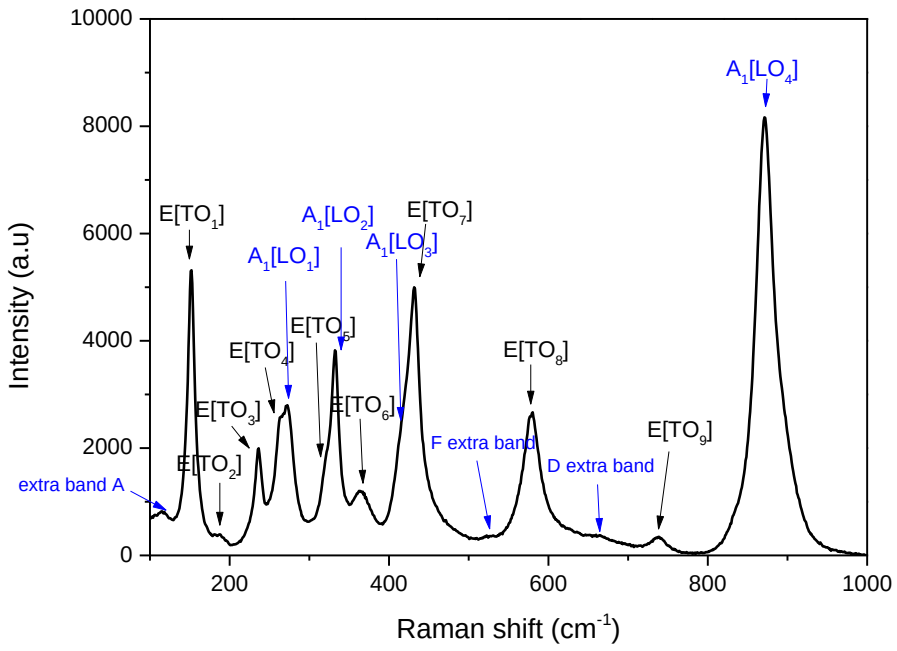

***Figure II. 16**– Raman spectuma of A1[LO] and E[TO] modes measured in $\boldsymbol{Z(XX)\overline{Z}}$ configuration for congruent LN sample*

In addition with all nine E[TO] lines and four A_1[LO] modes some extra bands (A, F and D) are detected. The same lines are observed in the configuration $Z(YY)\overline{Z}$ as it was expected according to selection rules.

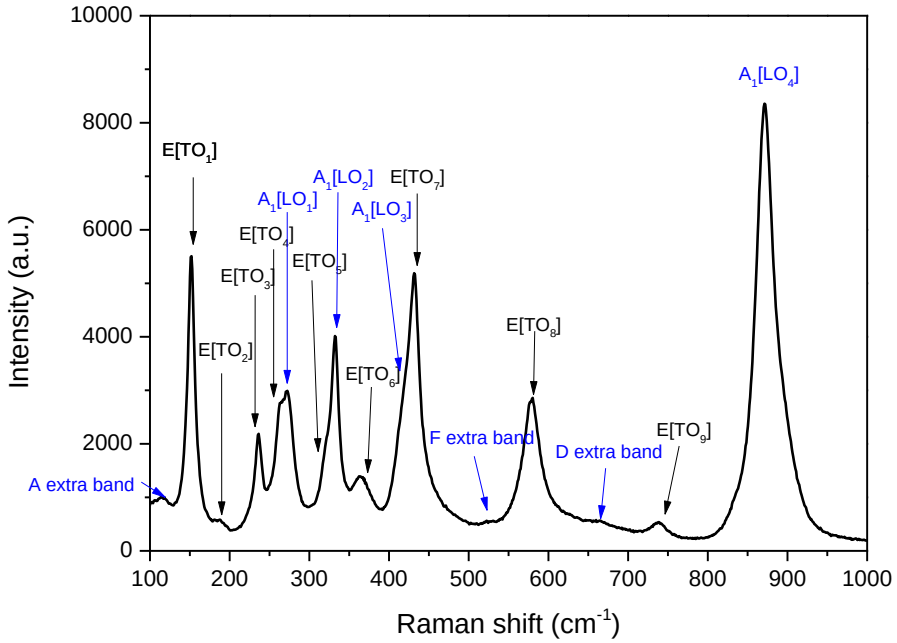

***Figure II. 17**– Raman spectra of A1[LO] and E[TO] modes measured in $\boldsymbol{Z(YY)\bar{Z}}$ configuration for congruent LN sample*

Mode	***at 300K (cm^{-1})***	***Kaminow et al. (cm^{-1}) 300K***
$A_1[LO_1]$	272.4	273.0
$A_1[LO_2]$	332.1	331.0
$A_1[LO_3]$	419.3	428.0
$A_1[LO_4]$	871.2	874.0

***Table II 6**–Frequencies of A1[LO] modes of congruent LN obtained at 300K and comparison with values by Kaminow et al. [18]*

II.III.4 – E[LO] modes

Similar to the case of A_1[LO] modes there is no Raman configuration which allows to obtain only E[LO] modes. They are also present with other modes, for example in the configuration $Y(XX)\overline{Y}$ for which they are combined with A_1[TO] modes (Figure II.18).

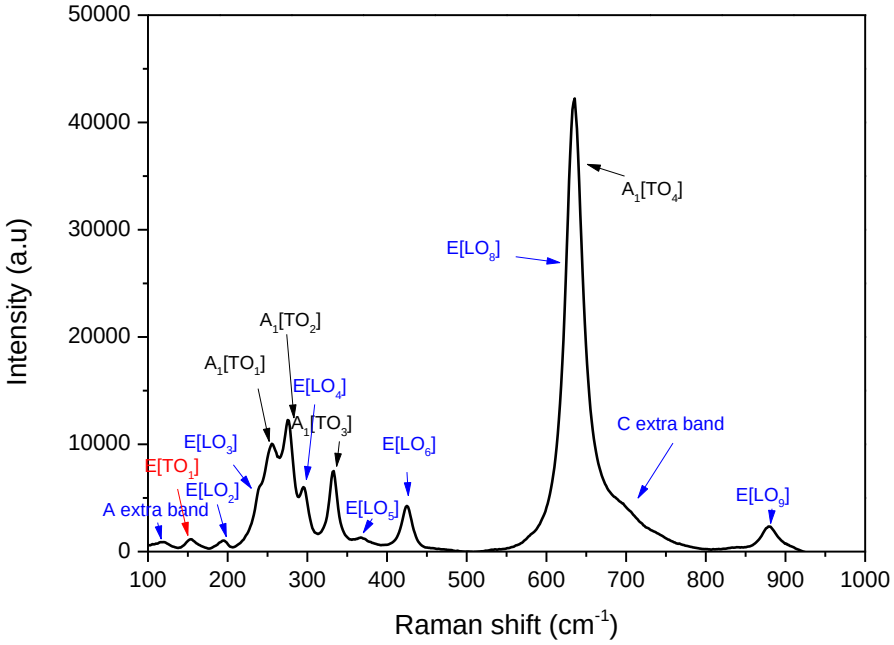

***Figure II. 18**– Raman spectrum of E[LO] and A1[TO] modes measured in $\boldsymbol{Y(XX)\overline{Y}}$ configuration for congruent LN sample*

There are seven E[LO] and 4 A_1[TO] lines are detected, in addition with a leakage of the mode E[TO_1] and 2 extra bands (A and C). The same bands are present for the configuration $X(YY)\overline{X}$, as expected according to the selection rules (Figure II.19).

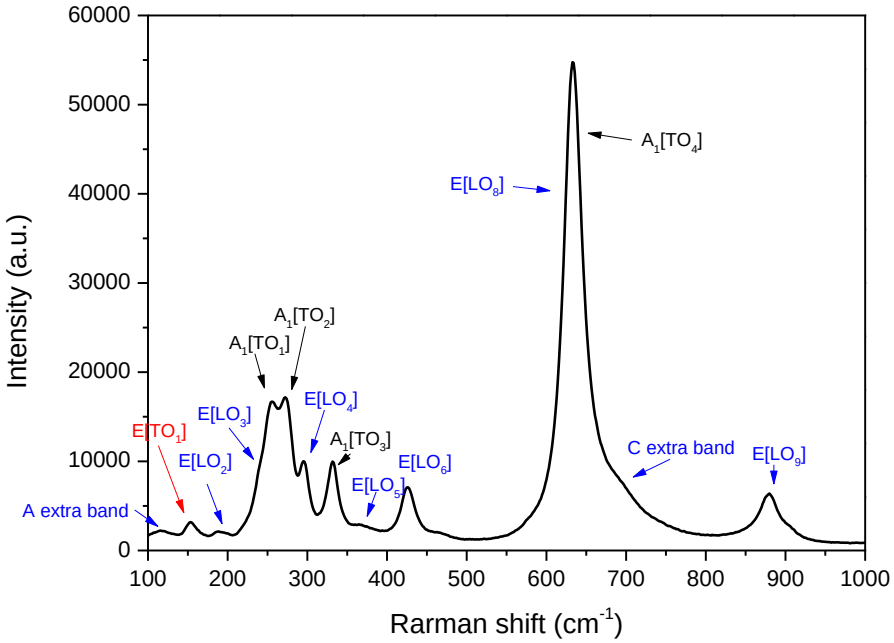

Figure II. 19– *Raman spectrum of E[LO] and A1[TO] modes measured in* $\boldsymbol{X(YY)\overline{X}}$ *configuration for congruent LN sample*

Modes	At 300K(cm^{-1})	Ridah et al. (cm^{-1}) (300K)
$E[LO_1]$		186.5
$E[LO_2]$	194.3	194.9
$E[LO_3]$	238.4	240.4
$E[LO_4]$	295.0	299.0
$E[LO_5]$	365.8	345.0
$E[LO_6]$	425.0	424.2
$E[LO_7]$		456.0
$E[LO_8]$	625.0	625.0
$E[LO_9]$	880.0	878.0

Table II 7– *Frequency of E[TO] and E[LO] modes of congruent LN. Results are compared with the values reported by Ridah et al [16]*

II.IV – Raman spectra on the congruent LN powder and unpolarized crystal

In principal in a powder of LN we don't have any privileged direction and therefore Raman spectra should behave regardless the polarization. In this part we compare the polarized and non-polarized scattered spectra of the LN powder and crystal as well.

II.IV.1 – Congruent LN powder

We performed Raman measurements on LN powder. Different spectra were recorded with or without beam polarization. The Raman spectrum presented in fig. II.20 is recorded without any polarization.

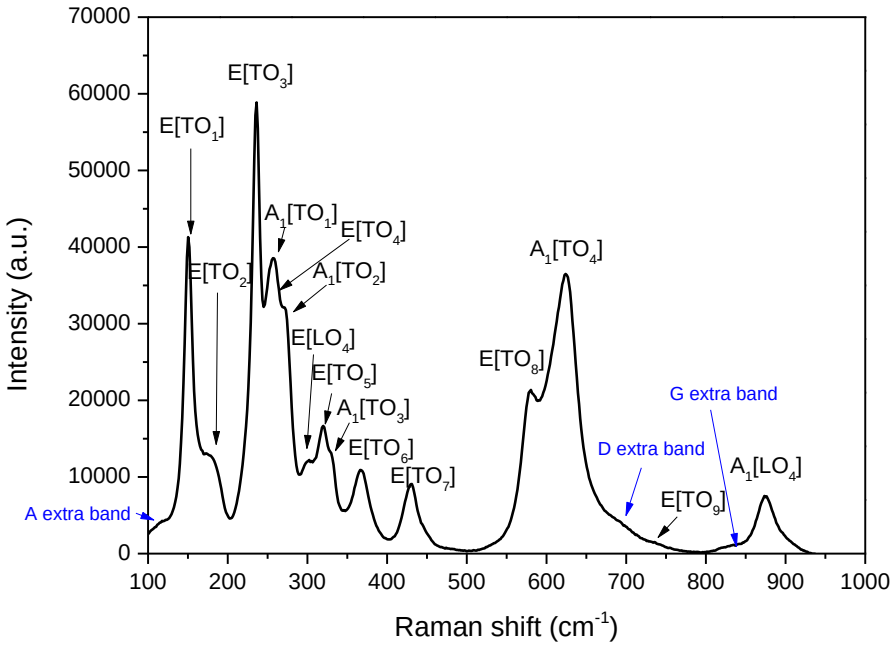

***Figure II. 20**– Non-polarized Raman spectrum of LN congruent powder, integration time 1s*

First-order Raman lines are detected. They correspond to different mode symmetries. They were assigned to A_1[TO], E[TO], E[LO] and A_1[LO] according to the analysis described above on polarized spectra for LN crystal. Some extra bands are present (A, D and G). The same spectrum was obtained for the case of polarizing the incident and scattered light parallel and perpendicular to each other (figs. II.21, II.22).

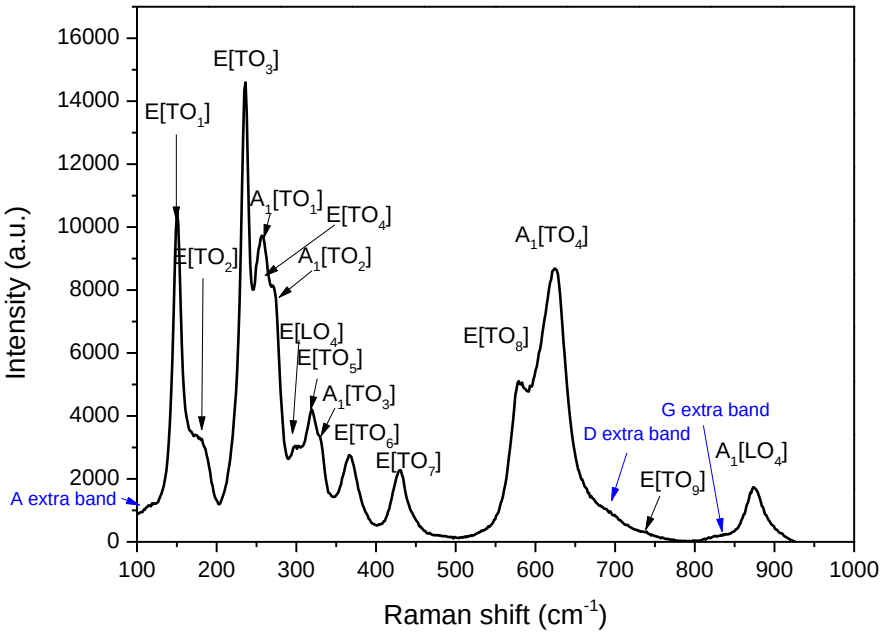

Figure II. 21 *– Raman spectrum of powder of congruent LN, xx polarization, x axis of the setup is defined as the horizontal direction comparing to the laser.*

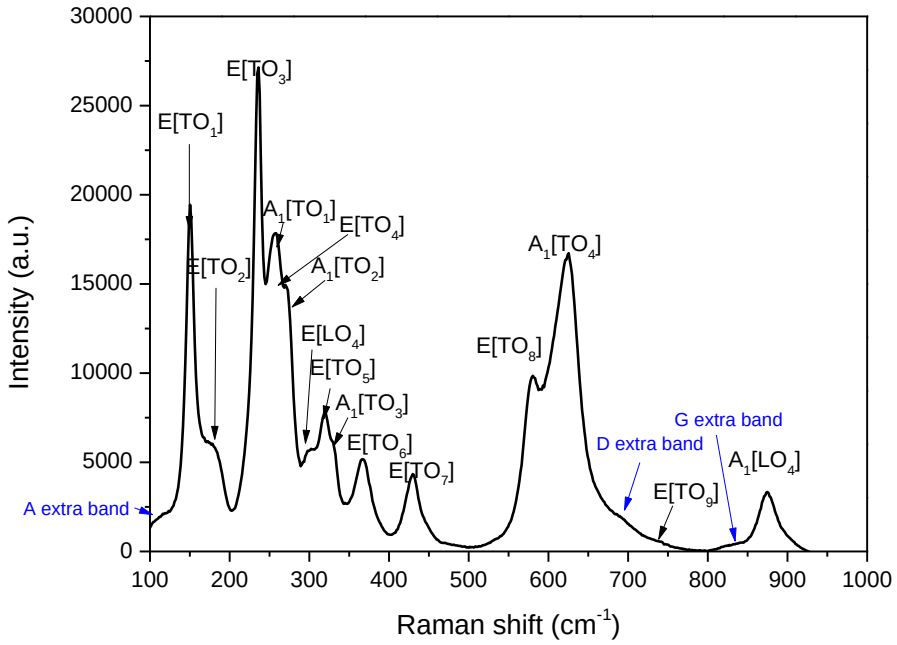

Figure II. 22*– Raman spectrum of powder of congruent LN, xy polarization*

In both cases the integration time for recording the spectra is equal to 1s. The difference of intensities can be explained by the fact that 2 different polarizers are utilized as analyzer (x and y directions, which have probably different characteristics. As expected the Raman spectra of the powder is insensitive to the polarization choice (crossed or parallel polarizers). In addition, it is to be noted that both spectra are exactly similar to the non-polarized spectrum. This means that irrespectively of the beam polarization, the spectrum of powder contains main information of the Raman spectra of LN. In other terms as the grains are completely misoriented, such a spectrum is like a contribution of all directions.

II.IV.2 – Unpolarized spectra on congruent LN crystal

Non-polarized measurement was recorded also for the LN congruent crystal (figure II.23).

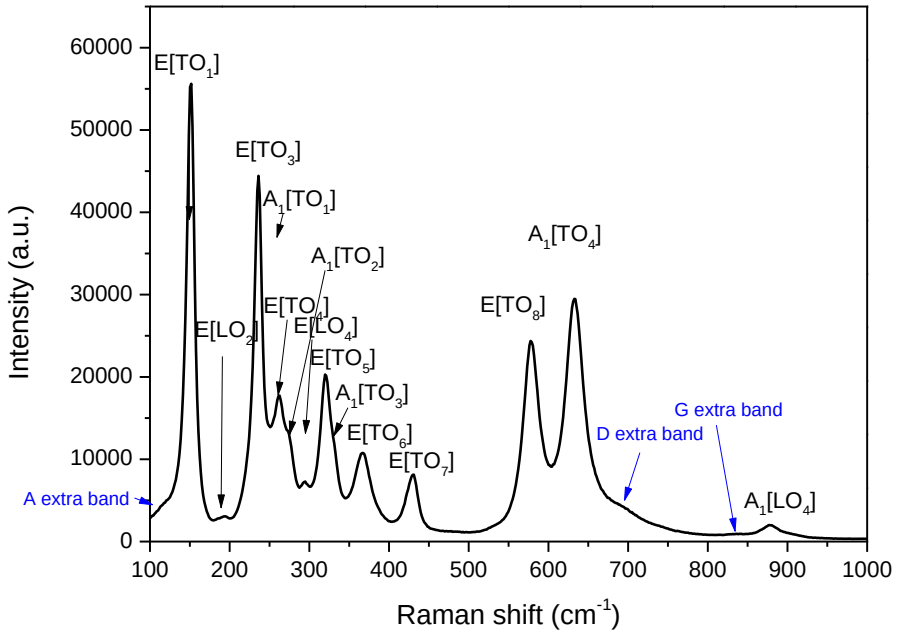

Figure II. 23– *Non-polarized Raman spectrum of congruent LN crystal*

In the non-polarized spectra we obtain the main Raman lines. It represents the sum of polarized spectra (crossed and parallel). This spectrum is compared with the non-polarized one of the LN powder (fig.II.24).

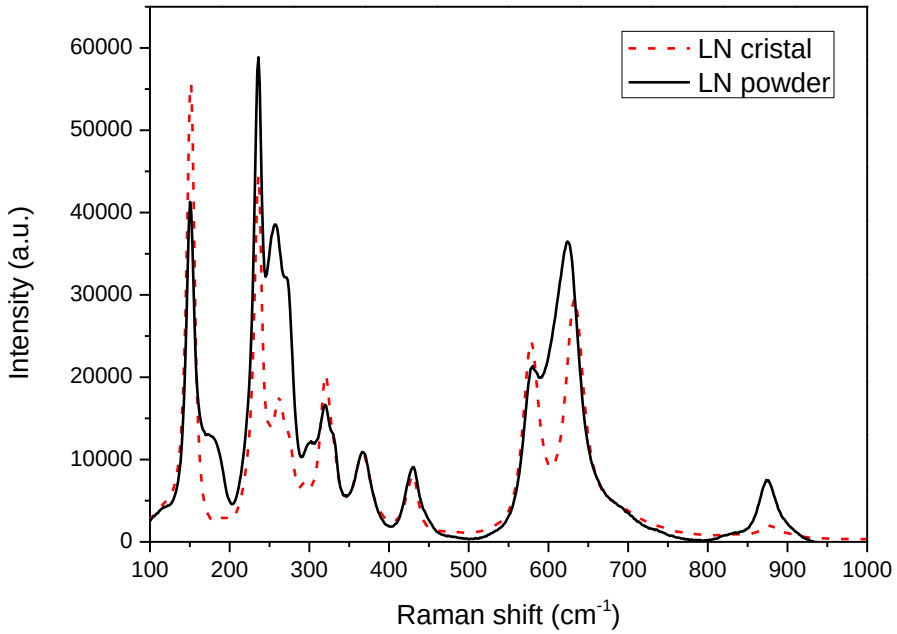

Figure II. 24*– Non-polarized Raman spectrum of congruent LN crystal and powder. The difference of the intensities of the spectra of LN powder and LN crystal can be explained by the "non-polarization" conditions of the set up. To obtain the non-polarized case the circular polarization is applied as the laser has some polarization itself. But the circular polarization of the spectrometer is not ideal, as it has ellipsoid form.*

Spectra are very similar and provide the same information. However we observe differences between spectra like the intensities of some modes and, small shifts of certain lines (near 200cm^{-1}, 300cm^{-1} and 650cm^{-1}). . In the case of powder there is no privileged direction in a contrast for the crystal which has an anisotropy so has different properties in different directions. All information (present modes) recorded by the Raman spectra on the crystal is contained in the spectrum recorded on the powder. So the spectra representing the sum of all directions and the one representing the sum of all polarizations are identical.

II.V – Asymmetry of the Raman lines and leakages

As mentioned above the Raman intensity is proportional to the Bose-Einstein population factor, this factor affects the low-frequency signal especially for the high temperature, and this can cause asymmetry of some Raman lines and therefore can lead to misinterpretation of the spectra.

Figure II.25 shows the lowest frequency E[TO_1] Raman spectrum recorded at different temperatures. This peak displays a stronger asymmetry with the increase in temperature. It is demonstrated below that this feature is mainly due to the Bose–Einstein thermal factor and its large variation with wave vector ω at high temperature.

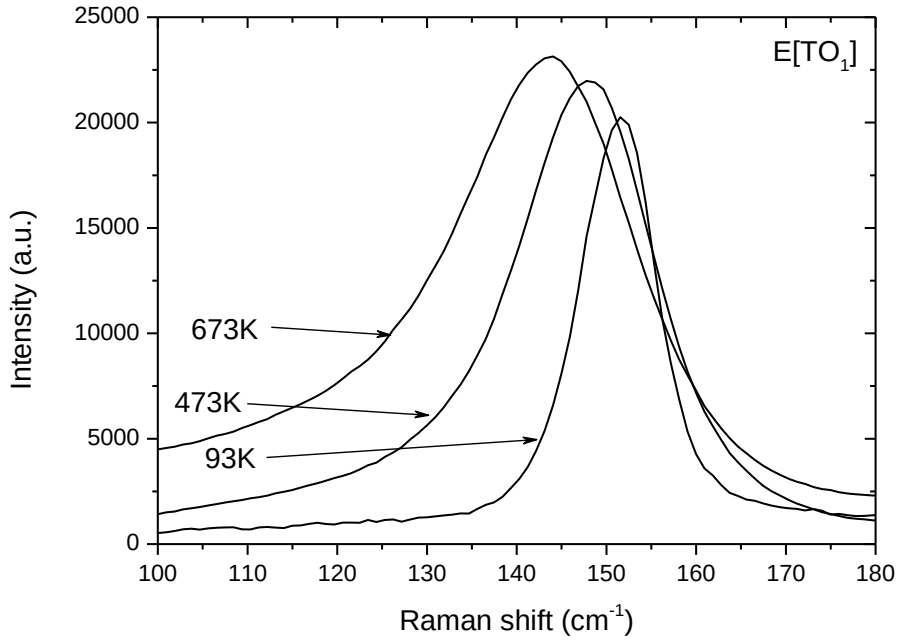

Figure II. 25– *Lowest-frequency E[TO_1] Raman spectra recorded at different temperatures*

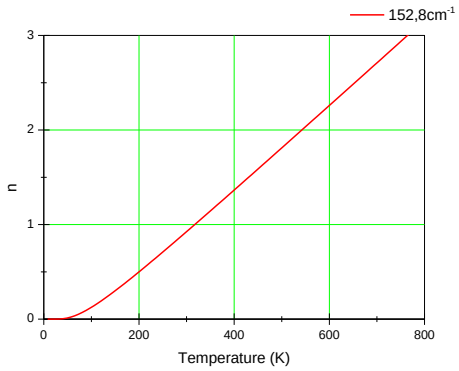

(a)

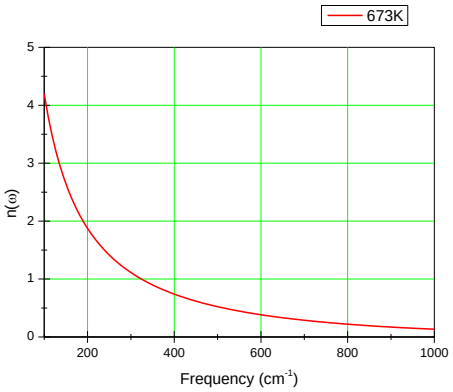

(b)

Figure II. 26 *- (a) temperature dependence of Bose-Einstein population factor for* $\boldsymbol{\omega}(E[TO_1])$ *at room temperature, (b) frequency dependence of Bose-Einstein population factor at 673K*

It is shown indeed in fig. II.27 that the asymmetry is strongly reduced after dividing the Raman intensity by the population factor $n(\omega) + 1$associated with first-order Stokes scattering. It can be noted that this effect is particularly large for low-frequency phonon lines (Fig. II.26).

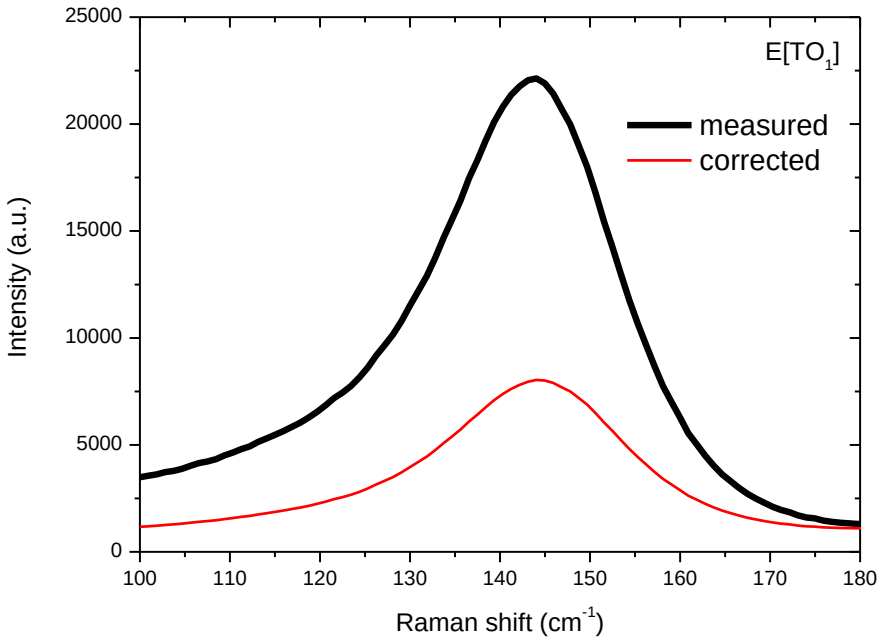

Figure II. 27*- Lowest frequency E[TO1] Raman spectrum at 673K. This spectrum is then divided by the Bose-Einstein population factor*

In figures II.28 and II.29 the measured and corrected spectra by the population factor are presented for the configuration $Y(ZZ)\bar{Y}$ *and* $Y(ZX)\,\bar{Y}$ respectively. The correction influence is much stronger for low frequency ranges.

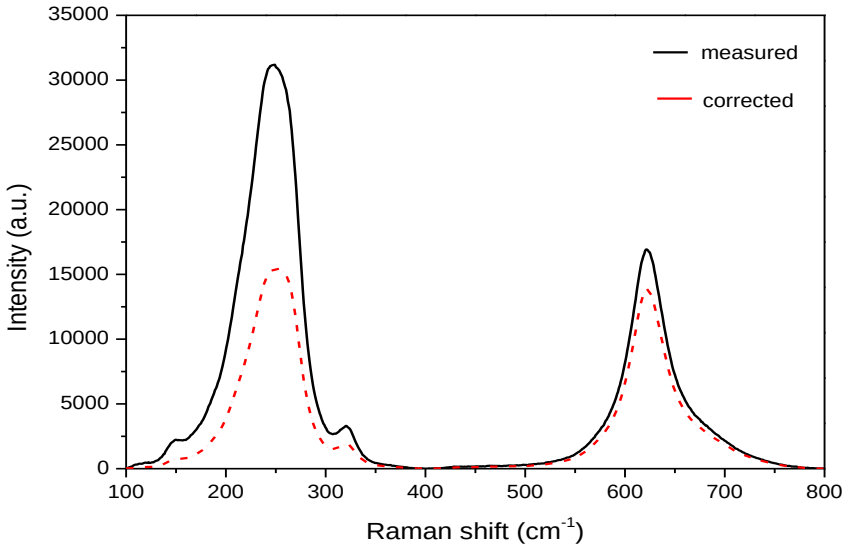

Figure II. 28- *Raman spectrum measured at 523K and after correction with the Bose-Einstein thermal factor. Configuration* $Y(ZZ)\bar{Y}$

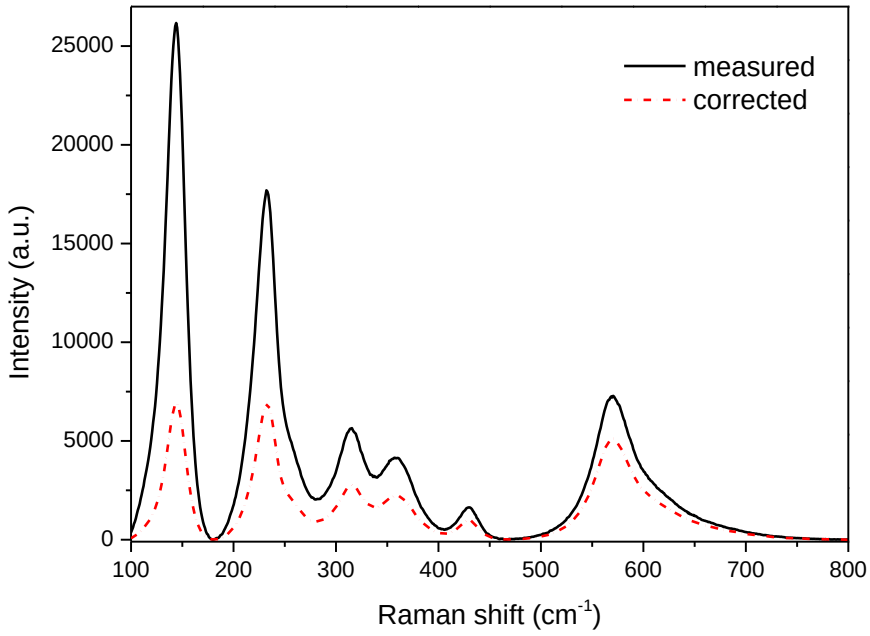

Figure II. 29- *Raman spectrum measured at 673K and after correction with the Bose-Einstein thermal factor. Configuration* $Y(ZX)\,\bar{Y}$

Other effects have to be invoked to explain the possible asymmetry of high-frequency peaks. Thus a leakage of lines with another symmetry but with frequency close to the frequency of the Raman line under consideration can also lead to asymmetric lines. The leakage arises from any, even small, misorientations of the sample and/or the polarizers thus causing the detection of lines which are in principle unexpected according to a peculiar configuration and Raman selection rules. This effect of leakage is illustrated in Fig. II.30. The spectrum (ZZ) displays in the low frequency side of the expected and intense $A_1[TO_4]$ peak, a small shoulder arising from the other symmetry E. On heating the shift-down of both peaks and their broadening give rise to a sole but wide and asymmetric band at higher temperatures.

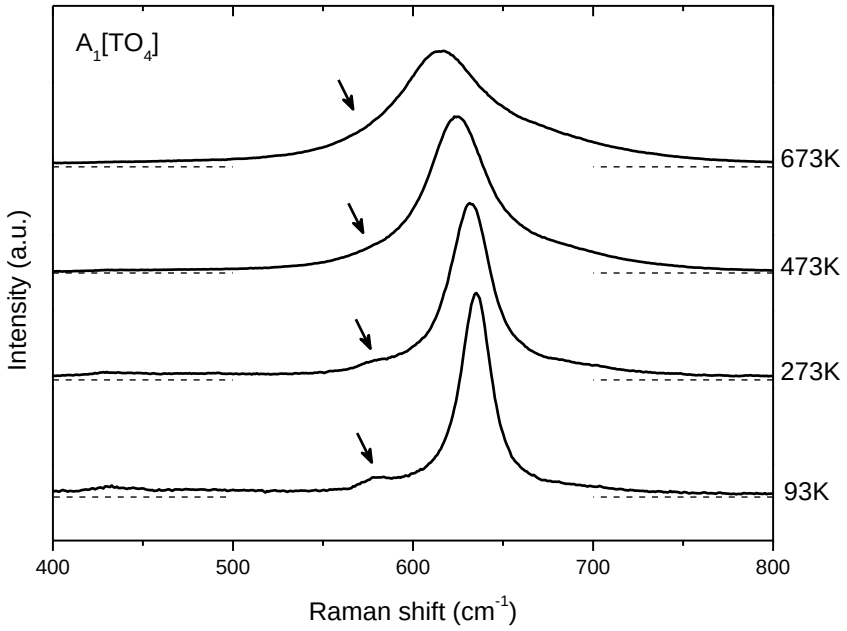

Figure II. 30– *Raman spectra around the A1[TO4] line. The arrows indicate the position of the E[TO8] showing a leakage of E[TO] spectrum into the A1[TO] spectrum. A misorientation of 7° can cause this leakage of 13%*

The leakages can be present as well as due to the polarizer and the analyzer in the spectrometer according to their adaptation to certain wavelength range. In spectrometer that was used the polarizer is adapted to range 500nm-700nm. So performing the measurements for other wavelengths (632.8nm and 785nm) additional polarizers were fixed in order to eliminate the leakages due to the polarizers. Two horizontal (H) polarizers were added in front of the laser, and the vertical (V) one was fixed after the analyzer. It has to be noted that

the V one was aligned perpendicular to H till the extinction was found. In the figure II.31 the spectra recorded without and with the additional polarizers are illustrated. It can be noted that the leakage of A_1[TO] modes is detected in the first spectra.

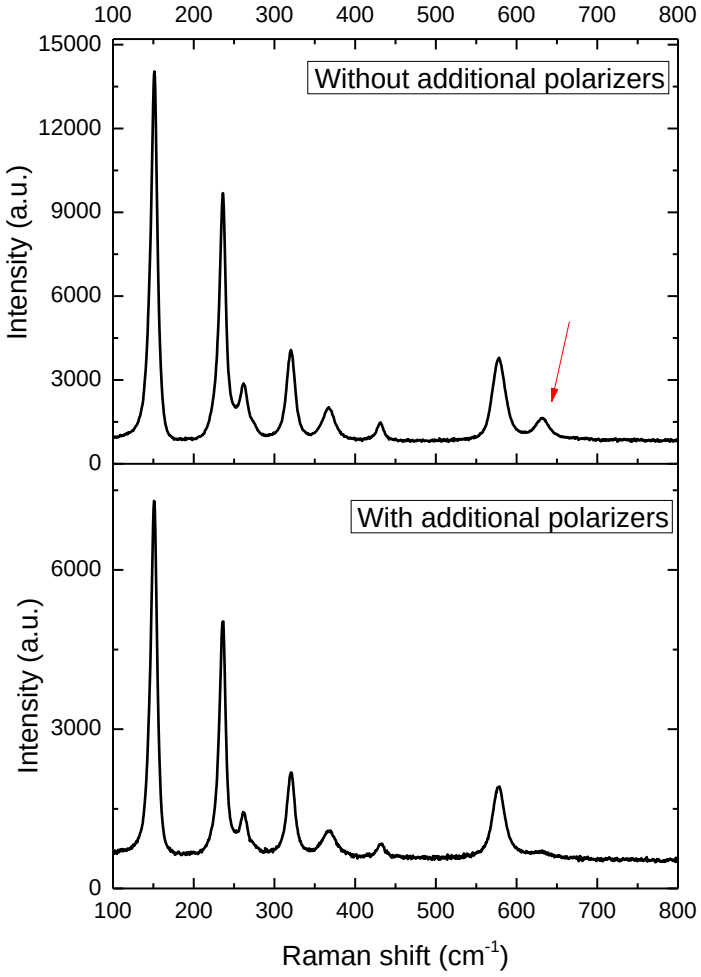

***Figure II. 31**–Raman spectra of Y(XZ) $\bar{Y}$ configuration without and with additional polarizers*

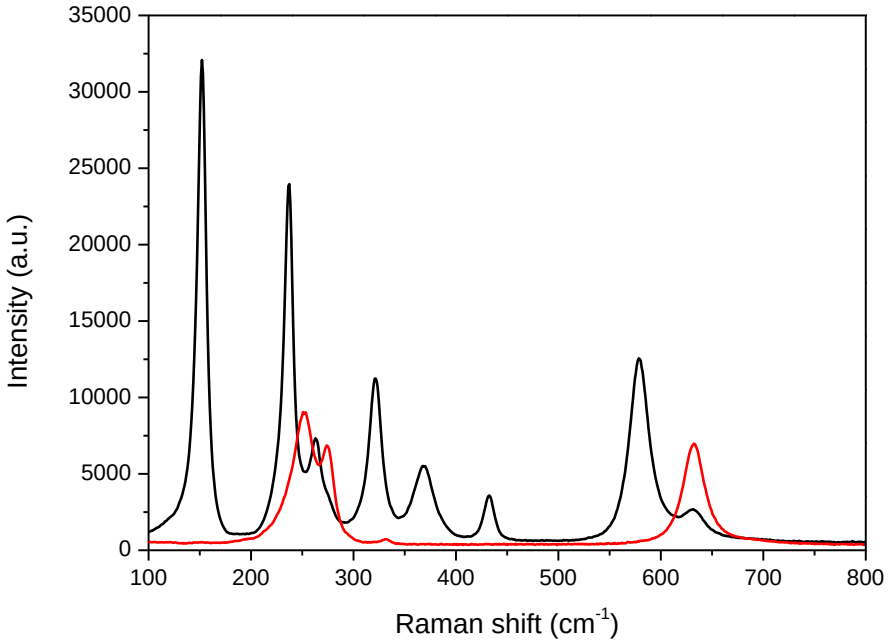

Figure II. 32– *Raman spectra for the configurations Y(ZX)* $\bar{\boldsymbol{Y}}$ *(black) and Y(ZZ)* $\bar{\boldsymbol{Y}}$ *(red) of a congruent LN crystal*

The position of A_1[TO] modes in the spectra of E[TO] modes is illustrated in the figure II.32. The intensity of A_1[TO] lines are less than for E[TO] line, which is in a contrary with the difference mentioned above in the chapter. This is explained by the additional polarizers which decrease the beam intensity.

Additional measurements were performed in order to have a clear idea about the leakages and additional lines. The crossed polarization was used in order to have a clear response of the polarizer (fig.II.33).

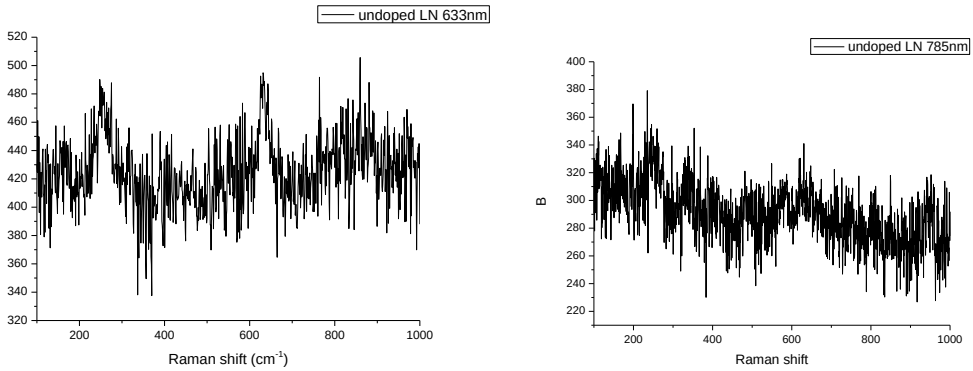

Figure II. 33 *–Raman spectra with crossed polarizers*

One can notice that the obtained spectra can be considered as a noise as they have a quite small intensity comparing the non-crossed Raman spectra.

II.VI Conclusion

In this chapter the selection rules of Raman lines were demonstrated for backward, forward and scattering at 90^{o}. Raman spectra of all configurations of backscattering were plotted and fitted in order to determine the frequency of all Raman existing modes. These results are the references for all feature studies. The influence of the temperature on Raman lines was studied, and it was shown that the asymmetry of lines with low frequency is strongly reduced after dividing the Raman intensity on the Bose-Einstein population factor. The presence of leakages was detected for some configurations and different origins were mentioned.

II.VII – References

[1] A. Smekal, Naturwissenschaften 11, 873 (1923)

[2] C. V. Raman and K. S. Krishnan, "*A new type of secondary radiation*", Nature 121, 501 (1928)

[3] I.R. Lewis and H.G.M. Edwards, Edts, "*Handbook of Raman spectroscopy"* Marcel Dekker, Inc – New York (2001)

[4] E.Schuller, R. Claus, H.J. Falge and G. Borstel, "*Comparative FTR-and Raman spectroscopic studies of fundamental mode frequencies in $LiNbO_3$ and the present limit of oblique phonon dispersion analysis*" Z. Naturforsch. 32, 47 (1977)

[5] D. A. Long, "*Raman spectroscopy"* McGraw-Hill, New York (1977)

[6] G.P. Srivastava, "*The physics of phonons*" ISBN: 0-85274-153-7, Adam Hilger – IOP Publishing Ltd (1990)

[7] R. Poilblanc et F. Crasnier, "*Spectroscopies Infrarouge et Raman*" EDP Sciences (2006)

[8] R. Loudon, "*The Raman effect in crystals*" Adv. Phys. 13, 423 (1964)

[9] S.C. Abrahams, J.M. Reddy, J.L. Bernstein „*Ferroelectric lithium niobate 3. Single crystal X-Ray diffraction study at 24C"* J.Phys. Chem. Solids 27, 997 (1966)

[10] Y. Shiozaki, T. Mitsui "*Powder neutron diffraction study of LiNbO3*", J. Phys. Chem. Solids 24, 1057 (1963)

[11] R. Claus, G. Borstel, E. Wiesendanger, L. Steffan, *„Assignments of Optical Phonon Modes ln LiINbO3"* Z. Naturforsh. 27 a, 1187 (1972)

[12] A.S. Barker Jr., R.Loudon "*Dielectric Properties and Optical Phonons in LiNbO3*", Phys. Rev. 158, 433 (1967)

[13] X. Yang, G. Lan, B. Li, H. Wang "Raman Spectra and Directional Dispersion in LiNbO3 and LiTaO3" Phys. Stat. Sol. B 141, 287 (1987)

[14] R. F. Schaufele, M. J. Weber *"Raman scattering by Lithium Niobate*" Phys. Rev. 152, 705 (1966)

[15] V. Cacius, A.V. Postnikov and G. Borstel, "*Ab initio structure and zone-center phonons in LiNbO3*" Phys. Rev. B 61, 8806 (2000)

[16] A. Ridah, P. Bourson, M.D. Fontana, and G. Malovichko, "*The composition dependence of the Raman spectrum and new assignment of the phonons in $LiNbO_3$*" J. Phys.: Condens. Matter **9**, 9687 (1997)

[17] A.V. Postnikov, V. Caviuc and G. Borstel, "*Structure optimization and frozen phonons in $LiNbO_3$*" J. Phys. Chem. Solids 61, 295 (2000)

[18] I.P. Kaminow and W.D. Johnston, Jr, "*Quantitative determination of the electro-optic effect in $LiNbO_3$ and $LiTaO_3$*" Phys. Rev. 160, 519 (1967)

CHAPTER III

Effect of Zr doping on the structure of Lithium Niobate crystals: Site spectroscopy and Chemometrics

III.I – Introduction

At present, a strong limitation to the applications of LN crystals comes from the fact that, under illumination with visible or near-infrared light, there are semi-permanent changes in the index of refraction of the crystal, due to the photorefractive effect (or "optical damage"), causing beam distortion and dramatically decreasing the device efficiency. This drawbacks and limitation exist unless some strategy to reduce the photorefractive effect is implemented [1]. The resistance to optical damage can be increased considerably by changing the LN crystal composition from congruent to stoichiometric [2,3] and/or by adding to LN an appropriate non-photorefractive dopant. Among the many dopants that have been tested, the most utilized is, at present, MgO that is known to be effective in molar concentrations above 5 mol%. The main problem with this is the very huge difficulty to grow large homogeneous MgO doped LN crystals. Recently, different tetravalent impurity ions (Hf^{4+}, Zr^{4+}, Sn^{4+}) were proposed as new non-photorefractive impurity ions [4,5]. Complex investigations of Hf as well as Zr doped congruent composition LN crystals including photorefractive, non-linear optical, compositional, electro-optical [6-10] properties have been shown that tetravalent impurity ions with a threshold concentration of around 2-3mol% can be considered as good candidates for reduction of the photorefractive effect in LN crystals with preserving of its main characteristics. However, it is very useful to know the environment of the dopants and the various alternative mechanisms to understand the microscopic mechanisms of induced effects in the crystals doped ions. In this work the Zr doped LN crystals are investigated in order to have a clear idea of the threshold concentration of the impurity ion required for the reduction of the photorefractive effect as well as sites occupied by different concentration Zr ions in the structure of LN. Raman scattering was used to characterize Zr doped LN crystal with two complementary ways for exploiting spectra: deconvolution and chemometrics. Chemometrics is a statistical method which is not so often used in the frame of solid materials. It is generally useful to compare large databases or/and small variations.

III.II – Site spectroscopy

III.II.1 – Site spectroscopy probed by Raman spectroscopy

Congruent composition LN crystals doped with various concentration of Zr were grown by the Czochralski method in a platinum crucible of dimensions 50x50x3mm3 using a set-up with a radio frequency [11] heating. The crystals were grown along the crystallographic c axis with a rotation rate of the seed of 20 rotations per minute and pulling rate 1mm per hour. The ferroelectric critical temperature of the congruent composition crystal is about 1142 °C, just about 110°C below the melting point of the congruent composition LN (1253 °C). To obtain single-domain crystals directly during the growth process, we applied an electric field (a electrical current of 12 A/M^2) to the crystal-melt system [1]. Without the application of an external electric field, the crystals grow in the paraelectric phase. Multidomains then appear as the sample is cooled below the Curie temperature, and an additional post-growth annealing procedure is required. The application of an electric field to the crystal-melt system during crystal growth leads to a homogeneous distribution of impurity ions within the main constituents that form the crystal [1]. The starting materials used for sintering the lithium niobate charges of congruent composition were high purity Nb_2O_5 and Li_2CO_3 compounds from Johnson-Mattey and Merck. The amount of impurity included in each initial charge of LN after the components were thoroughly mixed was ZrO_2 with concentration equals to 0.625, 0.75, 0.875,1.00, 1.25, 1.50, 2.00 and 2.50 mol%, respectively. The grown boules of crystals with diameters of about 20mm and a length of about 30mm were oriented by the method of Laue. After, samples were cut and polished to obtain rectangular samples with optical grade facets, perpendicular to the principal axis. The sizes of the samples were about 10×4×6.5 mm3 along the x, y and z axes, respectively.

As it was mentioned in introduction, Raman spectroscopy is utilized for investigation of the sites of Zr in LN. Measurements were performed at room (300K) and at low (93K) temperature in order to have a better resolution (the lines are thinner and more separated). Spectra were recorded for 2 configurations: $Y(ZZ)\overline{Y}$ (A_1[TO] modes) and $Y(ZX)\overline{Y}$ (E[TO] modes).

III.II.2 – Experimental part

Here are presented data recorded in configurations for different concentrations of Zr in LN (figures III.1 and III.2). There is no visible change in the spectra between the samples except the undoped one which have some leakages in spectra for both configurations. This may be due to some misorientations of the sample which are more visible at low temperatures due to the better resolution.

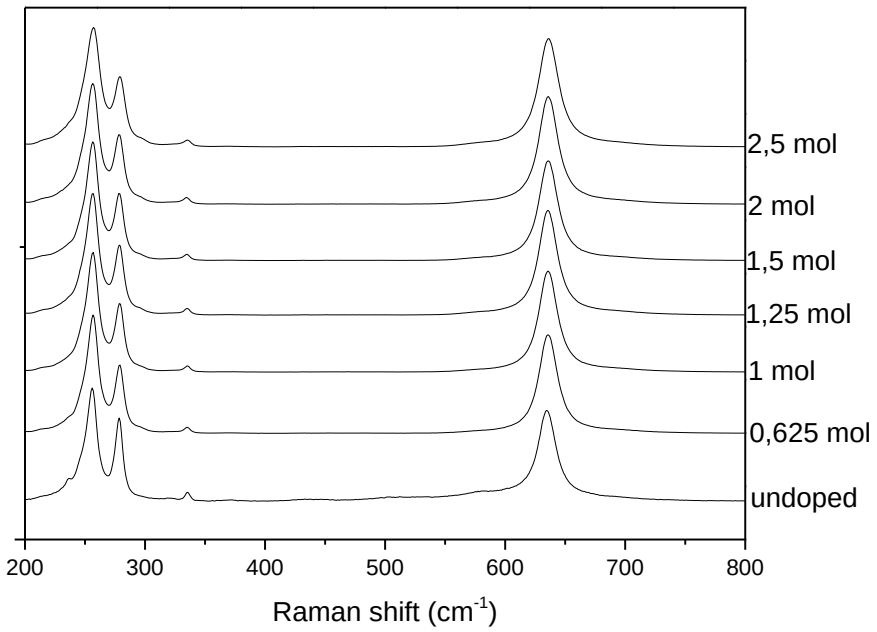

Figure III. 1 *– A_1[TO]Raman spectra in Y(ZZ)$\bar{Y}$ configuration for different concentrations of Zr ions in LN obtained at 93K*

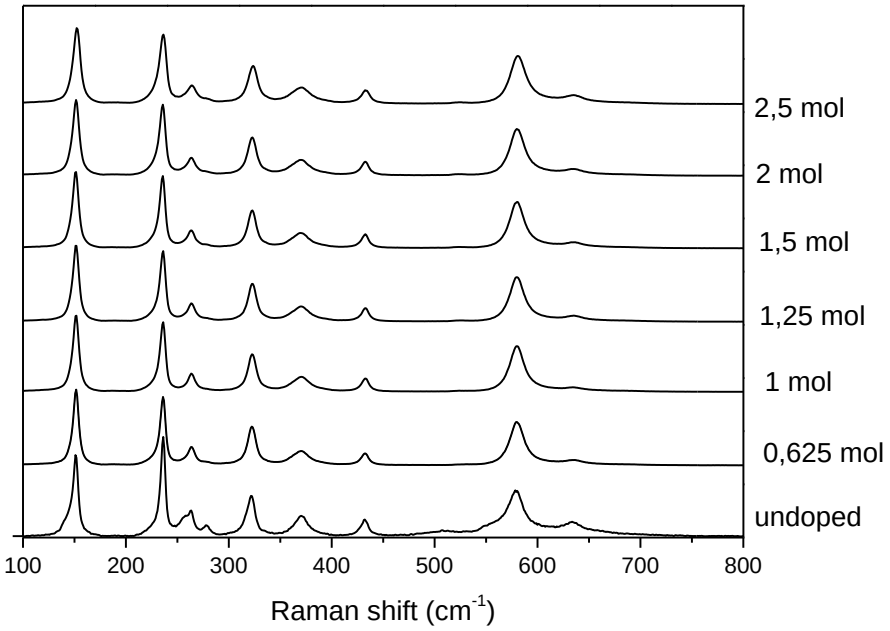

Figure III. 2– *E[TO] Raman spectra in Y(ZX)$\bar{Y}$ configuration for different concentrations of Zr ions in LN obtained at 93K*

As modes $A_1[TO_1]$ and $A_1[TO_2]$ are associated to the sites B and A respectively the corresponding lines, are plotted in the figure III.3 for different Zr content, in order to investigate the Zr site occupation.

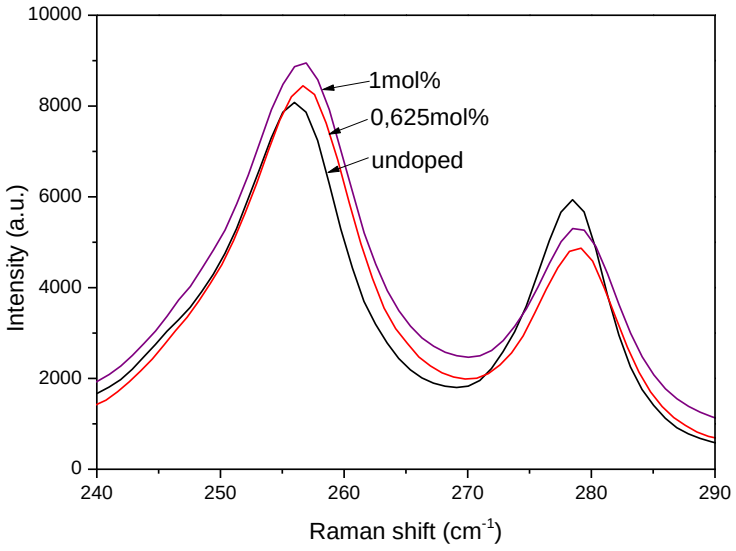

(a)

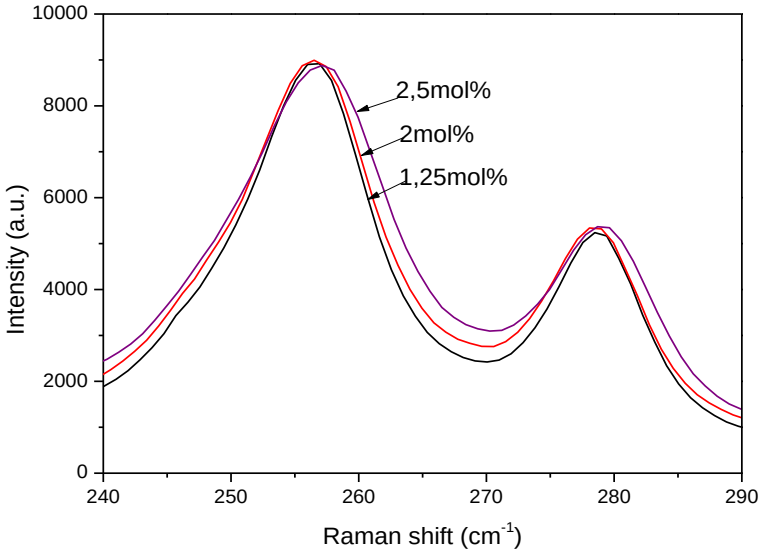

(*b*)

Figure III. 3 *– Modes $A_1[TO_1]$ and $A_1[TO_2]$obtained at 93K for different concentrations of Zr (a) undoped, 0.625mol%, 1mol% (b) 1.25mol%, 2mol%, 2.5mol%*

One observes that there is a change in the positions of both lines between the undoped and the 0.625mol% ZrO_2 doped LN (figure III.3 (a)). For higher concentration positions are nearly the same, and only for 2.5mol% ZrO_2 doped LN, a significant change is detected. In addition we observe that the linewidths of both lines increase with increasing the concentration of Zr. Before starting the fitting procedure there is no necessity here to perform the Bose-Einstein factor correction. Indeed, all measurements were recorded at the same temperature (93K), and the frequency range for each peak is nearly the same and the shift is very small between different samples.

The intensity, position and the linewidth are the parameters obtained for all modes by the fitting procedure.

III.II.3 – Results

Fitting procedure provides the phonon frequency and damping dependences on the concentration of Zr ions in LN. Here are the results for A_1[TO] modes obtained in the Y(ZZ)$\bar{Y}$configuration:

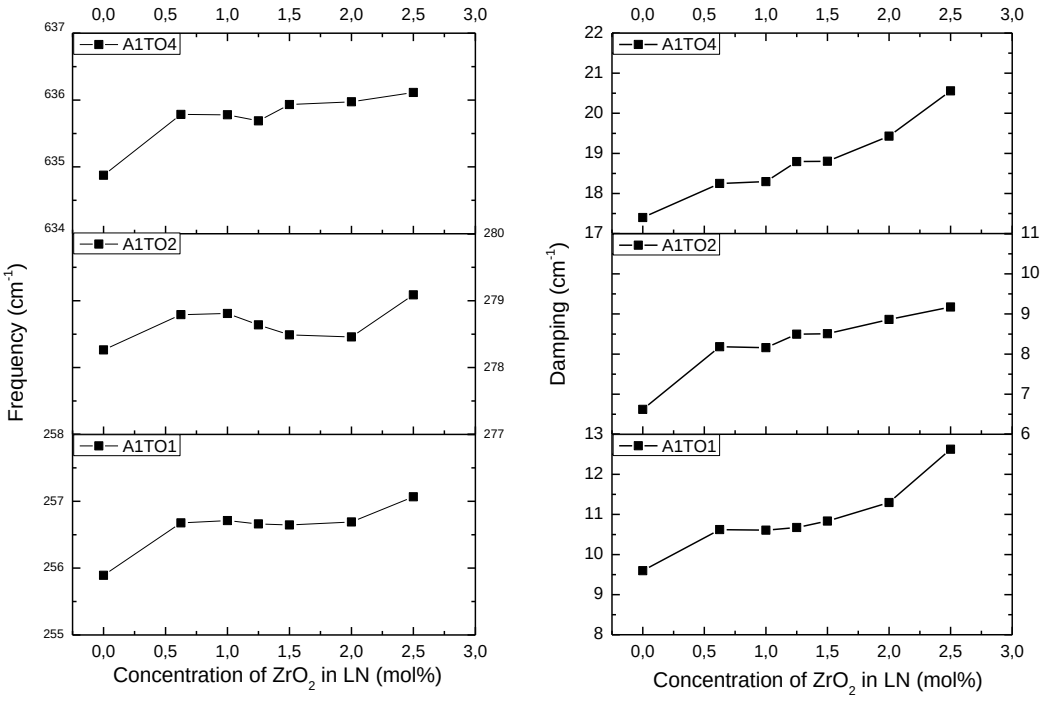

Figure III. 4– *Dependences of phonon frequency and phonon damping as a function of concentration of Zr ions in LN*

One can see that the phonon frequency increases with doping the LN with ZrO_2 comparing to the undoped one (figure III.4). For the mode $A_1[TO_1]$ the phonon frequency is nearly the same for all concentration of ZrO_2 below 2mol%, and then is larger for higher concentration. The mode $A_1[TO_2]$ shows a similar behavior versus Zr concentration. For the mode $A_1[TO_4]$ the frequency is nearly unchanged with the concentration of Zr in LN.The phonon damping of all modes increases with doping LN with Zr and with increasing monotonously with doping.

Here are the results for E[TO] modes obtained in Y(ZX)Y configuration:

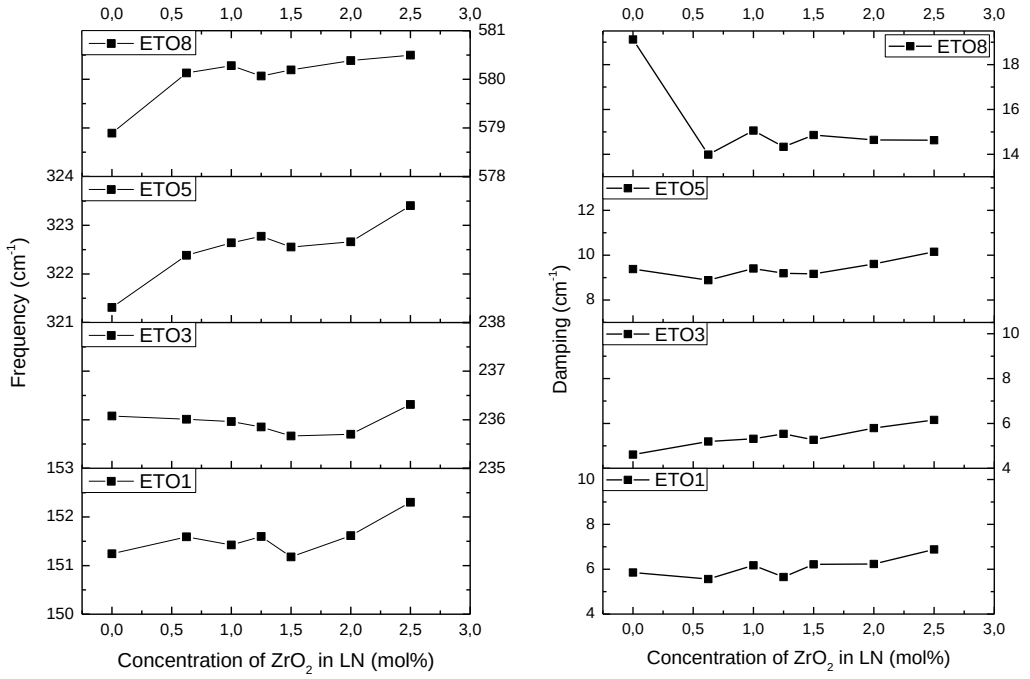

Figure III. 5*– Dependences of phonon frequency and phonon damping as a function of concentration of Zr ions in* ***LN***

The frequency of the mode E[TO_1] is nearly the same varying between 151cm^{-1} and 151.5cm^{-1} only for the concentrations below 2 mol% of Zr, and increases at 2.5mol% concentration reaching the value of 152.5cm^{-1}. The frequency of the mode E[TO_3] is nearly the same for all concentrations of Zr, varying between the values of 235.5cm^{-1} and 236.5cm^{-1}. For the mode E[TO_5] the frequency increases between undoped sample and 0.625mol% ZrO_2 doped sample (nearly 1cm^{-1} of increase) and then is constant between 0.625mol% and 2mol% and at last increases again for the concentration of 2.5mol% of ZrO_2 (reaching the value of 323.5cm^{-1}). For the mode E[TO_8] the increase of frequency concerns only the change between the undoped and doped samples (nearly 1.2cm^{-1} of increase). The phonon damping has nearly the same value for all modes independently of the concentration except the mode E[TO_5] where a large decrease of about 6cm^{-1} is detected between the undoped sample and 0.625mol% ZrO_2 doped sample.

The frequency change is very small for all modes under study so that is seems difficult to derive some information on the Zr site interpretation from these results. As a consequence we use an additional method: chemometrics.

III.III – Chemometrics and PCA

In a first view chemometrics means performing calculations on measurements of chemical data. More recently, the common usage of the word refers to using linear algebra calculation methods, to make either quantitative or qualitative measurements of chemical data, primarily spectra.

The science of chemometrics gives many different ways to solve the calibration problem for analysis of spectral data. Some are very simple to understand, while others require a strong background in linear algebra. The key to understanding chemometrics is in not necessarily understanding the mathematics of all the different methods; it is to know which model to use for a given analytical problem and properly applying it.

Principal Component Analysis (PCA) is a projection method that provides a possibility to visualize all the information contained in a data table. In a simple way by decreasing the number of variables PCA helps to find out which samples are similar and which are different according to one or more principal component (PC), which variables contribute most to this difference, and whether those variables contribute in the same way or independently from each other. It also enables to detect sample patterns, like any particular grouping with similar variation. Principal component analysis PCA can be applied to obtain the basic spectral features describing complete series of spectra. These basic spectral features are called the loadings or principal components PCs of the data set.

III.III.1 – PCA performed on Raman spectra

Performing a PCA on spectra we obtain the projection values of sample on each PC. These scores provide a possibility to have an idea of the relative change between different samples. Loadings represent the new base, which are representative to the variation on each spectra

$$Spectrum = \langle S \rangle + s_1 PC_1 + s_2 PC_2 + \cdots + \varepsilon$$

Where S is the average spectrum, s_i are scores, PC_i are loading, ε are residual values. That provides a possibility to see the influence of each component on the spectra (it has to be mentioned that the changings are compared to the average spectra).

In spectroscopy, PCA calculations are mostly used to follow species concentration (especially low concentration) through intensity variation. Interpretation of a frequency variation of one mode could be difficult as the resultant PCA loading is similar to a relative intensity variation of two peaks, with close frequencies. To illustrate this, two different spectroscopic cases were numerically generated: the relative intensity variations of two Gaussian functions (centered at 400cm^{-1} and 419cm^{-1}) as shown in fig III. 6; the frequency shift of one Gaussian function from 400cm^{-1} to 419cm^{-1} as shown in fig III.7

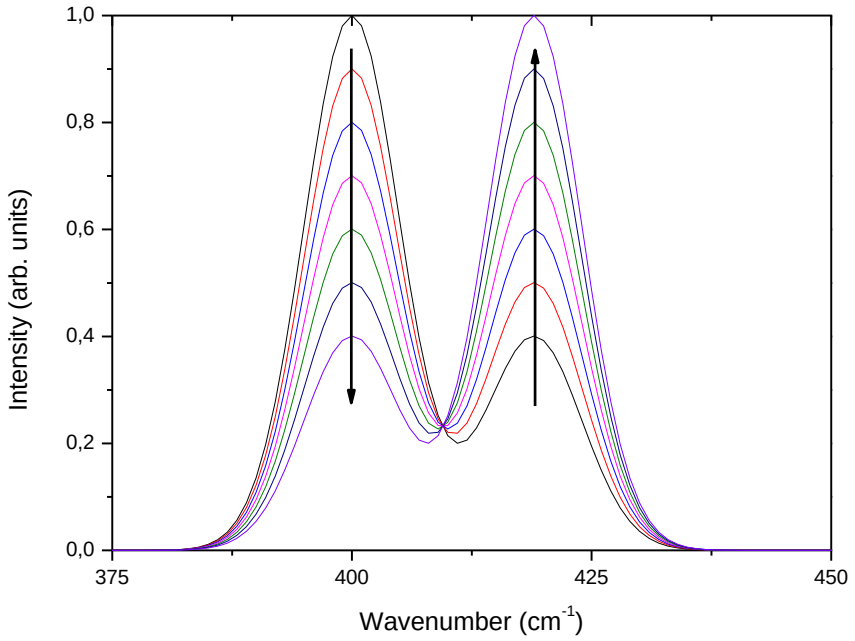

Figure III. 6*- Two Gaussian functions centered at 400cm^{-1} and 419cm^{-1}*

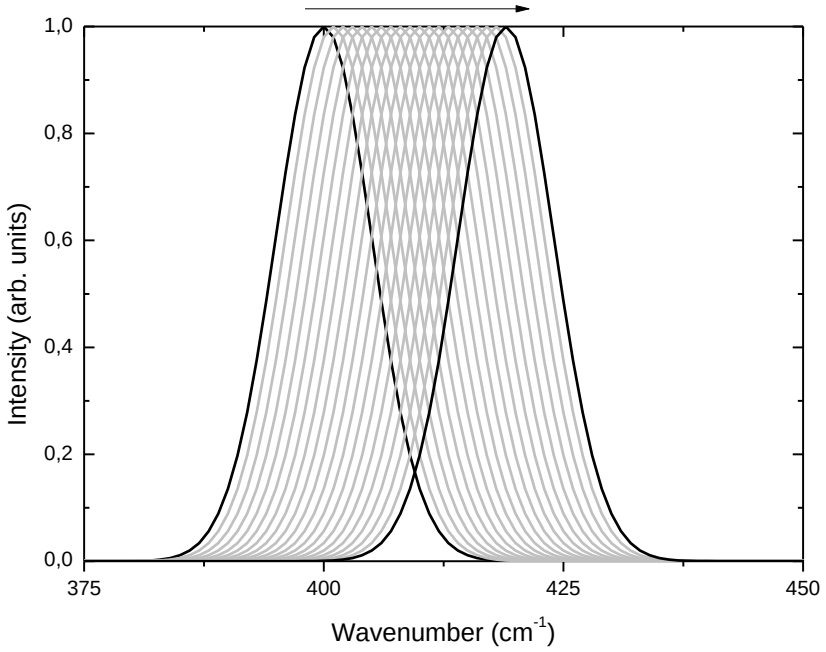

Figure III. 7 *-Frequency shift of a Gaussian function from 400cm^{-1} to 419cm^{-1}*

The first loading (PC1) of each case is shown in fig III.8. Their shapes are similar.

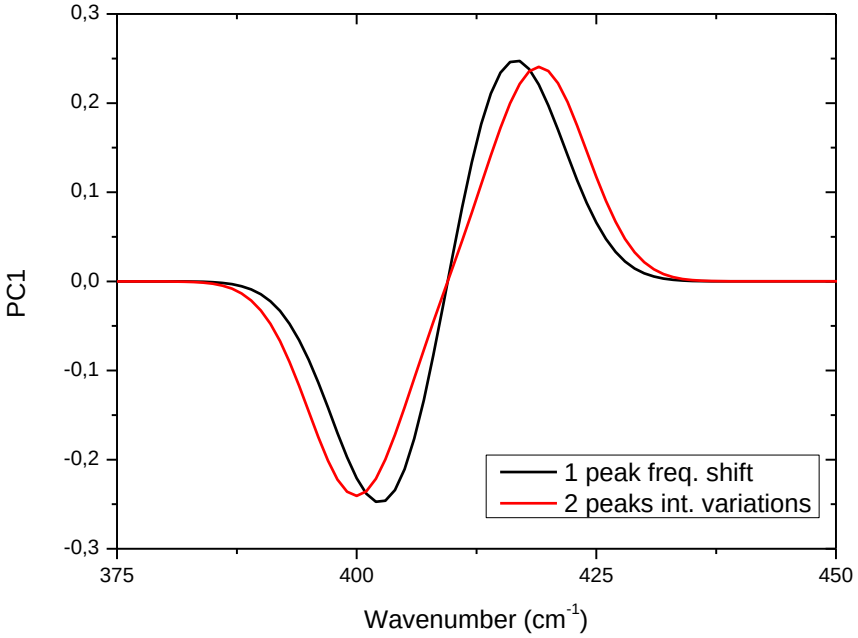

Figure III. 8*– Loadings of PC-1 for one Gaussian peak shift and two Gaussian peaks variations*

This means that performing the PCA on the spectra we can obtain similar results for completely different spectroscopic cases. So a special attention has to be given to PCA results interpretation. It can be noticed that the loadings of PC1 for the case of one Gaussian peak shift is the 1st derivative of the peak [12, 13], in addition it has to be mentioned that the 2nd derivative represents the line width change of the peak. In further investigations in this chapter these two facts are utilized in order to interpret the obtained results.

In our investigations the principal component analysis (PCA) was performed using the *Unscrambler10.3* software. The analysis was performed after performing a standard normal variate (SNV) pretreatment on the spectra utilizing the same software. The transformation is applied to each spectrum individually by subtracting the mean spectrum and scaling with the spectrum standard deviation. This means that it normalizes the intensity and corrects the baseline of all spectra. The PCA was done for the spectra of both configurations Y(ZZ)$\bar{Y}$ and Y(ZX)$\bar{Y}$).

- ***Y(ZX)Y: Scores and loadings***

PCA was performed on the Raman spectra obtained at low temperature (-180^{o}C) for the Y(ZX)Y configuration, in which case the modes E[TO] are presented. Before performing the analysis the spectra were cut taking into account only the range which contains E[TO_1] mode (100cm^{-1} – 200cm^{-1}). The scores of the PCA analysis are presented in figure III.9. The scores for each sample and component are obtained. Projecting on the axis PC-1 the values of scores of all samples one can see that the values differ only for samples 0, 2, 1 and 1.25 mol% ZrO_2 concentrations. It has to be mentioned that negative or positive sign of the PC is meaningless for interpretation

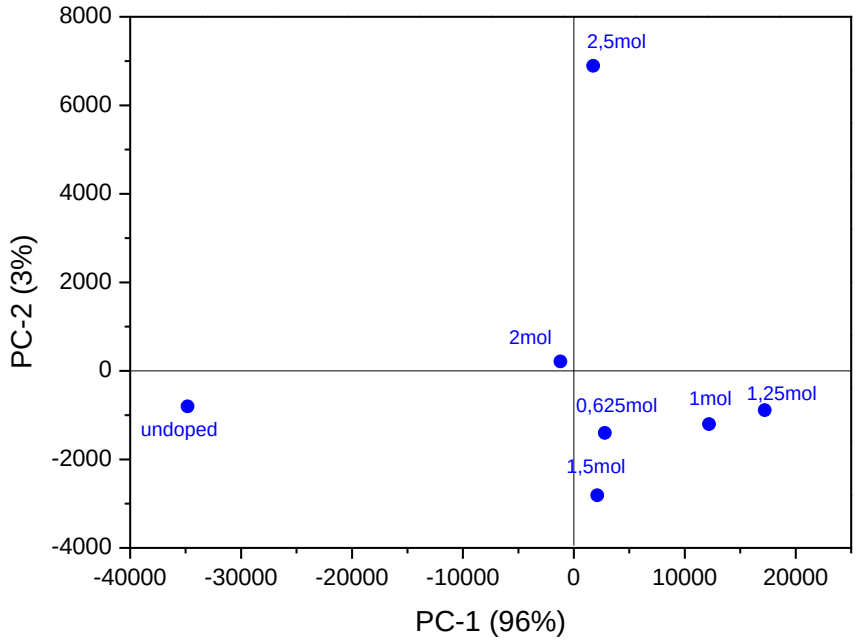

***Figure III. 9**- Scores of spectra (range of 100cm^{-1} – 200^{-1}) of all samples of Y(ZX)Y configuration obtained at low temperature (-180^{o}C)*

Projecting the scores on the PC-2 axis one can notice that all the samples except the 2.5mol% Zr doped LN sample are nearly the same. PC-1 explains 96% of variance between spectra and the PC-2 shows the 3% of variance of the spectra, this means that with two components the variance between all spectra is explained in 99%. Taking into account the loadings of two components one can mention that the variations of components are present only in the range of Raman line (E[TO_1]), which means that the component corresponds to the changes of Raman spectra.

In Figure III.10 the loadings of the components are presented. The first spectrum (lowest part) is the one of 2mol% ZrO_2 concentration as is similar to the average spectrum (nearest to 0 value of PC according to scores).

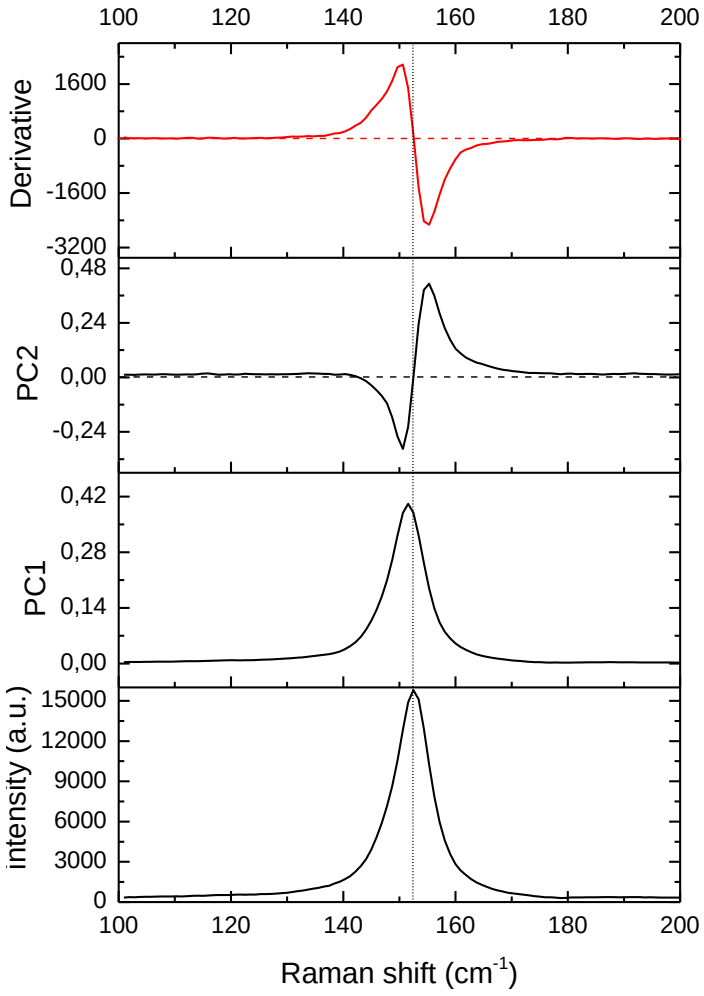

Figure III. 10 *- Loadings of PC1 and PC2 of PCA performed on the spectra (range of 100cm^{-1} – 200cm^{-1}) obtained at low temperature 93K, for the Y(ZX)Y configuration. Spectrum of 2mol% ZrO_2 and its derivative are shown for comparison*

As seen in figure III.10 the PC-1 is similar to a measured spectrum and doesn't look like a derivative. This component reflects the intensity change between spectra. In contrast the PC-2 is similar to the first derivative of the spectra (which is also shown in the figure). As it was mentioned above in this chapter, this fact means that the PC-2 represents the shift of the position of the peak between the spectra.

- ***Y(ZZ)$\bar{Y}$: Scores and loadings***

The spectra of Y(ZZ)$\bar{Y}$ configuration were used in the analysis. The spectra were cut into two parts. First part contains the modes $A_1[TO_1]$ and $A_1[TO_2]$ ($200cm^{-1}$ – $475cm^{-1}$), and the second part contains the mode $A_1[TO_4]$ ($550cm^{-1}$ – $700cm^{-1}$).

Performing the PCA on the high frequency peak (range of $550cm^{-1}$ – $700cm^{-1}$) recorded at low temperature (93K) one can obtain the scores for all samples (figure III.11).

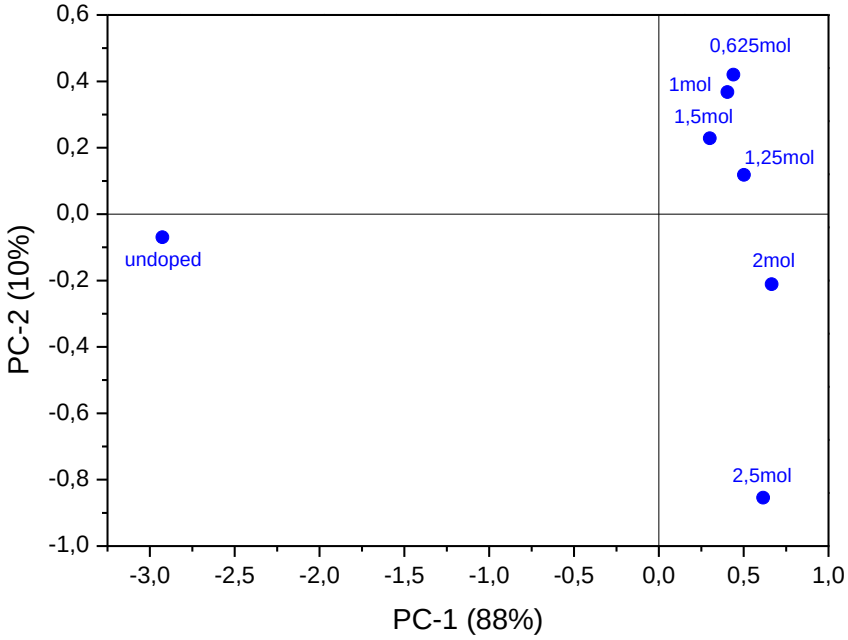

Figure III. 11- *Scores of spectra (range of $550cm^{-1}$ – $700cm^{-1}$) of all samples of Y(ZZ)$\bar{Y}$ configuration obtained at low temperature (93K)*

Projecting the scores of the samples on the axis PC-1 one can notice that all the samples except the undoped one have nearly the same value. And projecting the scores on the axis PC-2 one can see that except the undoped sample, all samples are classified according to the concentration of Zr. The PC-1 explains the 88 % of variance, and the PC-2 explains 10 %, this means that with both principal components the 98% of variance of all spectra is reported.

The loadings of this component are presented in the figure III.12. The first spectrum is the one of 2 mol% ZrO_2 doped sample. In the figure the loadings of PC-1 and PC-2 are presented and the first derivative of the spectra in order to be able to compare with loadings.

The loadings of mentioned components show variations only at the range of the Raman line, which means that the components shows the changes of Raman spectra.

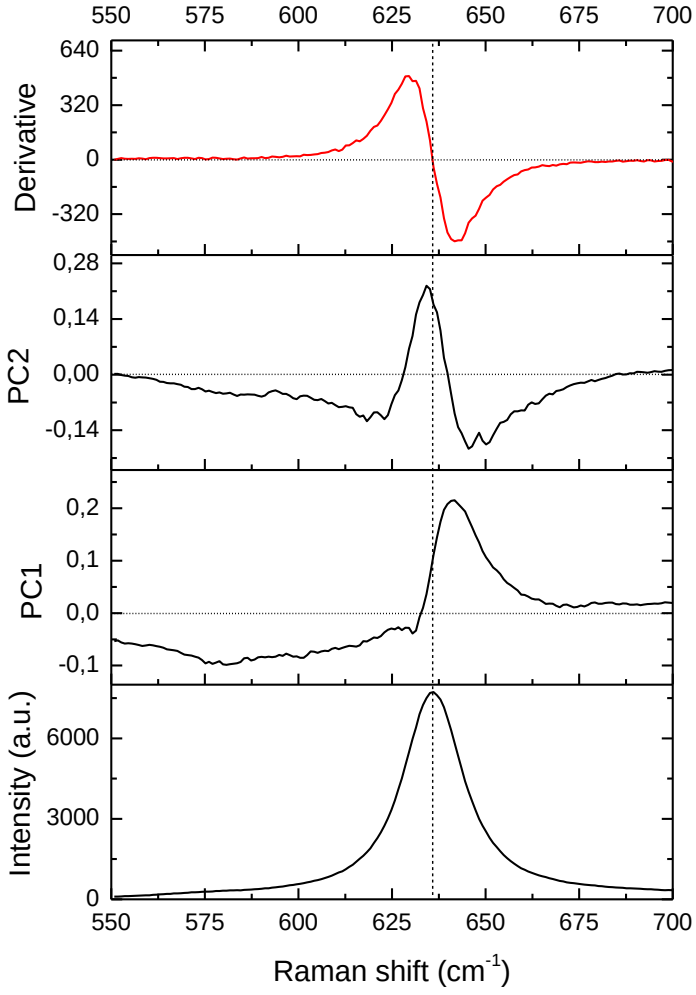

Figure III. 12*- Loadings of PC1 and PC2 of PCA performed on the spectra (range of 550cm^{-1} – 700cm^{-1})obtained at low temperature (93K), for the Y(ZZ)* $\bar{\boldsymbol{Y}}$ *configuration. Derivative of the Raman spectra*

One can see that PC-1 is quite similar to the 1st derivative with zero crossing (with opposite sign) of the $A_1[TO_4]$ mode which means that this component represents the shift of the position of the line. As it was seen in the figure IV.11 the scores PC-1 are nearly the same for all samples except the undoped one. And according to loadings of this component it can be confirmed as the shift of the position of the peak between Zr doped samples and undoped sample. The PC-2 reports the mix of 1st derivative with the 2nd derivative. As it was mentioned in the introduction of this chapter, the second derivative describes the linewidth change between samples. It can be concluded that the PC-2 reports the shift of the position

and the linewidth change between the spectra. According to scores of this component (figure III.11) the values of scores were classified according to the concentration of Zr and the undoped one has the value which is near to the value of the 2 mol% ZrO_2 doped sample.

Now we turn on results of PCA on low frequency of all measured spectra. The scores of each sample are plotted in figure III.13.

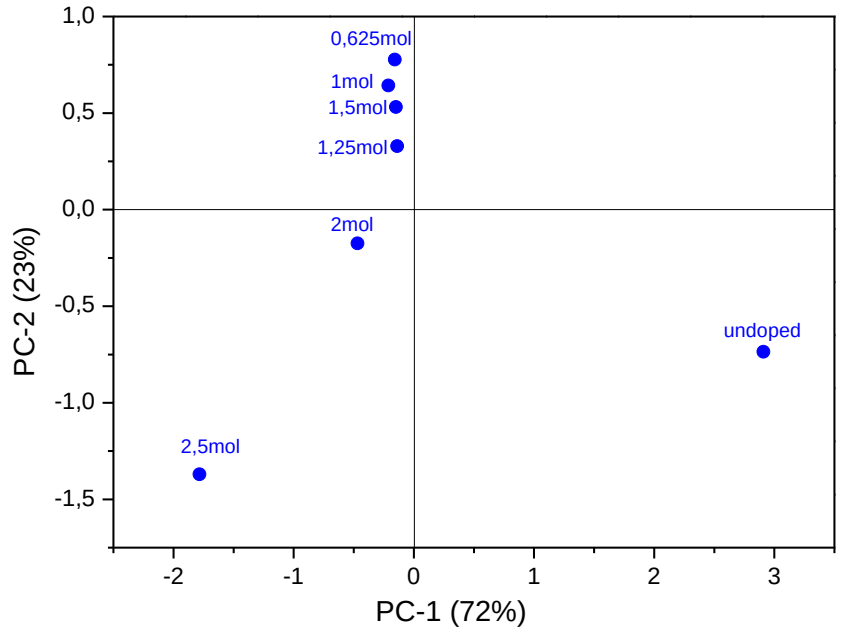

***Figure III. 13**- Scores of spectra (range of 200cm^{-1} – 475cm^{-1}) of all samples of Y(ZZ)$\overline{Y}$ configuration obtained at low temperature (93K)*

There are two axis (PC-1 and PC-2) which show different values for different samples. Each component distinguishes the samples differently. Projecting the scores of each sample on the axis PC-1 one can see that the values corresponding to 2.5mol% ZrO_2 doped LN and the value of undoped LN sample are different from each other and from the rest of samples. In a contrast the scores of the samples 0.625mol%, 1mol%, 1.25mol%, 1.5mol% and 2mol% ZrO_2 doped LN are nearly the same. Projecting the scores of all samples on the axis PC-2 it is visible that the samples are classified according to Zr concentration except the undoped sample which has the value between the 2mol% and 2.5mol% ZrO_2 doped LN. It has to be noted that the 95% of variance is explained with PC-1 and PC-2.

The loadings of the components are presented in figure III.14. The first spectrum is the 2 mol% ZrO_2 doped LN as for previous cases.

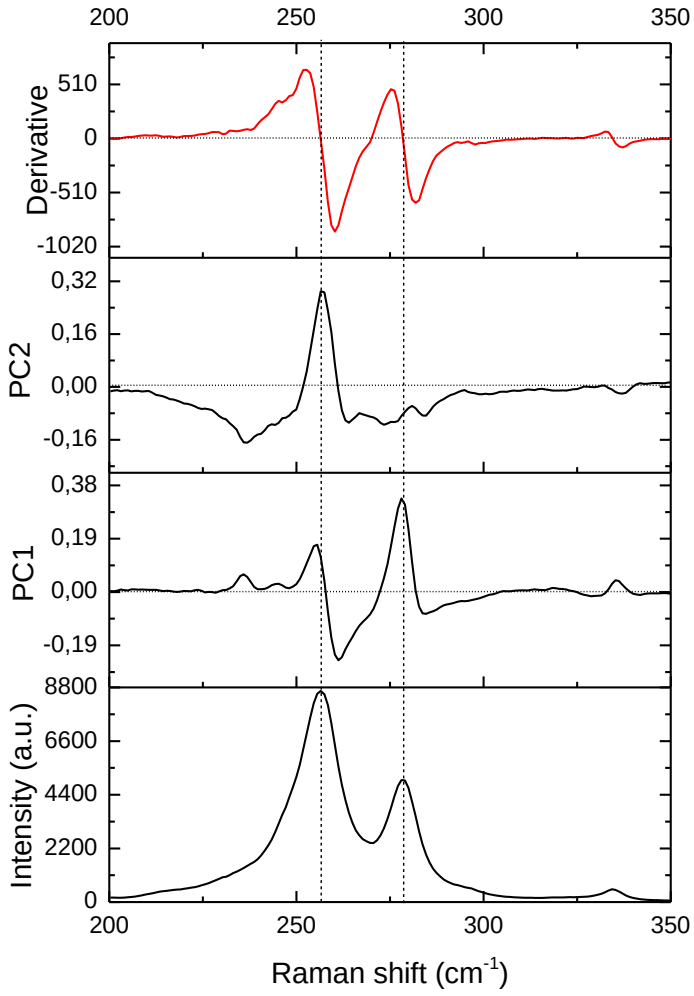

Figure III. 14 *- Loadings of PC1 and PC2 of PCA performed on the spectra (range of 200cm^{-1} – 475cm^{-1})obtained at low temperature 93K, for the Y(ZZ)$\bar{Y}$ configuration. Derivative of the Raman spectra*

One remarks that the variations of components correspond to the peak positions of the mean Raman spectrum. This means that they correspond to the changes of Raman spectra (between different samples). It has to be noted that in this analysis we have 2 peaks and they can have different variations comparing to each other. The PC-1 is similar to the 1st derivative of the spectra so it reflects the shift of the peaks between samples. The peak of the mean spectrum and this of the PC-2 are at the same position, and the PC-2 doesn't look like a derivative. PC-2 represents the intensity change of $A_1[TO_1]$ relatively to $A_1[TO_2]$.

III.III.2 – PCA of Raman spectra obtained at room (300K) temperature

The PCA was performed also for the spectra obtained at room temperature. This provides a possibility to compare them and to confirm the obtained results as well.

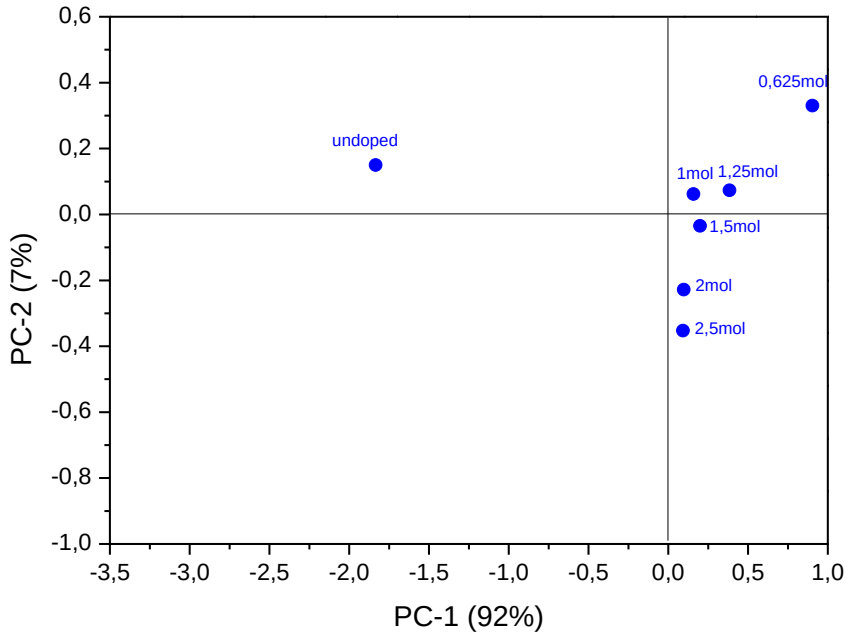

***Figure III. 15**- Scores of spectra (range of 550cm^{-1} – 700^{-1}) of all samples of Y(ZZ)$\bar{Y}$ configuration obtained at room temperature (300K)*

The scores of all spectra are presented in figure III.15. The variance is explained within 99% with PC-1 and PC-2. Comparing these results with the scores of the same mode ($A_1[TO_4]$) we can mention that the behavior is the same according to the consequence of the Zr concentration and the scores of PC-1 and PC-2. The difference is that in the case of low temperature the scores are more "expanded" which is due to the better resolution. In figure III.16 the spectrum of the 1.5mol % ZrO_2:LN is presented and its derivative in order to compare with loadings. As one can see the PC-1 is very similar to the 1st derivative so represents the frequency shift between spectra of samples, and this was the case also for the PC-1 of the same analyses of the spectra at low temperature.

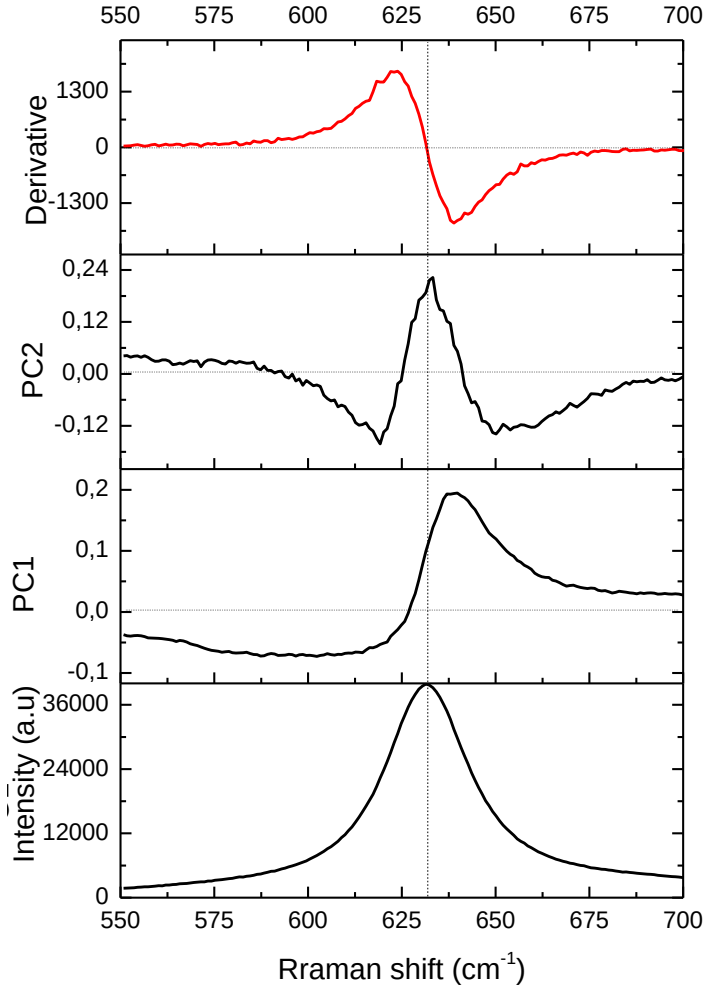

***Figure III. 16**- Loadings of PC1 and PC2 of PCA performed on the spectra (range of 550cm^{-1} – 700cm^{-1}) obtained at room temperature (300K), for the Y(ZZ)$\bar{\boldsymbol{Y}}$ configuration. Derivative of the spectrum of the 1.5mol% Zr sample*

So we can mention that the PCA reproduces the same results for the spectra obtained at low and at room temperatures.

III.IV – Interpretation

III.IV.1 – Comparison of results between both methods

Now we interpret Raman data from the information given by fits and PCA of the spectra. For this at first we compare results derived from these two completely different methods. In figure III.17 the frequency dependence on the concentration obtained by classical fitting of Raman spectra, is compared with the variation of PC-2 which, as mentioned above, reflects the frequency shift (fig III.10).

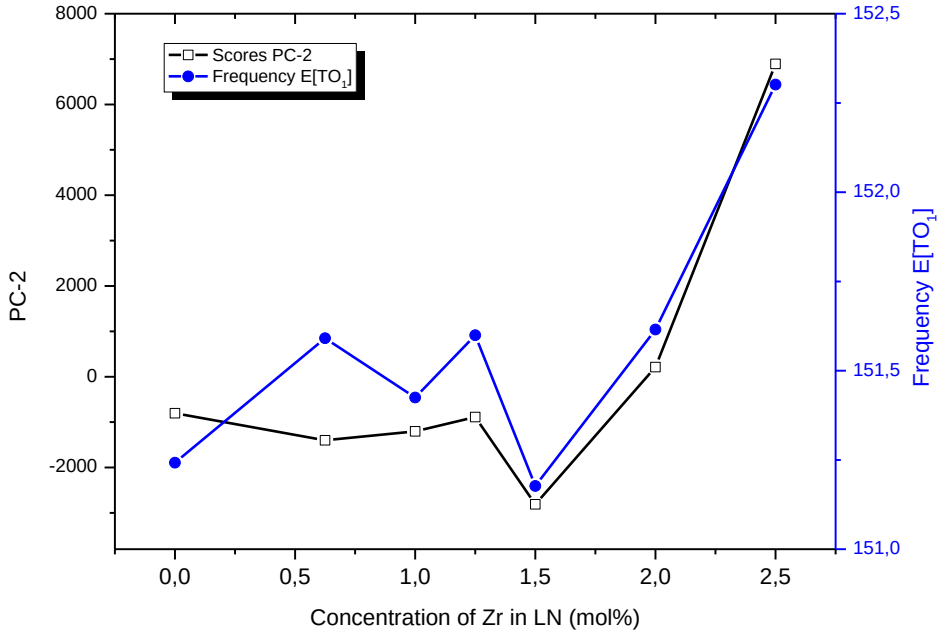

Figure III. 17 *- The frequency of the mode E[TO$_1$] and the scores of PC2 as a function on the concentration of Zr in LN*

A remarkable agreement between these methods is obtained. This corroborates the validity of the dependence of the E[TO$_1$] frequency.

The same dependencies are plotted for the mode A$_1$[TO$_4$] as presented in figure III.18. Fitting results give a frequency increase between the undoped sample and the Zr doped samples. For the same spectra in PCA analysis it was shown that PC-1 (figure III.12) represents the shift of the peak between the spectra of different samples so that this component is compared with the dependence of the A$_1$[TO$_4$] frequency.

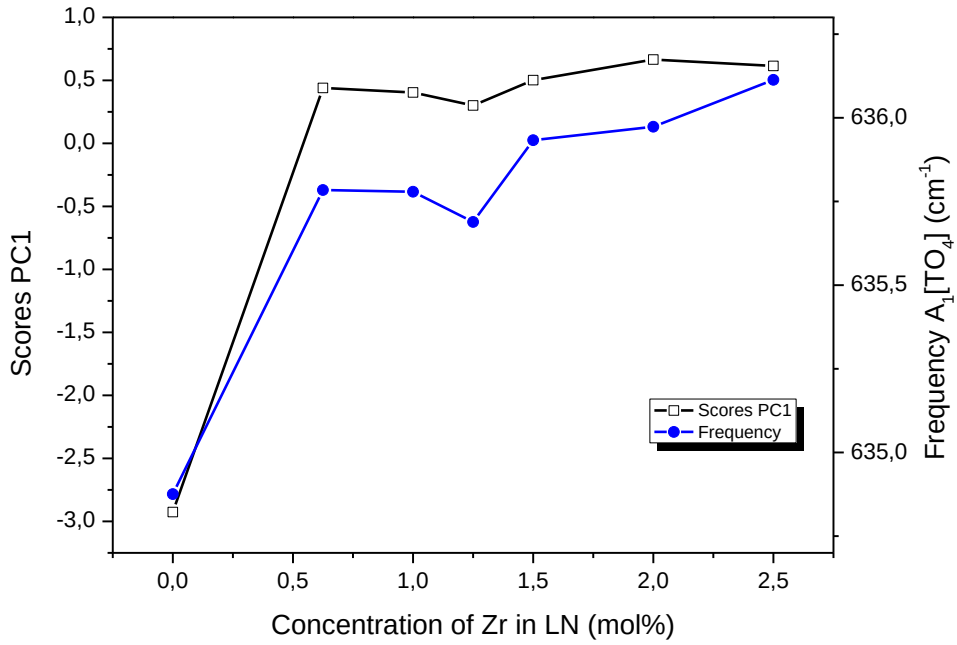

Figure III. 18 *- The frequency of the mode $A_1[TO_4]$ and the scores of PC1 as a function on the concentration of Zr in LN*

Again a very good agreement is achieved.

Now we consider the low-frequency modes $A_1[TO_1]$ and $A_1[TO_2]$. The frequency change with Zr concentration is compared with the score of PC-1 (figure III.19). PC-1 scores explain the common shift of $A_1[TO_1]$ and $A_1[TO_2]$. When there are 2 modes included in the same PCA it is not very visible the results for each mode separately. In other terms PC-1 gives the average shift between both modes. Therefore the dependence for the PC-2 is compared with relative shift $A_1[TO_1]$-$A_1[TO_2]$ (figure III.20). Now a better agreement is obtained showing the consistency between both methods.

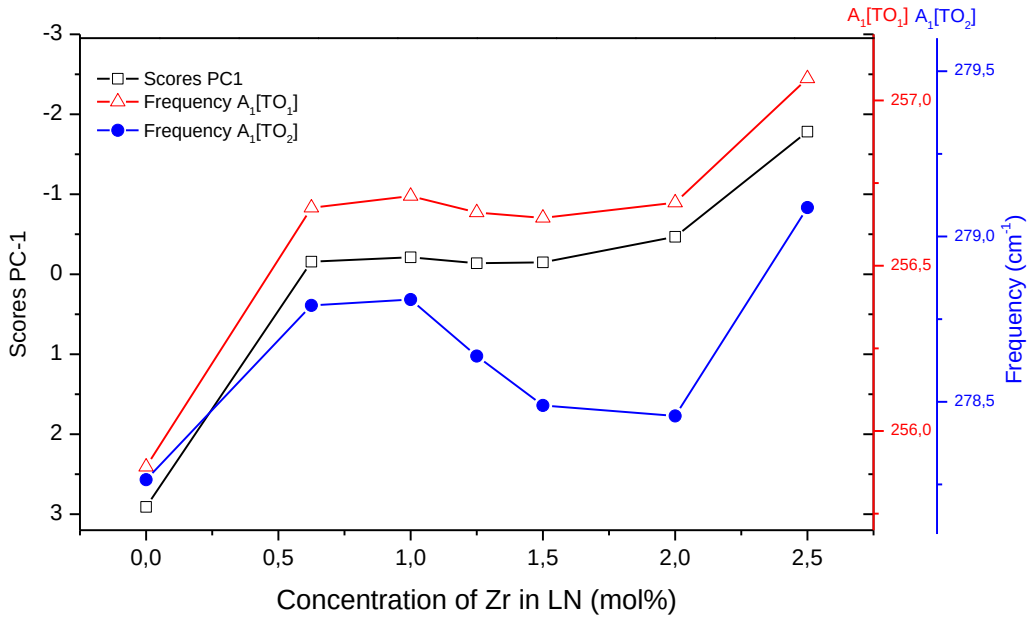

Figure III. 19 *- The frequencies of the modes $A_1[TO_1]$ and $A_1[TO_2]$ and the scores of PC1 as a function on the concentration of Zr in LN*

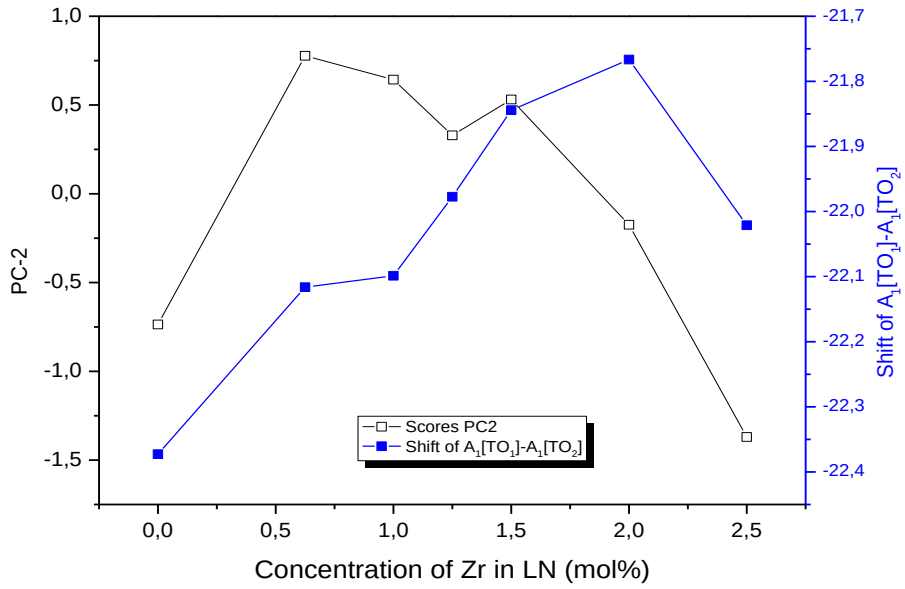

Figure III. 20*- The frequency shift between $A_1[TO_1]$ and $A_1[TO_2]$ and the scores of PC1 as a function on the concentration of Zr*

III.IV.2 – Site occupation

From Raman results we attempt to describe the mechanism of incorporation of Zr ions in LN lattice. We remind that the mode A_1 [TO_1] mainly involves B site, where we have Nb while A_1[TO_2] corresponds to the motion of Li against the oxygen octahedra. Zr ions can at first replace the part of Nb antisites on A site, so that we have a frequency increase of the A_1[TO_2] mode between the undoped and 0.625mol Zr LN. Increasing the concentration of Zr will lead to an increasing occupation of Nb antisites and Li vacancies. When Zr replaces Li as the mass of Zr ion is larger than this of Li ion the frequency of A_1[TO_2] mode decreases till the 2mol % concentration. Starting at 2mol % Zr concentration the Zr ions occupy the site B as well, so the frequency is increasing for A_1[TO_1] and A_1[TO_2] modes reflecting a larger strength of A-O and B-O bands. The mode A_1[TO_4] corresponds to the movement of oxygen octahedral and the frequency is increasing continuously with Zr concentration due to the strengthening of the lattice which becomes more compact. The analysis provides a possibility to conclude that the optical damage threshold is near 2mol% of Zr concentration. This interpretation is in agreement with absorption measurements on the same series of samples. The absorption edge is seen to shift to lower wavelength with Zr content increase and above the threshold, it shift up to larger wavelength [10] (fig. III.21).

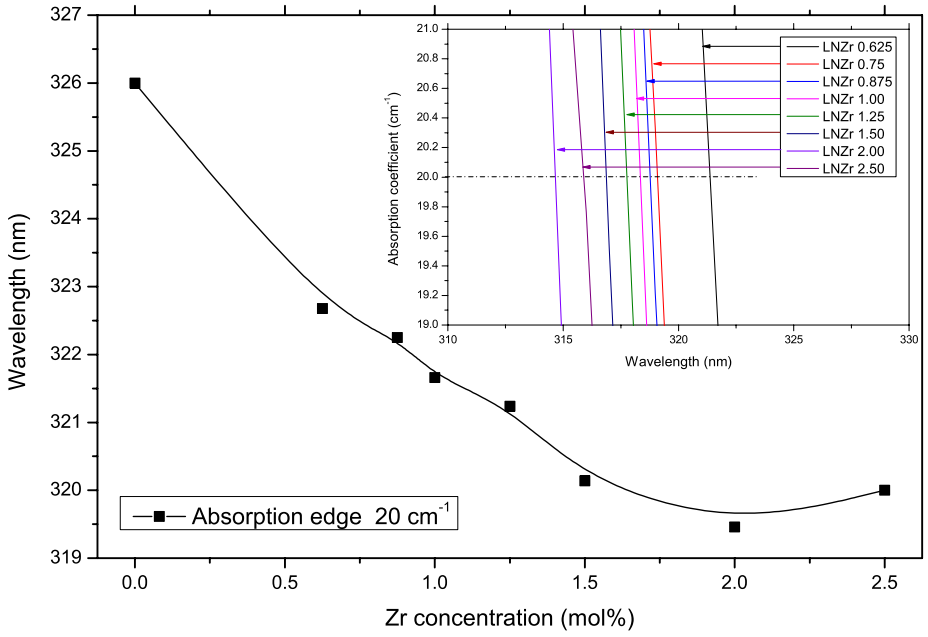

Figure III. 21*- Absorption edge versus Zr concentration in congruent LN doped crystals evaluated from absorption spectra. Insert: Zoom of the absorption spectra in the range of the absorption edge [10].*

III.V – Conclusion

Utilizing Raman technique and the chemometrics method the threshold of Zr doped LN crystals was determined and is near 2mol%, which is in agreement with the results that were obtained using other techniques [8, 9,10]. It was shown that the PCA, even it gives a relative and not an absolute shift, can be used in order to help to determine the threshold. These results provide a possibility to use the PCA to derive the relative change in the spectra among many samples and to deduce a hierarchy of these samples using the classical fitting procedure.

III.VI – References

[1] T. R. Volk and M. Woehlecke. Ferroelectrics Review **1**, 195 (1998)

[2] G.I. Malovichko, V.G. Grachev, E.P. Kokanyan, O.F. Schirmer et al. *"Characterization of stoichiometric LiNbO3 grown from melts containing K_2O"* Appl.Phys. A 56, 103 (1993).

[3] M.Fontana, K.Chah, M.Aillerie, R.Mouras, P.Bourson. "*Optical damage resistance in undoped $LiNbO_3$ crystals"*, Optical Materials 16, 111 (2001)

[4] A.M.Petrosyan, R.K.Hovsepyan, E.P.Kokanyan, R.S.Feigelson. "*Growth and evaluation of lithium niobate crystals containing nonphotorefractive dopants"* Proc. SPIE, 4060, 106, (2000)

[5] E.P.Kokanyan,L.Razzari, I.Cristiani, V.Degiorgio and J.B.Gruber, *"Reduced photorefraction in hafnium-doped single-domain and periodically poled lithium niobate crystals"* Applied Phys. Letters, 84, 1880, (2004).

[6] P.Minzioni, I.Cristiani, V.Degiorgio, and E.P.Kokanyan, *"Strongly sublinear growth of the photorefractive effect for increasing pump intensities in doped lithium-niobate crystals*" Journal of Applied Physics, 101, 116105, (2007).

[7] P.Minzioni, I.Cristiani, J.Yu, J.Parravicini, E.P.Kokanyan, and V.Degiorgio, "*Linear and nonlinear optical properties of Hafnium-doped lithium-niobate crystals" O*ptics Express, 15, 14171, (2007)

[8] G. Nava, P. Minzioni, W. Yan, J. Parravicini, D. Grando, E. Musso, I. Cristiani, N. Argiolas, M. Bazzan, M. V. Ciampolillo, A. Zaltron, C. Sada, V. Degiorgio, *"Zirconium-doped lithium niobate: photorefractive and electro-optical properties as a function of dopant concentration*", -Optical Materials Express, 1, 270 (2011)

[9] Y. Kong, Sh. Liu, Y. Zhao, H. Liu, Sh. Chen, J. Xu, *"Highly optical damage resistant crystal: Zirconium-oxide-doped lithium niobate"*, Appl. Phys. Lett. 91, 081908, (2007)

[10] M. Abarkan, M. Aillerie, N. Kokanyan, C. Teyssandier, E. Kokanyan, *"Electro-optic and dielectric properties of Zirconium-doped congruent lithium–niobate crystals*", Optical Materials Express 4, 179, (2014)

[11] R. N. Balasanyan, V. T. Gabrielyan, E. P. Kokanyan, and I. Feldvari, "*Composition and homogeneity of LiNbO3 crystals in connection with growth conditions.I, The influence of electrical field".* Kristallografiya 35, 1540, (1990)

[12] T. R. Brown, R. Stoyanova, *"NMR spectral quantitation by Principal-Component Analysis. II. Determination of frequency and phase shifts"* Journal of Magnetic Resonance, B112, 31, (1996)

[13] H. Witjes, M. van den Brink, W.J. Melssen, L.M.C. Buydens, *"Automatic correction of peak shifts in Raman spectra before PLS regression"*, Chemometrics and Intelligent Laboratory Systems 52, 105, (2000)

Chapter IV
Time dependence of Raman spectra in photorefractive Fe doped LN

IV.I – Introduction

Photorefractive properties of Lithium Niobate crystals are associated with the presence of space charge field, and the defocusing of the beam inside the crystal (Chapter I). In particular the space charge field can lead to a strain of the lattice due to the piezoelectric property of the crystal. In this chapter it will be shown how these mentioned effects can be reflected in the Raman spectra.

The chapter is divided into two parts. In the first part are reported and analyzed the data obtained by means of forward and backward Raman scattering on Fe doped LN crystals, pointing out the influence of the defocusing on the breaking of Raman selection rules. In the second part the shift of the frequency of some lines is analyzed to evidence the photoreftactive induced strain effect.

IV.II – Experimental Part

Forward and backward scattering Raman measurements were performed on a 0.06mol% Fe doped LN crystal and the spectra were recorded as a function of time. The sample has dimensions of 20x60x24 mm^3. Backscattering measurements were performed utilizing the Horiba ARAMIS Raman spectrometer, with 532nm excitation laser which has a power of 10mW on the sample. Forward scattering experiments were performed with our own set up especially mounted for this aim and presented below. A laser with a radiation at the wavelength of 532nm and having a power of 350mW was used.

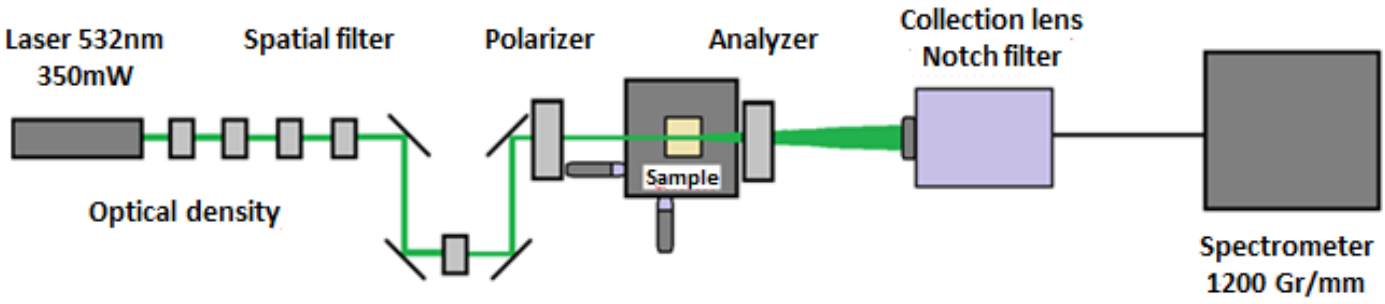

Figure IV. 1*– Scheme of the experimental set up of forward scattering Raman spectrometer*

A Notch filter was used with 200cm^{-1} half width, so all the spectra of forward scattering shown below are cut below 200cm^{-1}. Two linear polarizers with a range 500nm-700nm are fixed, one in front of the sample and the other behind the sample as the analyzer. The lens of 40cm focal length was utilized in order to have a parallel beam in the sample, which provides the possibility to obtain the homogeneous excitation in the sample. The power of the laser was measured in front of sample with a powermeter and was managed by the optical density to be 50mW for all measurements. We use this high power for forward Raman measurements because the beam goes through the sample, by contrast with backscattering experiments where the beam is focused on the surface of the sample with a depth of about 1μm.

During forward scattering measurements the beam passes through the sample which has the thickness from 20 up to60mm according to the direction propagation.

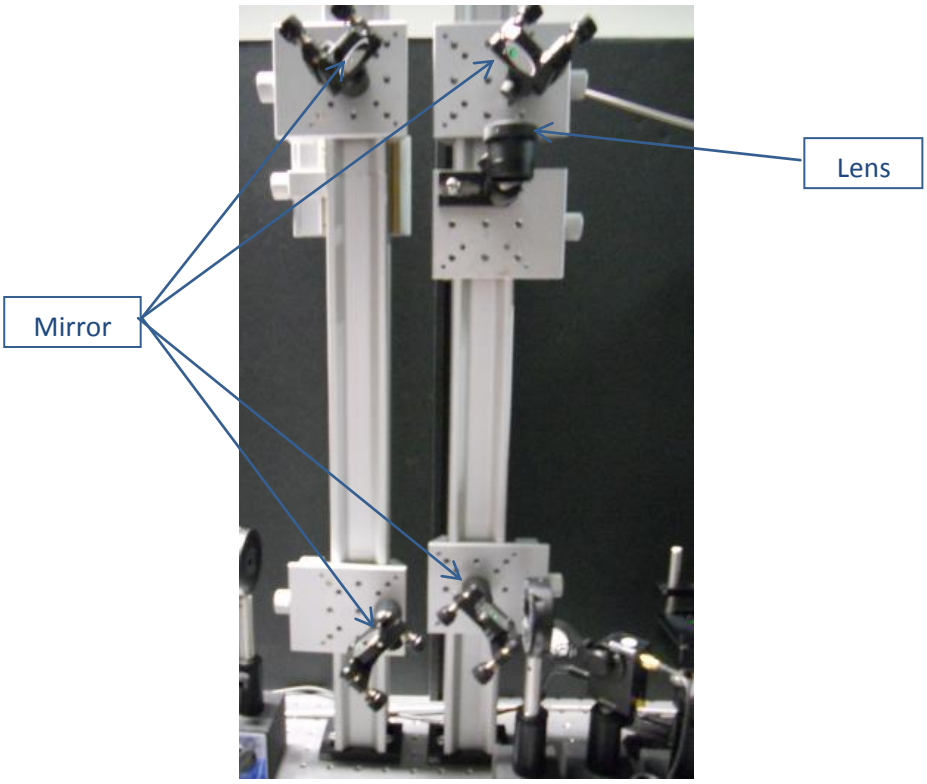

Figure IV. 2– *System with lens in order to have a parallel beam inside the sample*

As all configuration measurements Raman means were performed on the sample and the defocusing of the beam was simultaneously detected. In order to eliminate the memory effect related to the photorefractive effect, a white lamp was fixed near the sample during 45 minutes which allows to "refresh" the sample. In the case of the configuration X(YZ)X it was checked that the detection of lines is found to be the same before and after "refreshing" the sample without changing the point under study. It has to be mentioned that as we have demonstrated changing the point has the same "effect" as the refreshment with the white lamp. As a consequence we change the point on the sample between each measurement in order to eliminate the memory effects.

IV.III – Results

Time dependence Raman spectra were recorded in the backward and forward scattering configurations. Data obtained in different configurations and for both scatterings are presented.

- ***X(ZY)X***

For the configuration X(ZY)X in both forward and backscattering we observe the lines E[TO] as it is expected by Raman selection rules (figures IV.3 and IV.4).

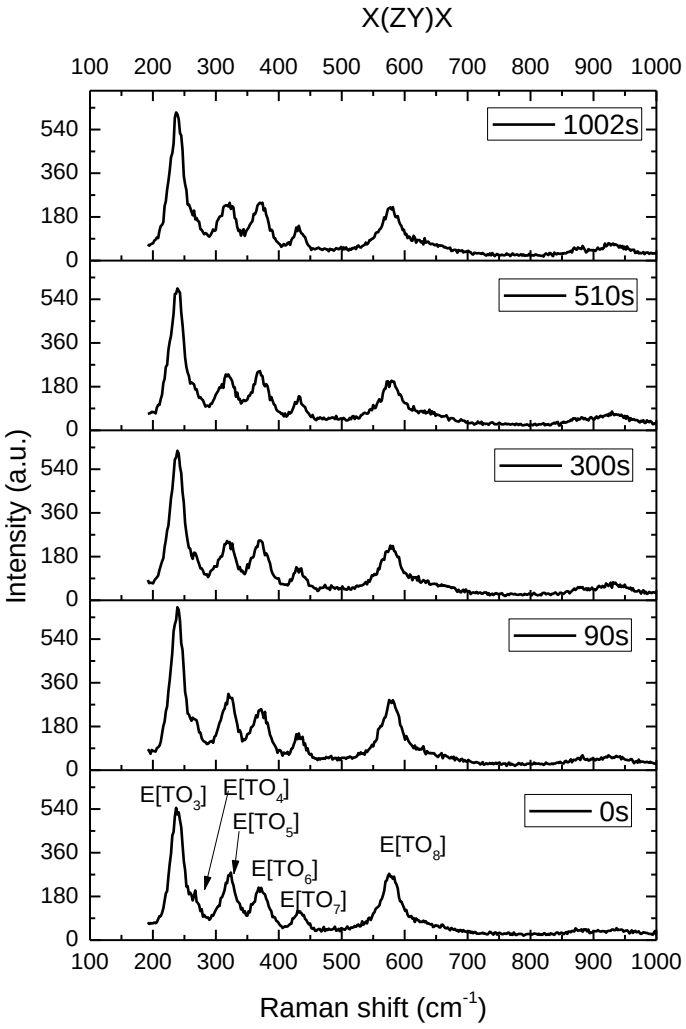

Figure IV. 3*– Forward Raman spectra as a function of time for the configuration X(ZY)X*

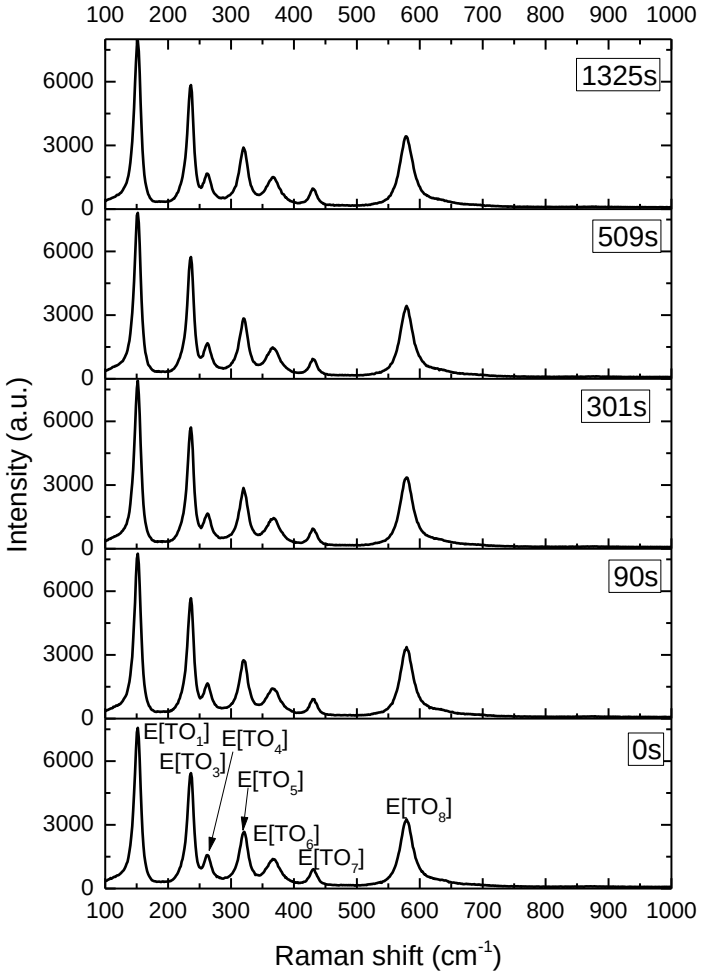

Figure IV. 4*– Backscattering Raman spectra as a function of time for the configuration X(ZY)$\overline{X}$*

It has to be noted that we don't observe any change of the lines neither in their positions, nor in their intensity as a function of time. We don't observe any anomaly. In addition we have recorded the pattern of the scattered beam as a function with time. The image of the emerging ray was projected and recorded on a screen at a distance of about 35 cm between the sample and the screen.

In figure IV.5 the pattern after the sample recorded for the configuration X(ZY)X is presented. It can be noted that the beam remains a centered beam and doesn't change with time.

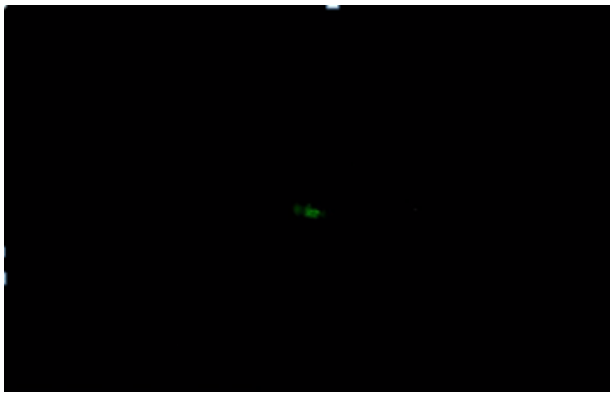

a) 12 seconds

b) 60 seconds

c) 240 seconds

***Figure IV. 5**– Image of forward scattering on Fe doped LN at 12 seconds, 2 minutes and 4 minutes, for the configuration X(ZY)X (Z axis is vertical)*

- ***X(YZ)X***

The evolution of the forward Raman spectra with time is plotted in Figure IV.6. The forward scattering spectrum is completely different to which is expected according to selection rules since A_1[TO] are additionally activated. Furthermore the spectrum shows a large change with time. Thus, while at 0s, the spectrum consists of the expected (according to Raman selection rules) E[TO] modes only, it exhibits mainly A_1[TO] modes after a long time (4 minutes) (figure IV.7).

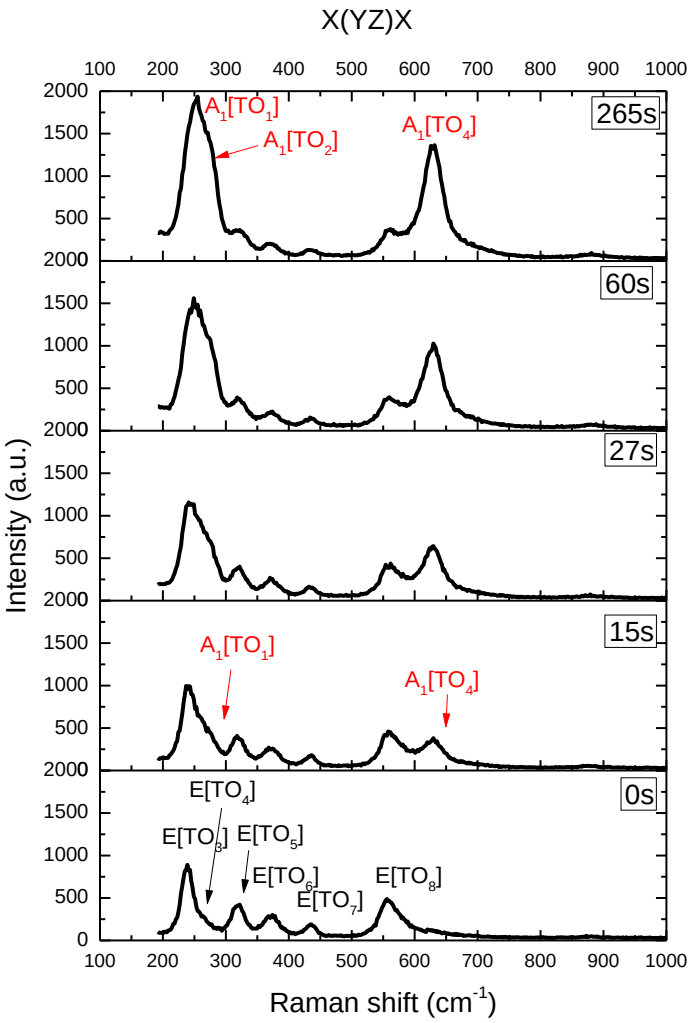

Figure IV. 6*– Forward Raman spectra as a function of time for the configuration X(YZ)X*

By contrast, the spectra obtained in backscattering do not display the same features – we only observe E[TO] lines and a small leakage of A_1[TO_4] mode (figure IV.7). Furthermore the spectrum doesn't change with time.

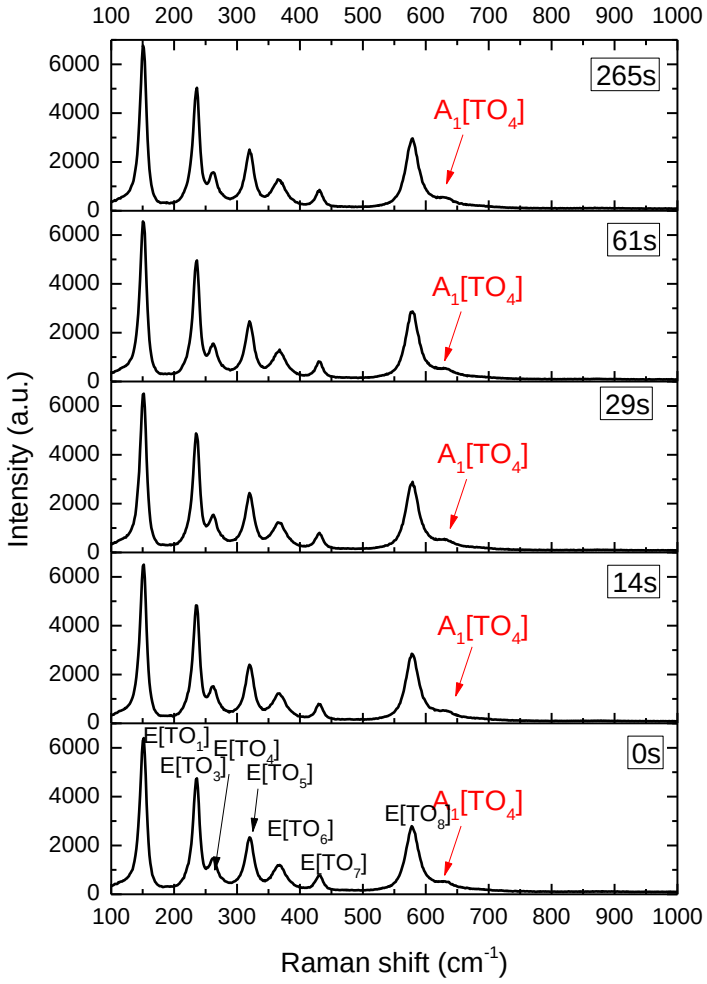

***Figure IV. 7**– Backscattering Raman spectra as a function of time for the configuration X(YZ)$\overline{X}$*

The forward scattered beam images recorded at different times are presented in figure IV.8. One can notice that the beam image changes with time with its extent along the axis Y and Z. In addition 2 lobes become more intense with time. The mentioned pictures report a defocusing of the beam along Y and Z axis (more defocused along Y than along Z).

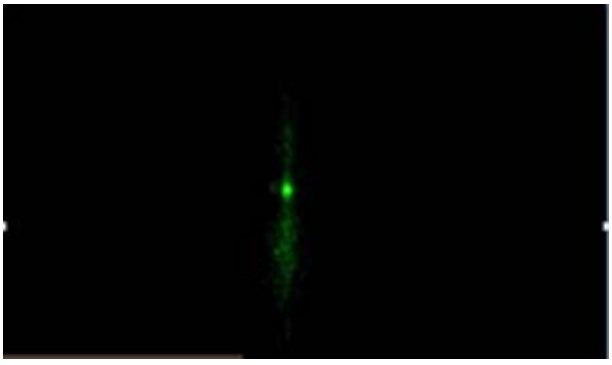

a) 20 seconds

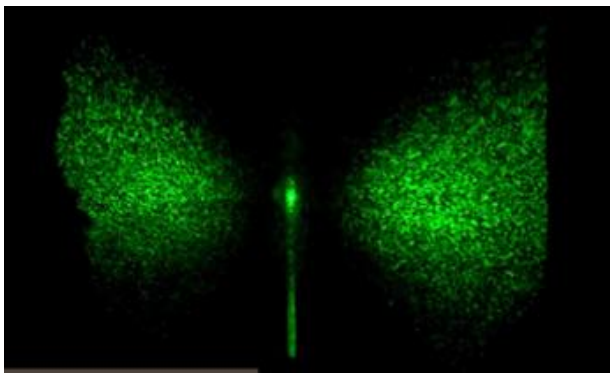

b) 80 seconds

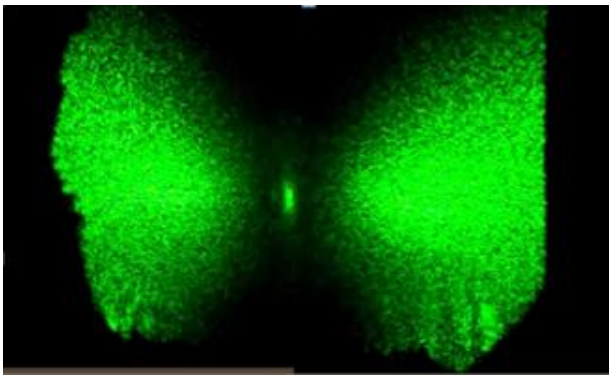

c) *220 seconds*

Figure IV. 8*– Recorded pattern in forward scattering at 20 seconds, 80 seconds and 220 seconds, for configuration X(YZ)X for Fe doped LN (Z axis is vertical to the image)*

- ***X(YY)X***

For the configuration X(YY)X both modes A_1[TO] and E[TO] are expected according to Raman selection rules, in forward and backscattering. Forward Raman spectra are presented as a function of time for this configuration in figure IV.9.

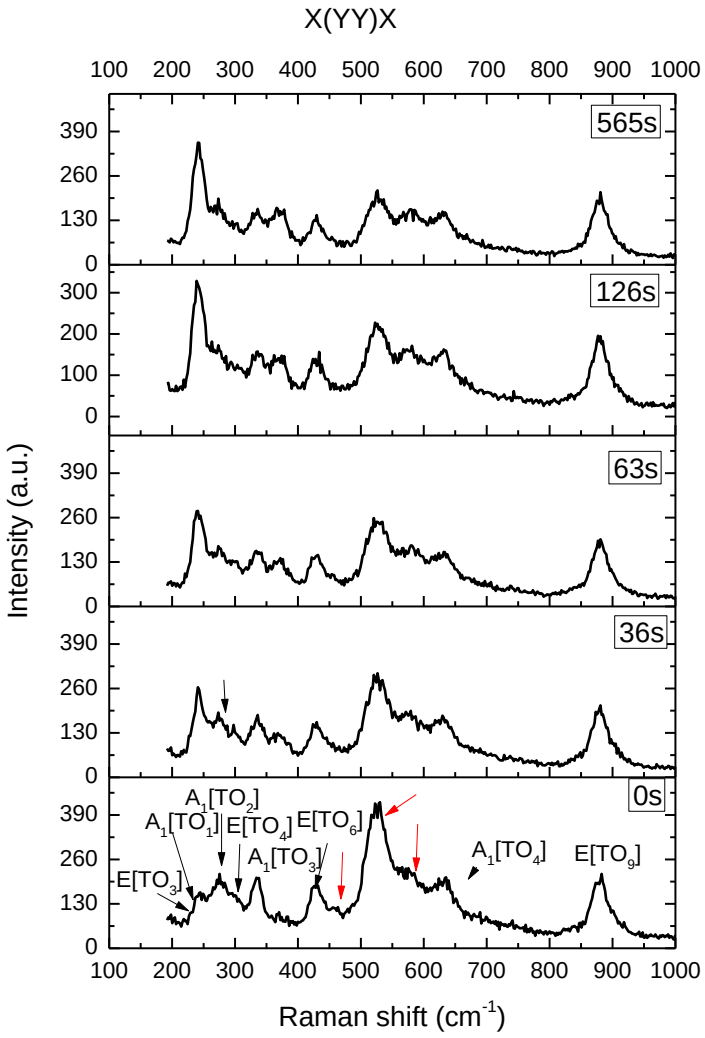

Figure IV. 9– *Forward Raman spectra as a function of time for the configuration X(YY)X. Red arrows indicate unexpected peaks as mentioned*

One can see that the lines A_1[TO] and E[TO] are obtained as expected, and we have in addition 3 unexpected peaks near 453cm^{-1}, 524cm^{-1} and 580cm^{-1}. Small variations of intensity with time are noticed for the mode $A_1[TO_1]$ and the peak at 524cm^{-1}.

Spectra in backscattering are plotted in figure IV.10. One can notice that the modes E[TO] and A_1[TO] are obtained as expected and the spectrum doesn't change with time.

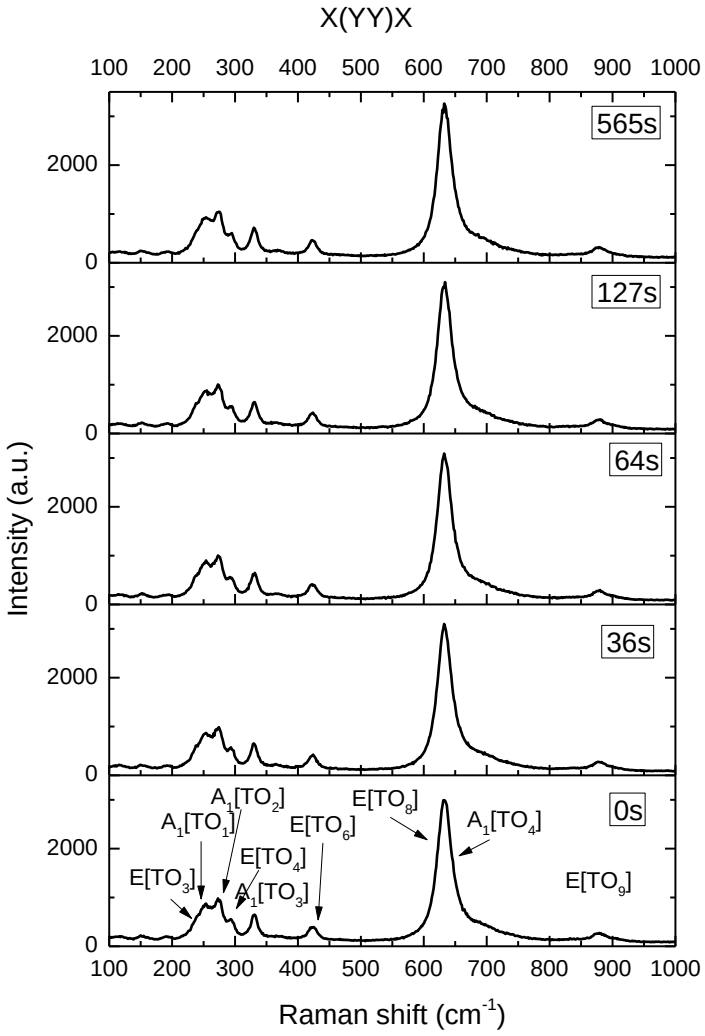

Figure IV. 10– *Backscattering Raman spectra as a function of time for the configuration X(YY)$\overline{X}$*

Spectra in backscattering and forward scattering are compared in figure II.11. It can be seen that the intensity of forward-scattering spectra is smaller and more noisy, comparing to backscattering. The positions of expected lines are the same for both cases and the forbidden 3 peaks obtained only at forward scattering are clearly evidenced.

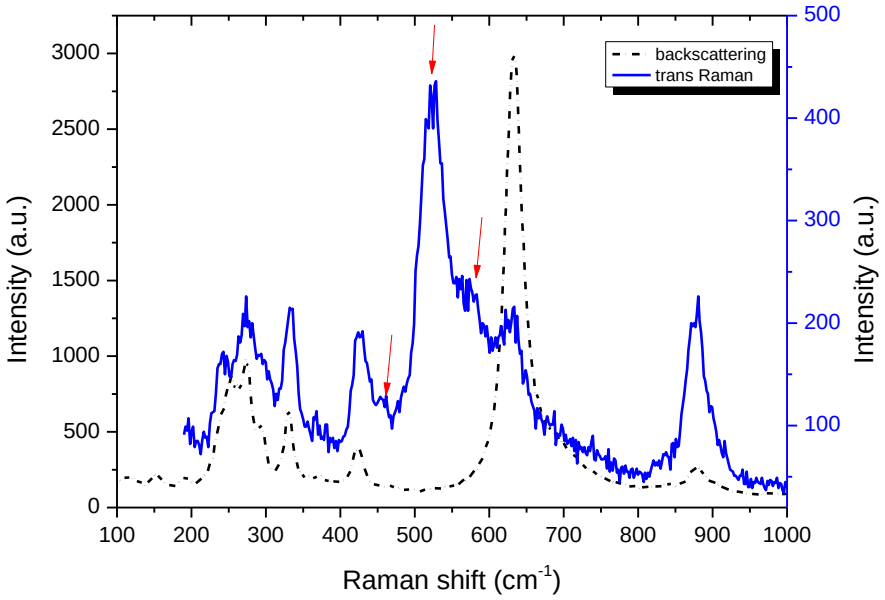

Figure IV. 11– *Backscattering and forward Raman spectra recorded at 0s for the configuration* $X(YY)\overline{X}$ *(X)*

The forward scattered beam shown in the figure IV.12 exhibits a large defocusing along the Z axis.

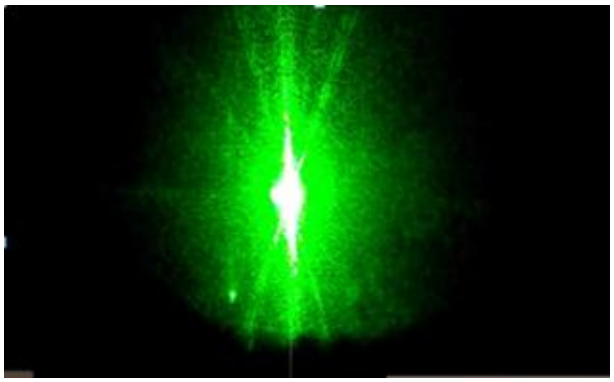

a) 2 seconds

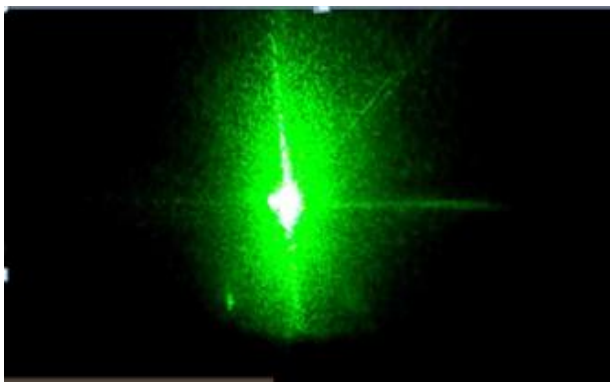

b) 148 seconds

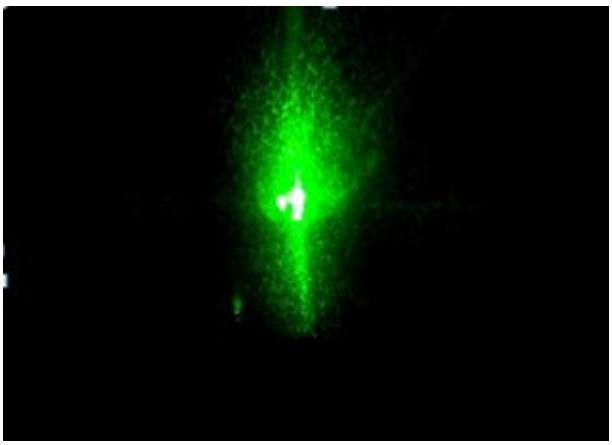

c) 360 seconds

***Figure IV. 12**– Image of forward scattering at different times for configuration X(YY)X for Fe doped LN (Z axis is vertical to the image)*

It has to be mentioned that for the configuration Y(XX)Y the modes A_1[TO] and E[LO] are expected according to selection rules. In forward scattering, the same additional lines as for X(YY)X configuration are detected (near 453cm^{-1}, 524cm^{-1} and 580cm^{-1}). Defocusing of the pattern along Z is recorded as well.

- ***X(ZZ)X***

In the configuration X(ZZ)X only the modes A_1[TO] are expected according to selection rules for forward and backscattering Raman. For this configuration the evolution with time of the forward Raman spectra are presented in figure IV.13. In addition of the expected A_1[TO] modes, 4 forbidden lines are observed near 433cm^{-1}, 524cm^{-1}, 575cm^{-1} and 875cm^{-1}. Some intensity changes of forbidden lines are observed with time.

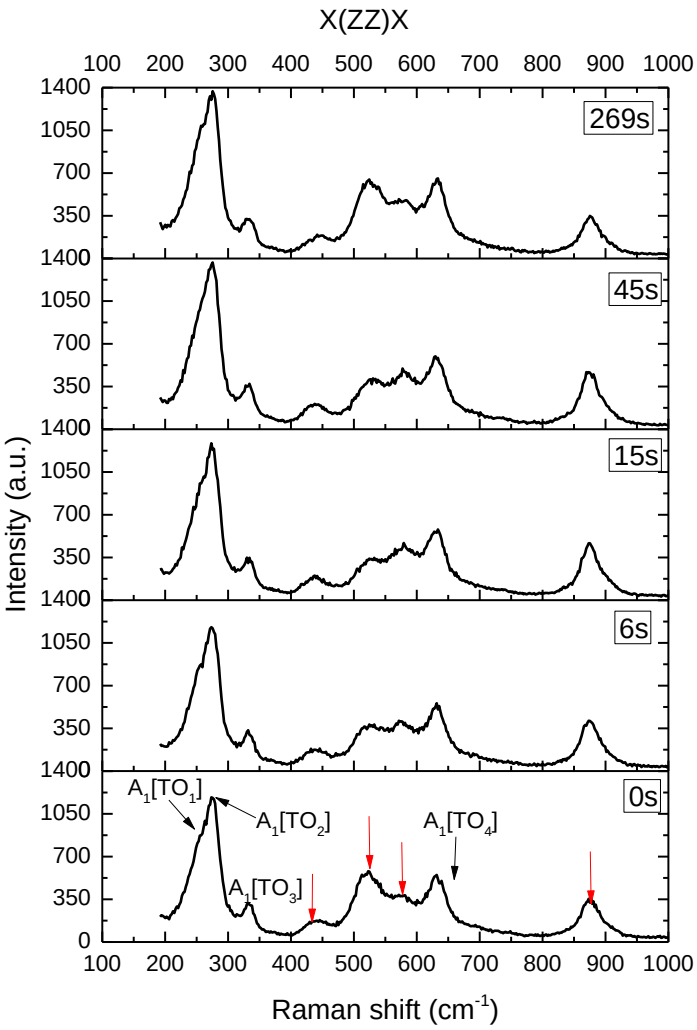

Figure IV. 13 *– Forward Raman spectra as a function of time for the configuration X(ZZ)X*

As seen in figure IV.14, only 4 lines A_1[TO] are present as expected in the backscattering spectra and the spectra doesn't change with time.

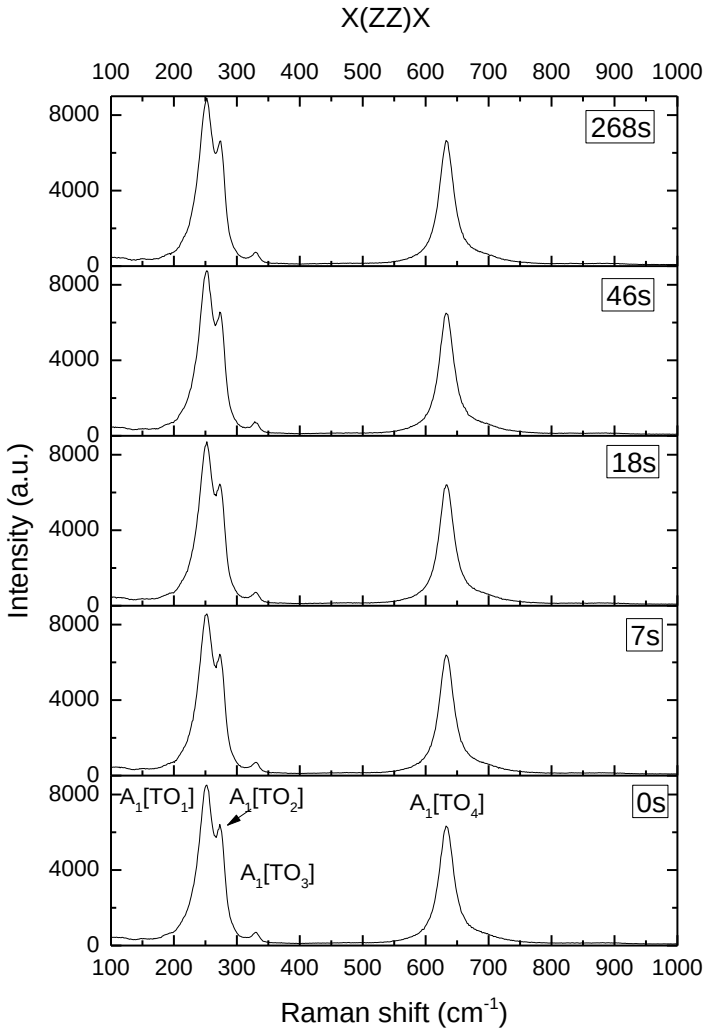

Figure IV. 14*– Backscattering Raman spectra as a function of time for the configuration X(ZZ)$\overline{X}$*

The comparison in the spectra between the backward and forward scattering reported in figure IV.15 underlines the large difference showing the activation in forward scattering of 4 forbidden lines as follows:

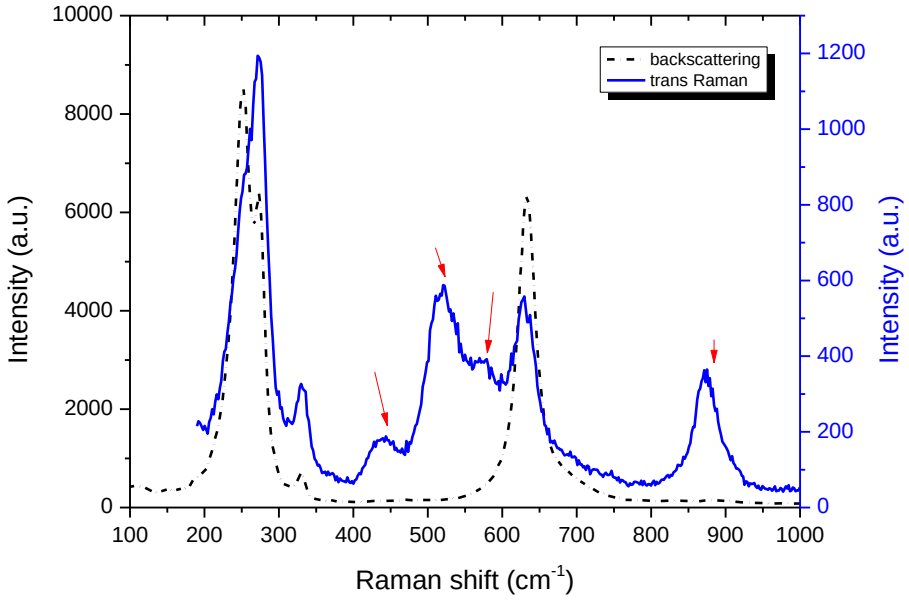

Figure IV. 15*– Backscattering and forward Raman spectra as a function of time for the configuration* $X(ZZ)\overline{X}$ *(X)*

It has to be noted that the spectra obtained with a beam propagation along Y give the same information as the spectra along X. The patterns of the forward scattered beam in figure IV.16 show a constant defocusing along Z axis constant with time.

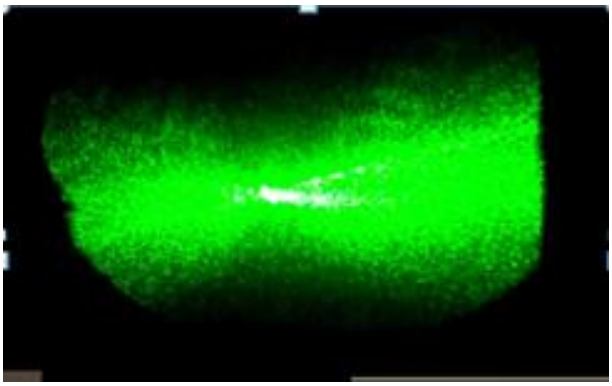

a) 2 seconds

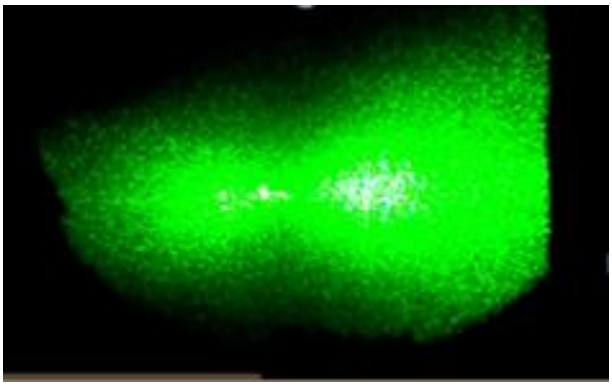

b) 144 seconds

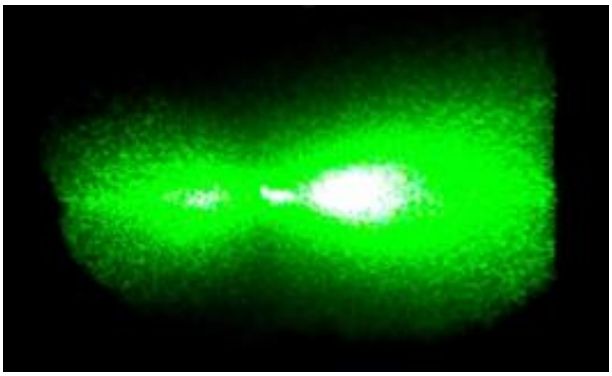

c) *340 seconds*

Figure IV. 16– *Image of forward scattering at different time for the configuration X(ZZ)X for Fe doped LN (Z axis is horizontal to the image)*

- ***Z(YY)Z***

The modes E[TO] and A_1[LO] are expected for the configuration Z(YY)Z according to Raman selection rules for forward and backscattering. In forward Raman spectra (fig. IV.17) it is seen that forbidden peaks near 300cm^{-1}, 518cm^{-1}and 626cm^{-1} are detected in addition to expected E[TO] and A_1[LO] modes. The spectrum doesn't change with time, except the change in intensity of the peak at 518cm^{-1}.

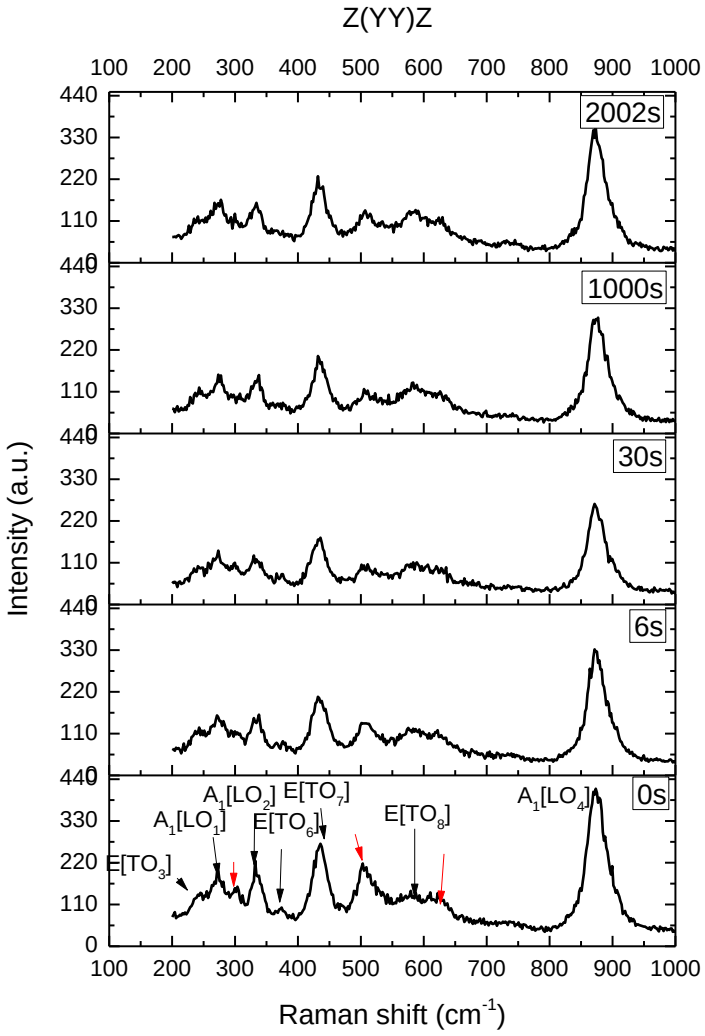

***Figure IV. 17**– Forward Raman spectra as a function of time for the configuration Z(YY)Z*

The backscattering spectra show some changes with time. Thus at 0s the lines E[TO] and A_1[LO] are obtained as expected, then after some time (20 seconds) a new peak at a 625cm^{-1} appears besides these lines (figure IV.18). The same behavior as in Z(YY)Z in forward and backscattering spectra was obtained also for the configuration Z(XX)Z.

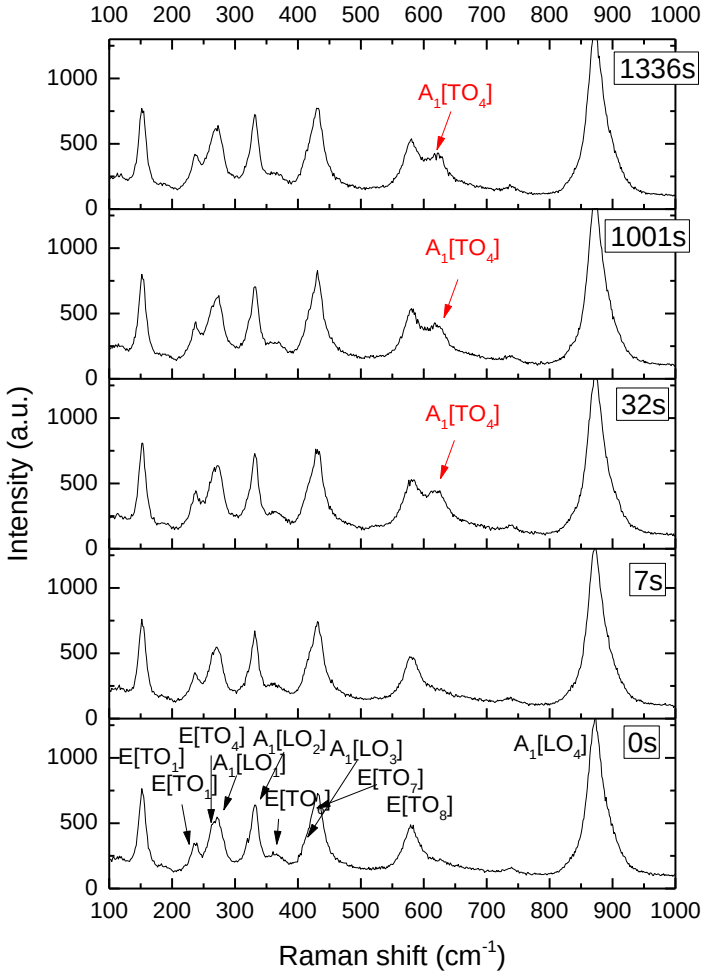

Figure IV. 18– *Backscattering Raman spectra as a function of time for the configuration Z(YY)$\bar{Z}$*

The recorded pattern of the forward scattered beam is presented in figure IV.19. A circular defocusing is detected normal to Z-axis.

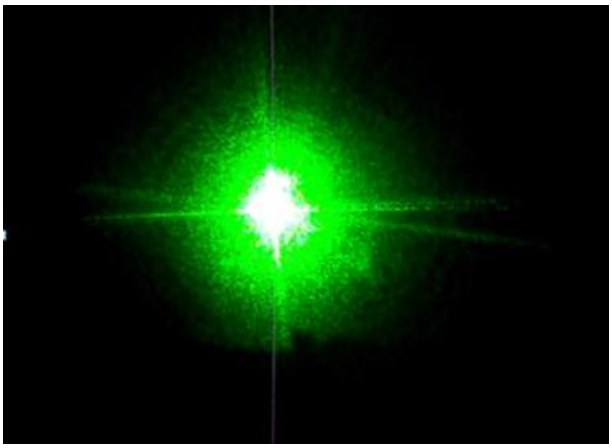

a) 2 seconds

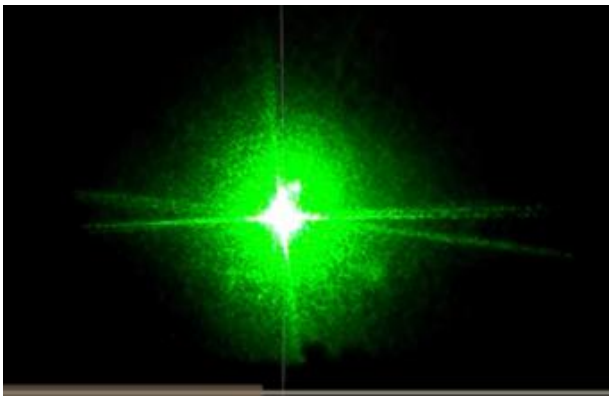

b) 56 seconds

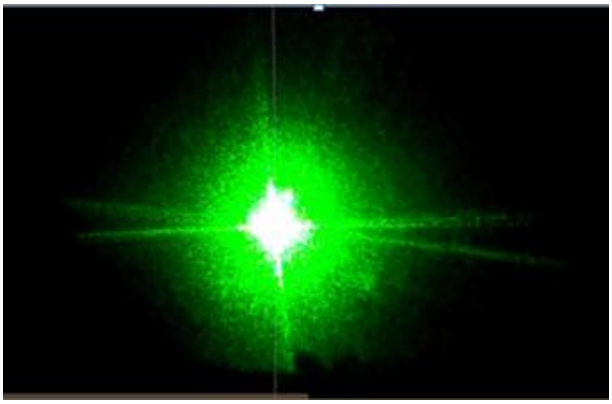

c) 340 seconds

***Figure IV. 19**– Image of forward scattering at different times for the configuration Z(YY)Z for Fe doped LN (Z axis is ,normal to the plane of the image)*

- ***Z(XY)Z***

Only the modes E[TO] are expected. The time dependence of the Raman spectra obtained at forward scattering is shown in fig. IV.20. Beside the E[TO] modes, unexpected lines near 301cm^{-1}, 516cm^{-1} and 874cm^{-1} are detected. No change was observed with time.

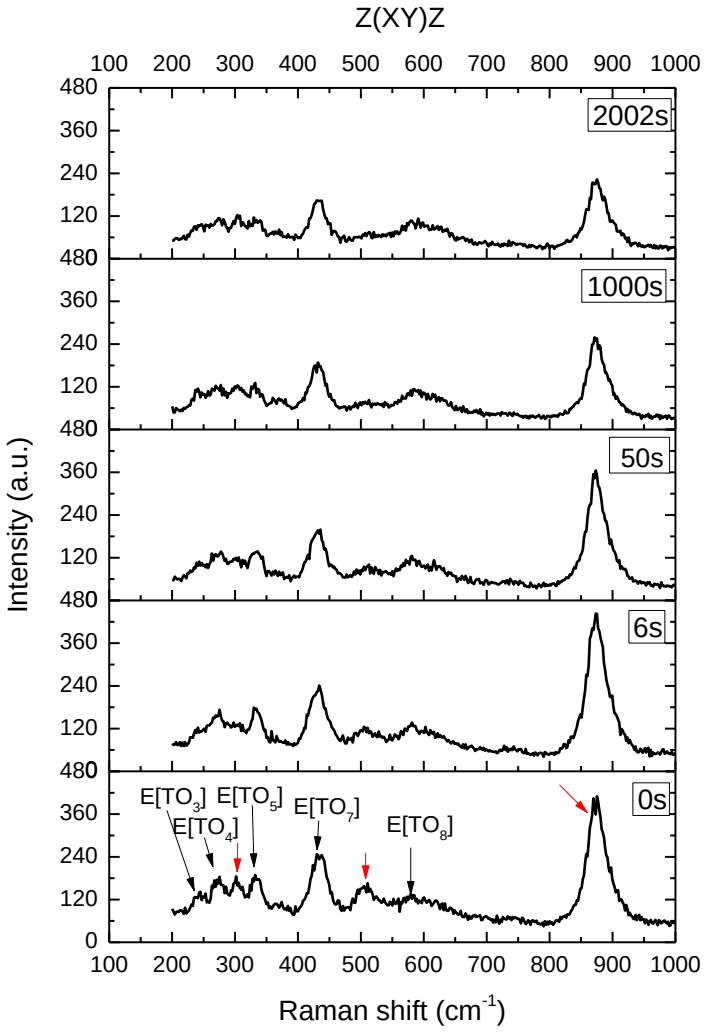

Figure IV. 20– *Forward Raman spectra as a function of time for the configuration Z(XY)Z*

In backscattering spectra an unexpected peak near 875cm^{-1} is detected and the band near 626cm^{-1} increases with time (figure IV.21*)*.

The comparison between the forward and backscattering shows the relative intensity difference between the lines and points out the additional forbidden lines in forward scattering (fig. IV.22).

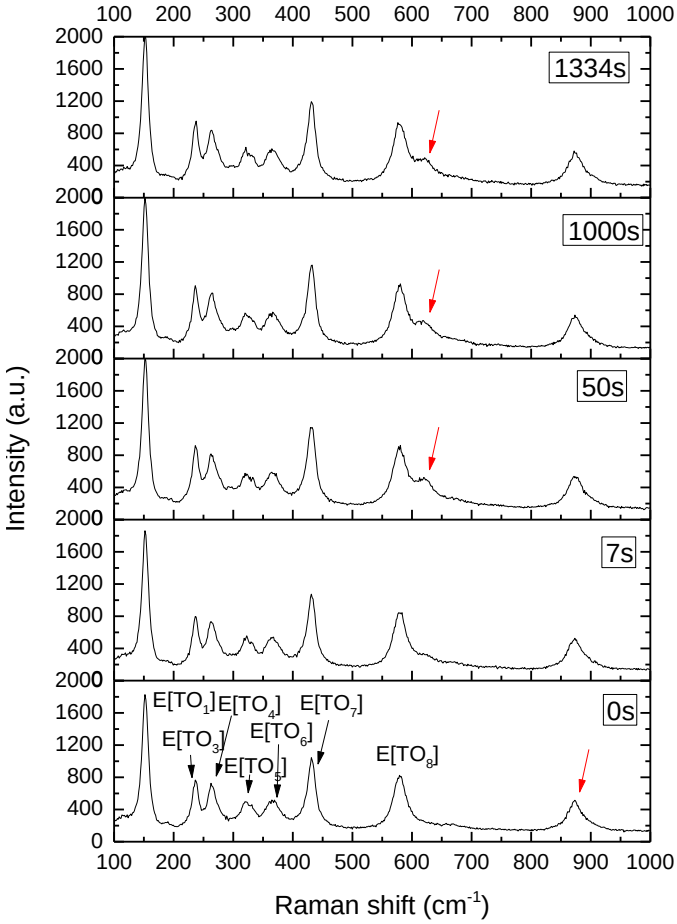

***Figure IV. 21**– Backscattering Raman spectra as a function of time for the configuration $Z(XY)\overline{Z}$*

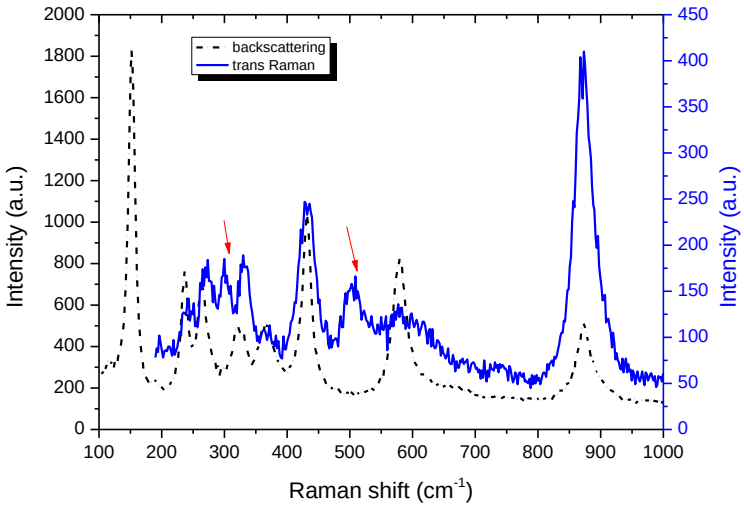

***Figure IV. 22**– Backscattering and forward Raman spectra recorded at 0s for the configuration $Z(XY)\overline{Z}$ (Z)*

Same results as Z(XY)Z are obtained for the configuration Z(YX)X. The forward scattered beam pattern shows a circular defocusing (figure IV.23).

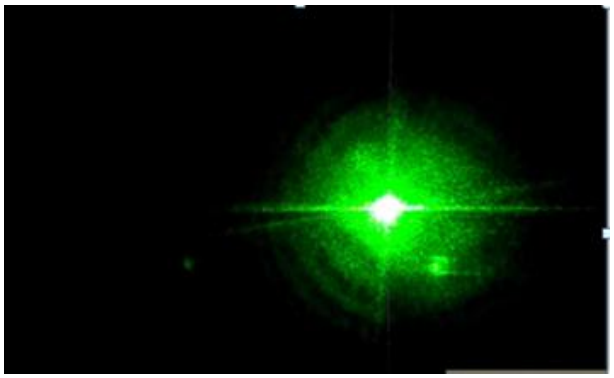

a) 2 seconds

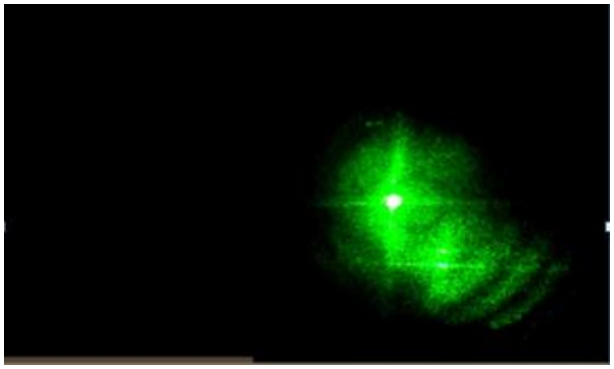

b) 48 seconds

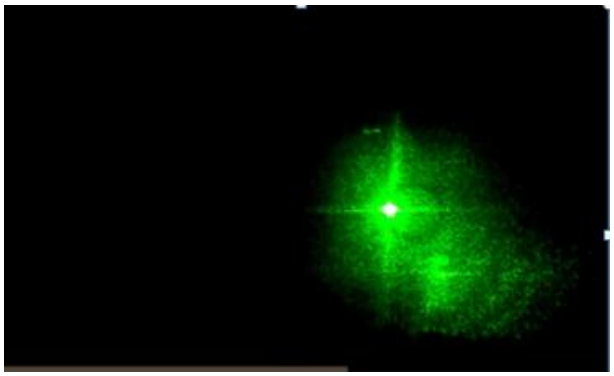

c) *180 seconds*

Figure IV. 23*– Image of forward scattering on Fe doped LN at different times for the configuration Z(XY)Z (Z axis is normal to the image plane)*

IV.IV – Interpretation

Summarizing and comparing the forward and backscattered Raman spectra, we observe that while in backscattering expected lines were generally obtained, in forward scattering several forbidden lines are present with a time dependence for all configurations except X(ZY)X (or Y(ZX)Y) for which only expected lines were detected. The results are reported in table IV.1 (with the main information on the pattern of the forward scattered beam).

Configuration	**Expected modes by selection rules**	**Detected lines in backscattering**	**Detected lines in forward scattering**	**Forward scattered beam pattern**
X(ZY)X/Y(ZX)Y	E[TO]	E[TO]	E[TO]	No defocusing
X(YZ)X/Y(XZ)Y	E[TO]	E[TO]+$A_1[TO_4]$	E[TO]+A_1[TO]	Extent along Y (X) and Z
X(YY)X	E[TO]+A_1[TO]	E[TO]+A_1[TO]	E[TO]+A_1[TO]+ forbidden lines at 453cm^{-1}, 524cm^{-1}, 580cm^{-1}	Extent along Z
X(ZZ)X/Y(ZZ)Y	A_1[TO]	A_1[TO]	A_1[TO]+ forbidden lines at 433cm^{-1}, 524cm^{-1}, 575cm^{-1}, 875cm^{-1}	Extent along Z
Y(XX)Y	E[LO]+A_1[TO]	E[LO]+A_1[TO]	E[LO]+A_1[TO]+ forbidden lines at 453cm^{-1}, 524cm^{-1}, 580cm^{-1}	Extent along Z
Z(YY)Z/Z(XX)Z	E[TO]+A_1[LO]	E[TO]+A_1[LO] +625cm^{-1}	E[TO]+A_1[LO]+ forbidden lines at 300cm^{-1}, 518cm^{-1} and 626cm^{-1}	Circular extent
Z(XY)Z/Z(YX)Z	E[TO]	E[TO] + peak at 626cm^{-1} and 875cm^{-1}	E[TO]+ forbidden lines at 301cm^{-1}, 516cm^{-1} and 874cm^{-1}	Circular extent

Table IV. 1*– Expected and obtained Raman modes for forward and backscattering measurements. The direction of defocusing of the pattern in forward scattering is reported as well*

We can underline three points as follows:

- In the configuration X(ZY)X the forward and backscattering Raman spectra shows only the E[TO] modes as expected by Raman selection rules (table IV.1) and there is no defocusing detected in the recorded pattern.
- In the configuration X(YZ)X while the backscattering spectra gives only expected E[TO] modes (except the small leakage of $A_1[TO_4]$ mode), spectra obtained in forward scattering shows a large activation of A_1[TO] modes dependent on time. At

the same time, the defocusing of the forward scattered pattern is observed along Z and Y directions (more along Y compared with Z).

- For all configurations corresponding to the propagation direction along Z in forward scattering Raman spectra, some forbidden lines are detected and the circular defocusing of the recorded pattern is detected (consequently with the equivalence of X and Y axis).

We can conclude that there is a strong link between the defocusing of the scattered beam and the detection of forbidden lines in the Raman spectra recorded in forward scattering. The interpretation as follows is based upon this observation. The defocusing or the extent of the scattered beam has as an obvious consequence that the incident and scattered beams are no longer collinear. This leads to some deviation from selection rules which assume this co-linearity. Subsequently the phonon wave vector (or beam transfer through the crystal) is strongly dependent on the beam defocusing. The phonon wave vector has therefore an extra component beside the main component along the incident beam direction.

The scattering geometry for the determination of the directional dispersion of phonons is shown in figure IV.24.

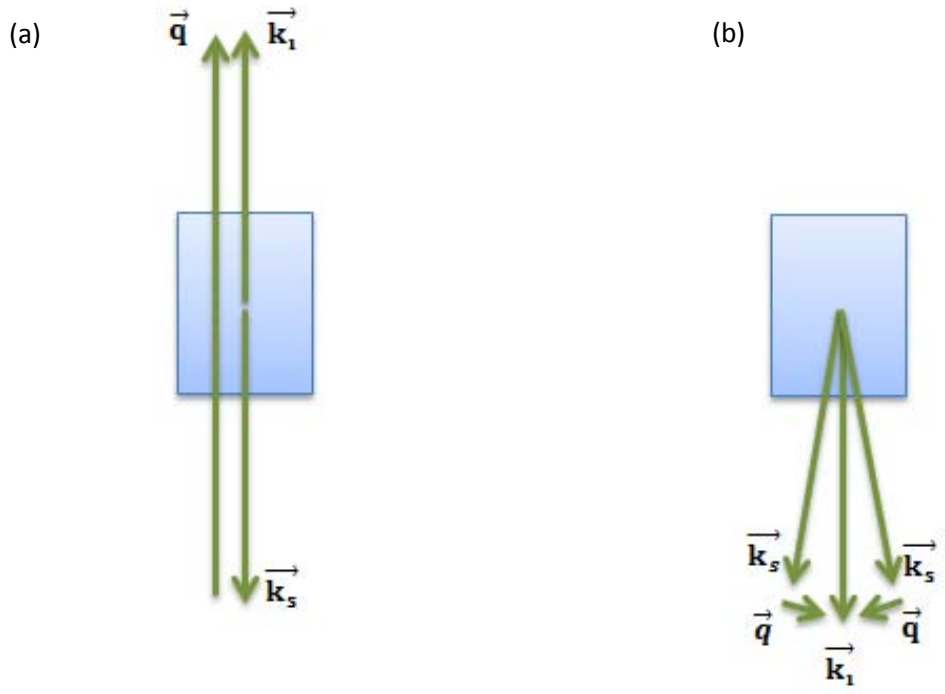

Figure IV. 24*- (a) backscattering geometry (b) forward scattering geometry* $\mathbf{k_i}$ *and* $\mathbf{k_s}$ *are the wave vectors of incident and scattered light respectively, and the* $\mathbf{q}$ *is the phonon wave vector.*

Two cases can be encountered. In the first case **q** is in the plane normal to the optical axis, so in the ordinary plane. In the second case **q** is in the extraordinary plane (the wave vector is in the planes normal to X or Y axis) and makes an angle with Z axis. In this case some quasi-modes (neither A_1, nor E symmetry) can be detected. The frequencies of these quasi-modes depend on the angle θ between **q** and Z and can be obtained from the dispersion when θ varies between 0 and 90^o. The spectra were recorded under a set of angles between wave vector and optical axis by X.Yang et al [1]. In figure IV.25 the dispersion of modes depending on the angle between the incident and optical axis is presented.

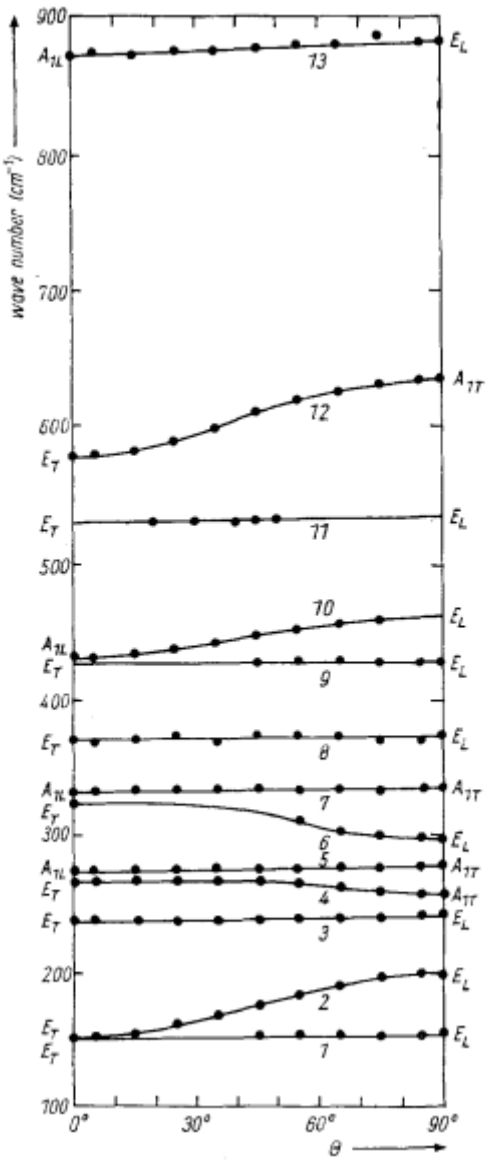

***Figure IV. 25**–Directional dispersion branches of phonons in LN [1]*

One can notice that the frequencies of forbidden lines shown in the table above can be found in this figure. This can be explained by the plane where the wave vector is according to directions of defocusing of the pattern. For the configuration X(YZ)X the defocusing of the beam along Y and Z axis were observed mainly along Y so the phonon vector has additional Y components. The phonon wave vector is in the ordinary plane. When defocused through the sample the incident beam is therefore depolarized so that the component (ZZ) of the Raman tensor can be considered. (ZZ) corresponds to activation of A_1[TO] lines consequently with our observation with time. The line intensity increase with time is simultaneous with the intensity change of the scattered beam.

The defocusing along Z was detected for the configurations X(YY)X and X(ZZ)X. In this case the wave vector has also a Z component and is in the extraordinary plane. This means that the quasi-modes can appear which is in agreement with obtained spectra.

A circular defocusing was detected for the configurations Z(YY)Z and Z(XY)Z. In this case the wave vector is along Z and must have components along X and Y, so will be in the extraordinary plane and as it was mentioned quasi-modes can be present for these cases.

It has to be mentioned that the quasi-mode detected near 524cm^{-1} was seen in all spectra where quasi-modes were present. The frequency of this quasi-mode is quite different of the frequency of normal Raman lines. As it was mentioned in the work of X.Yang et al. (fig.IV.25), the mode near 530cm^{-1} appears at the angles nearly from 20^o to 50^o between the propagation direction and the optical Z axis. And this peak isn't present at back and 90^o scatterings.

IV.IV – Strain effect induced by the photorefractive effect

In addition to the activation of forbidden Raman lines discussed above, we observe in both back- and forward- scattering Raman measurements a shift of the position of some lines, which is dependent on time: This shift is discussed in terms of strain induced via piezoelectric effect by the space charge field associated with photorefractive effect.

IV.IV.1 – Backscattering

IV.IV.1.1 – Experimental part

Four different Fe:LN samples were grown by the Czochralski method with dimensions of about 10 x 10 x 1 mm^3 with the major (X) surface optically polished. The effective concentration of Fe^{2+} and $Fe^{3+}$are reported in table IV.2. We first report data obtained by backscattering using the Horiba ARAMIS Raman spectrometer with the excitation line of 633 nm.

Sample code and description	**Fe concentration (%mol.)**	**[Fe^{2+}] (x10^{24}at./m^3)**	**[Fe^{3+}] (x10^{24}at./m^3)**	**[Fe^{2+}]/[Fe^{3+}]**
Fe:LN 0.1 O (oxidized)	0.1	0	18.8	<0.01
Fe:LN 0.1 AG (as-grown)	0.1	0.46	18.34	0.025±0.008
Fe:LN 0.1R (reduced)	0.1	5.29	13.5	0.39±0.01
Fe:LN 0.05	0.05	1.57	7.83	0.20±0.01

Table IV. 2*– Summary of sample codes and characteristics*

Raman spectra as a function of time in configuration X(ZZ)$\overline{X}$ (modes A1(TO)) and X(YZ)$\overline{X}$ (modes E(TO)) were collected and analyzed. The peak frequency of each Raman line was fitted and the results were plotted as a function of time. The acquisition time of a Raman spectrum is significantly shorter than the photorefractive time constant of the material. In a given sample, the speed of the PR phenomenon is influenced primarily by the intensity of the illumination pattern, so that it is mandatory to use low intensities to have large time constants. Also, the confocal aperture plays an important role. In order to obtain fast acquisition times,

we had to use a large pinhole size (fixed at 400 μm) and consequently large detection volume; this has important consequences in the dynamics of the measured signal, as it will be shown below. In the following we used a 10x objective and an excitation beam with a wavelength of 632.8 nm. The incident power was varied by means of three neutral density filters and measured before the sample surface with the help of a portable power meter to be in the range between 10 and 0.1 mW.

IV.IV.1.2 – Results

By observing the time evolution of the Raman spectra we found that in general all Raman peak frequencies shift with time. Although all the modes are shifted of a comparable amount, the phenomenon is particularly evident for the A1[TO_4] mode because this line is intense, well separated and with a relatively high frequency of ~ 632 cm^{-1} which makes it particularly sensitive to any perturbation of the lattice structure. In figure IV.26 it is reported the time evolution of the $A_1(TO_4)$ frequency shift for samples Fe:LN 0.05 and Fe:LN 0.1-AG. The shift evolves according to a saturation behavior and reaches a limit value as high as 0.7 cm^{-1} and 1.4 cm^{-1} for the sample Fe:LN 0.05 and Fe:LN 0.1-AG, respectively (see table IV.2 for sample description).The time evolution of the frequency shift depends on the light intensity, becoming faster for higher intensities.

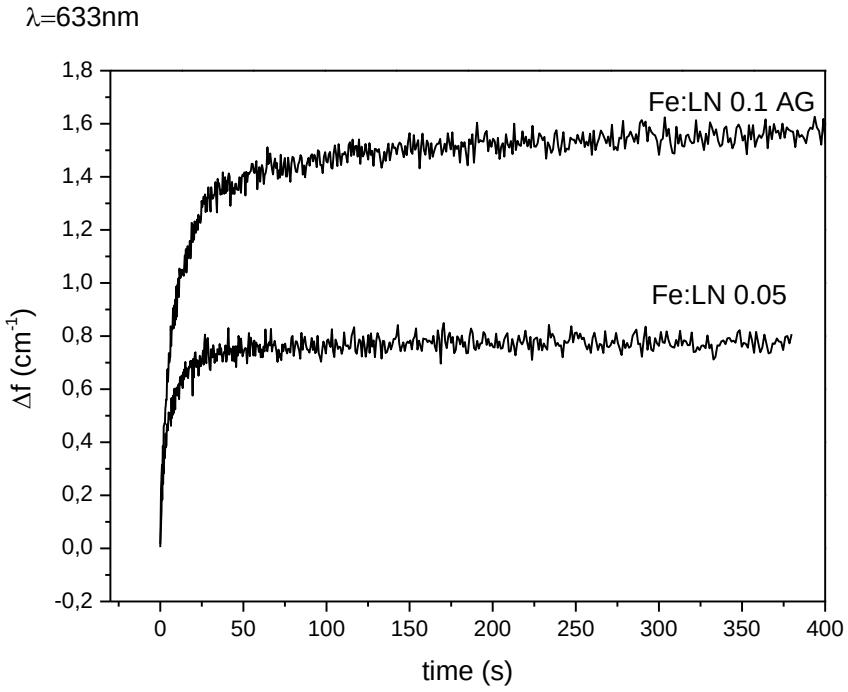

Figure IV. 26*-Time evolution for the peak frequency of the A1[TO_4] mode in samples Fe:LN 0.05 and Fe:LN 0.1 asgrown (see table IV.2)*

IV.IV.1.3 – Discussion and Analysis

It is clear that the time dependent shift of the Raman lines is due to some kind of local modification induced by the excitation beam in the sample. A change in Raman lines frequency can be due to several reasons, such as a change in the sample temperature or stress. Our first aim is therefore to figure out what are the important couplings responsible for the observed shifts in the Raman spectra.

In Figure IV.27 are represented the possible effects arising when an absorbing lithium niobate sample is illuminated with a laser beam, together with the possible couplings between the different fields. The arrow *B*, the photo-induced charge transport, is of particular interest to us. It is known [2-5] that typical space charge fields in Fe:$LiNbO_3$ samples can easily reach values as high as ~10^{-7} V/m, with a major component along the positive z direction.

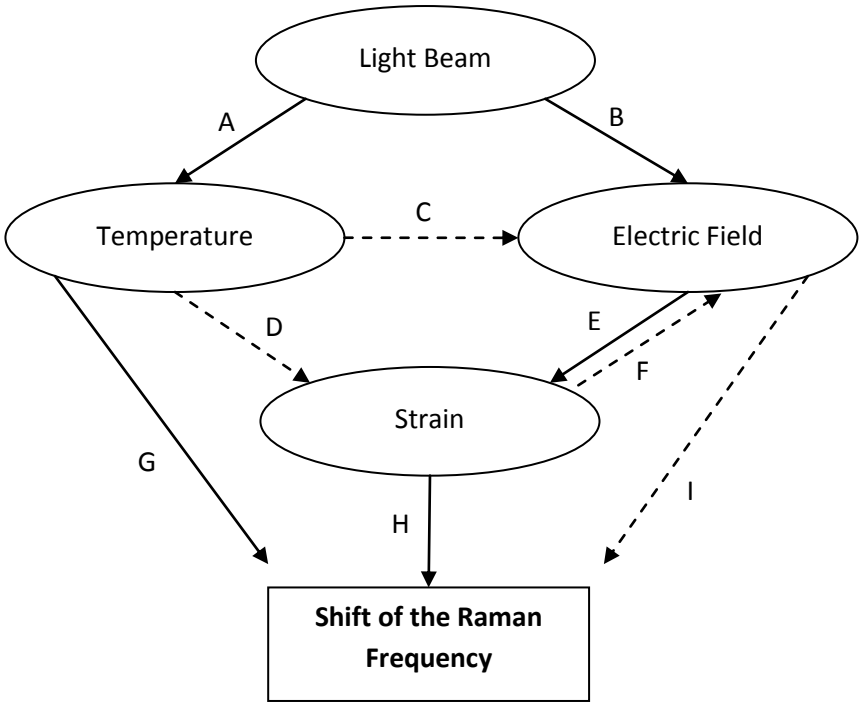

Figure IV. 27*– Scheme of the possible couplings between different light induced effects in Fe:LN. Dashed arrows represent contributions that can be neglected*

It is known that strain may modify the frequencies of Raman modes. As LN is piezoelectric, the photorefractive electric field is able to induce such a strain, affecting indirectly the lattice modes frequency (figure IV.27).

In our experiments we aim at investigating the effect of a light-induced space charge field on the Raman spectra. This study can be compared with the changes in the Raman spectra directly induced by a static electric field or a temperature change applied on the sample. Therefore, we also performed a series of experiments which were useful to clarify our observations. The effect of a static electric field on the Raman spectra was evaluated in the following way: a couple of planar electrodes were deposited on the X surface of an undoped LN sample, leaving between them a gap of about 100 µm, so that the electric field was along the Z direction. Those electrodes were connected with a power supply able to span a voltage range of 1 kV, which can be doubled by inverting the electrical connections with the sample. We measured the Raman spectra in backward scattering at different voltages focusing at the surface of the region between the electrodes, using the lowest possible power and an excitation wavelength at 785 nm, in order to limit to the maximum possible extent the influence of the photorefractive effect. When the field is ramped between -10^7 to 10^7 V/m, a linear change in the frequency of the Raman modes is observed. By repeating several times our experiments and by fitting the obtained dependences with a linear law we were able to estimate a calibration coefficient Raman frequency/Electric field of $+0.5\text{x}10^{-7}$ cm^{-1} mV^{-1} for the $A_1[TO_4]$ mode (Figures IV.28).

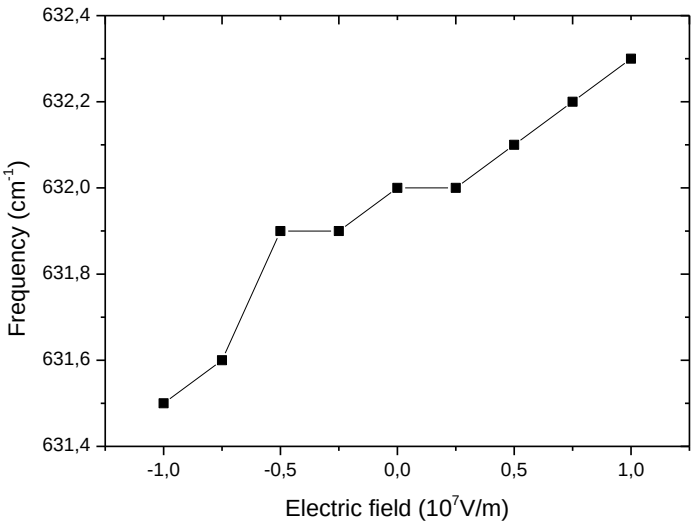

Figure IV. 28- *Frequency dependence of the mode $A_1[TO_4]$ on the electric field by sequence*

Moreover the PR effect on the Raman spectrum has to be distinguished from other contributions, such as those deriving from sample heating, which may play a role during the Raman measurements Then, in order to verify whether the heating of the sample due to the

sample absorption can affect the Raman modes frequency, we performed also measurements of the Raman frequency change due to the sample temperature with the 633 nm excitation line. A pure lithium Niobate sample (i.e. with negligible absorption) was mounted into a thermal stage and measured between room temperature and 675K (appendix A). The experiments as function of temperature show an opposite behavior since in the explored range the frequency is shifted to lower values by increasing the temperature. From our data we obtained a time dependent coefficient with temperature of -0.024 $cm^{-1}K^{-1}$ (appendix A).

IV.IV.2 – Forward scattering

In the previous part it was shown that the frequency shift with time is originated by the photo-induced space charge field through to the piezoelectric effect. As it was seen in forward scattering measurements for the configuration X(YZ)X (or Y(XZ)Y) unexpected A_1[TO] modes are activated with time and after long time the A_1[TO] are mainly present. In this part we will report the frequency shift of these activated modes A_1^*. We will concentrate on the same Raman line ($A_1[TO_4]$) as for the backscattering case. For these measurements the samples with 0.03mol and 0.05mol % Fe were used, for each concentration of Fe oxidized and as grown samples were measured. The frequency values were fitted by the LabSpec software which provides a possibility to fit the peak and reproduce the dependence with time. In figure IV.29 the shift of forbidden $A_1[TO_4]$ (we will name it $A_1[TO_4]^*$) line as a function of time is presented for two concentrations of Fe.

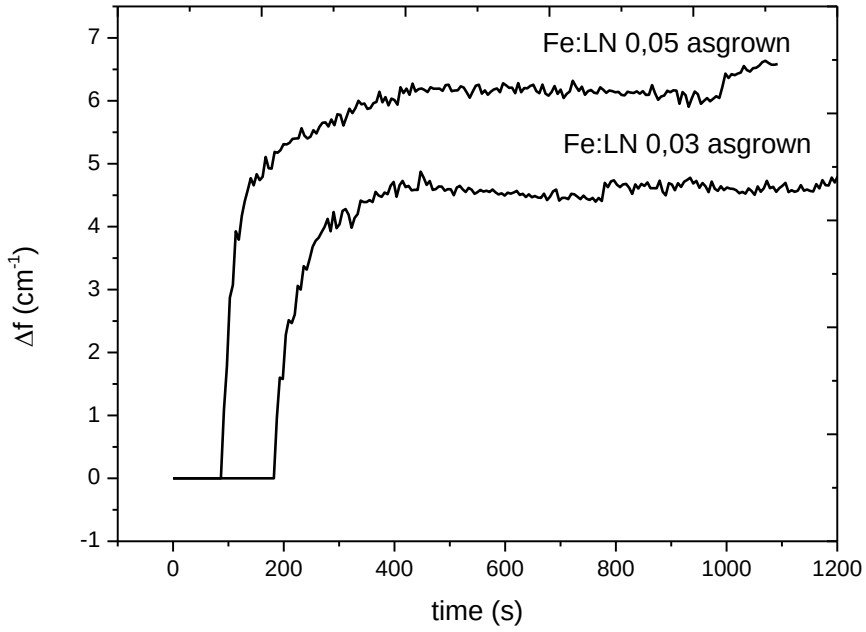

Figure IV. 29 *-Time evolution of the frequency shift of activated $A_1[TO_4]^*$ in the configuration X(YZ)X, 0.03mol and 0.05mol Fe doped asgrown samples are presented*

In addition the shift is sensitive to the concentration of Fe and to the reduction degree of the samples as well (figures IV.30 and IV.31).

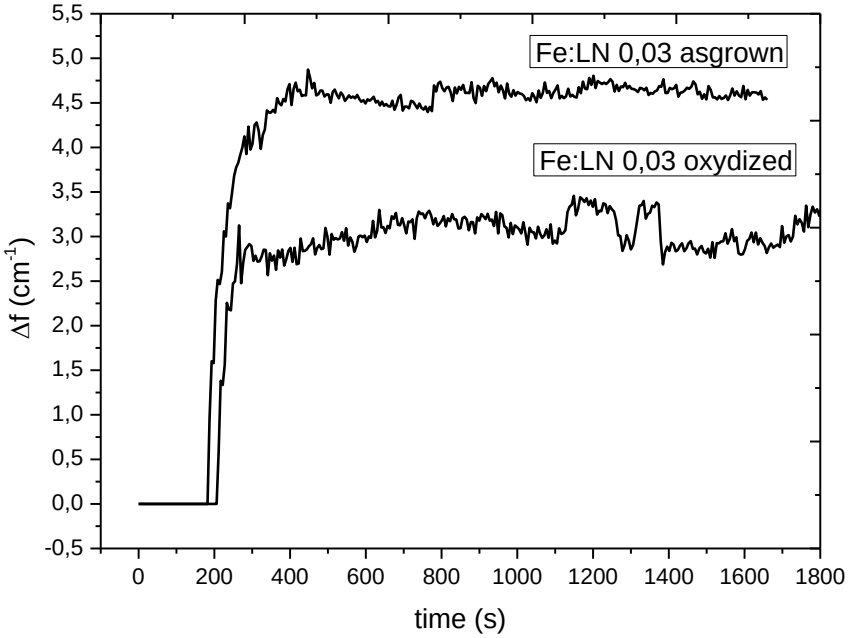

Figure IV. 30*-Time evolution of the frequency shift of activated $A_1[TO_4]^*$ in the configuration X(YZ)X, 0.03mol Fe doped asgrown and oxidized samples are presented*

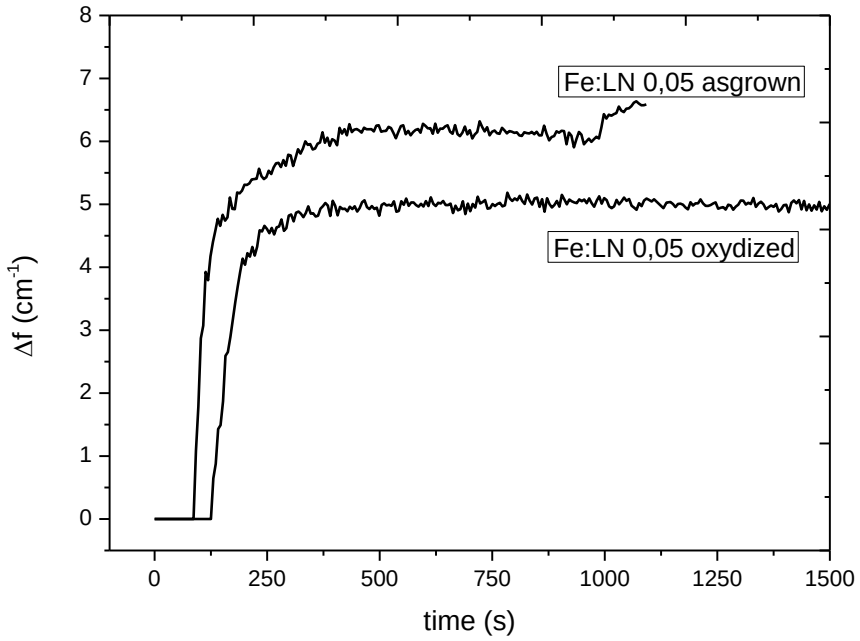

Figure IV. 31 *-Time evolution of the frequency shift of activated $A_1[TO_4]^*$ in the configuration X(YZ)X, 0.05mol Fe doped asgrown and oxidized samples are presented*

It has to be mentioned that the frequency shifts have the values between 3 and 6.5cm^{-1} in a contrast with a backscattering case where the frequency shift was between 1 and 1.4cm^{-1}.

The activation of A_1[TO] modes occurs with time. It is thus interesting to exploit the intensity dependence with time in order to have an idea about the time constant. In figure IV.32 the integrated intensity ratio between activated $A_1[TO_4]^*$ and expected $E[TO_8]$ is plotted. As one can see the time required for detecting the activation of A_1[TO] modes is less for the as grown sample comparing to the oxidized one. The time of saturation of the ratio is nearly the same for both samples. In addition it is important to mention that the ratio is higher for the asgrown sample comparing to the oxidized one. The same behavior is detected for the samples with 0.05 mol% of Fe.

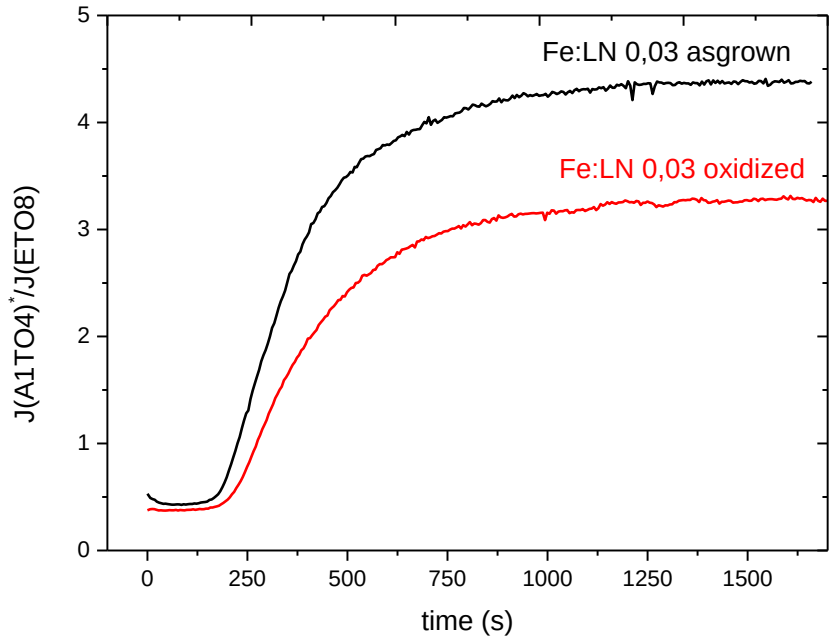

***Figure IV. 32**-The ratio between integrated intensity of activated $A_1[TO_4]^*$ and expected $E[TO_8]$ in the X(YZ)X configuration. Fe:LN 0.03 asgrown and oxidized samples are presented.*

Summarizing all the results above we can conclude that the frequency shift of the forbidden $A_1[TO_4]$ is originated by the strain effect due to photorefractive space charge field and the piezoelectric properties of Fe doped LN samples as for the case of backscattering discussed above. The frequency shifts are much higher in the forward scattering case as the beam traverses the sample which is not the case of the backscattering case where the measured volume and so the induced strain is much smaller.

IV.IV.3 – Interpretation

One – center model analysis

The above reported analysis indicates the photorefractive space charge field as the possible origin of an elastic strain through the reverse piezoelectric effect, just as the same field induces a change in the optical properties through the electro optic effect. Raman spectroscopy is sensitive to strain changes so that the Raman frequency change during time exhibits some typical features of the photorefractive phenomena.

For sake of simplicity, in this first analysis we will approximate the illumination as uniform inside the spot area, with an average intensity given by the beam power divided by

the spot area. Of course this is a crude approximation but allows capturing the essential features of the phenomenon using simple mathematics. In this case, according to the well – known one – center model for photorefractive phenomena in Fe:LN [6], the space charge field should evolve following a saturated exponential law:

$$E(t) = E_{sat}\left[1 - \exp\left(-\frac{t}{\tau}\right)\right]. \quad \text{(IV.1)}$$

The parameter E_{sat} is proportional to the concentration of Fe^{3+} ions [7] according to the formula:

$$E_{sat} = \frac{\kappa_{ph} h\nu r}{\mu e}[Fe^{3+}] \quad \text{(IV.2)}$$

where κ_{ph} is the Glass constant, $h\nu$ the photon energy, r the recombination rate, μ is the mobility of light induced charge carriers and e the elementary charge. The expected value of the proportionality constant in eq. (2) is of the order of 10^{-17} - 10^{-18} Vm^2 [6]. On the other hand, the time constant τ is given by:

$$\tau = \frac{\varepsilon\varepsilon_0}{\sigma_{PC}} \quad \text{(IV.3)}$$

where σ_{PC} is the material photoconductivity if the dark conductivity of the sample was neglected.

According to experiments performed under applied electric field, $\Delta f(t) \approx sE(t)$ where $s = 0.5x10^{-7} cm^{-1}\frac{m}{V}$ was estimated for the $A_1[TO_4]$ mode. Using this value and assuming for the moment that the space charge field is the only origin of the observed shifts, we may use our data to obtain the time evolution of the field amplitude in the different samples. According to this view, the time evolution of the Raman frequency shift of the $A_1[TO_4]$ line was first converted in the space charge amplitude using the constant s and subsequently fitted using equation (IV.1). The E_{sat} values were obtained for back and forward scattering frequency shifts and are shown in the figs. IV.33 and IV.34.

The space charge field value in backscattering is one order of magnitude less than the one in forward scattering. As the photorefractive space charge field depends on the absorption

coefficient, so the difference in values in backward and forward scatterings is explained by the difference of wavelengths used in both cases

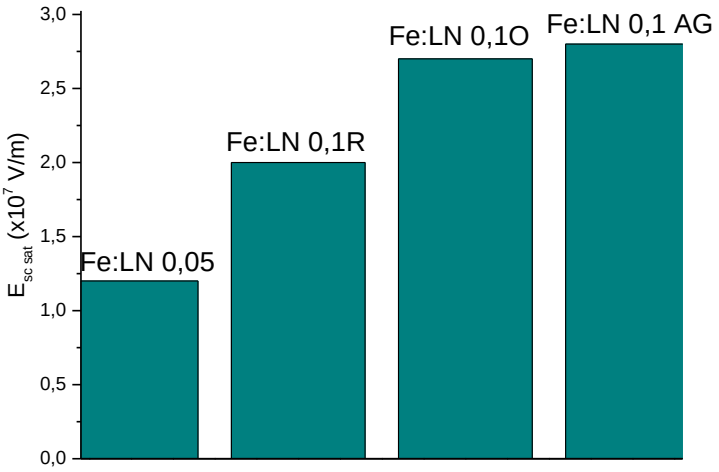

***Figure IV. 33**–Saturation value of the space charge field in backscattering determined by converting the shift of the Raman frequency to space charge field and subsequent fitting with eq. (IV.1)*

As on can see the space charge field value is higher for the reduced sample comparing to the oxidized and asgrown, this is due to the difference of concentration of Fe^{3+} (table IV.2) in samples, as the space the saturation value of space charge field is proportional to Fe^{3+}.

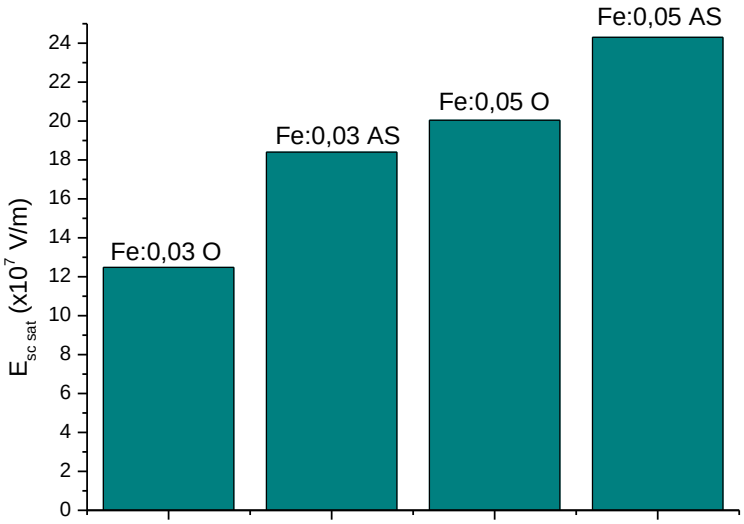

***Figure IV. 34**–Saturation value of the space charge field in forward scattering determined by converting the shift in the Raman frequency in space charge field and subsequent fitting with eq. (IV.1)*

IV.V – Conclusion

The photorefractive effect in Fe doped LN crystals can lead to some changes in Raman spectra and so can be characterized by it. One of the results of the photorefractive phenomenon is the defocusing of the beam after interaction with a photorefractive LN crystal which can lead to significant changes in Raman spectra. It was shown that the defocusing of the beam leads to the activation of forbidden Raman lines of other symmetry and quasi-modes as well. Activations are due to the changing of the plane of wave vector and are originated by the defocusing of the beam.

In the second part of the chapter it was shown that there is a frequency shift of some Raman lines with time in back and forward scattering spectra. The $A_1[TO_4]$ line was analyzed. The frequency shift is due the piezoelectric strain and is originated by the photo-induced space charge field. Using a calibration value the space charge field saturation values can be calculated. It is shown indeed that the space charge values are higher in forward scattering results.

IV.VI – References

[1] X. Yang, G. Lan, B. Li, H. Wang "*Raman Spectra and Directional Dispersion in $LiNbO_3$ and $LiTaO_3$"* phys. stat. sol. (b) 141, 287 (1987)

[2] R. Grousson, M. Henry, S. Mallick, and S. L. Xu, J. Appl. Phys. 54, 3012 (1983)

[3] F.S.Chen *"Optically induced change of refractive indices in LiNbO3 and LiTaO3*", J. of Applied Physics 40, 3389 (1969)

[4] A. M. Glass, D. von der Linde, T. J. Negran „High-voltage bulk photovoltaic effect and the photorefractive process in LiNbO3" Appl. Phys. Letters 25, 233 (1974)

[5] B.G.Kim, B.K. Rhee "*Determination of photovoltaic constant and photoconductivity in LiNbO3:Fe using Maker fringes"* Optics Communications 198, 193 (2001)

[6] P. Gunter and J. P. Huignard, "*Photorefractive Materials and their Applications 1: Basic effects"* Springer-Verlag, Berlin, 426 (2006)

[7] T. Volk and M. Wohlecke, "Lithium Niobate: Defects, Photorefracion, and Ferroelectric Switching" Springer, Berlin, 264 (2008)

Conclusion

We have investigated by Raman spectroscopy the different and successive effects caused by photorefractivity in LN crystal, and especially Fe doped LN sample. Results were compared with data on undoped LN and on Zr doped crystals as well, which are considered as optical damage resistive crystals.

At first, the influence of the polarization on the Raman spectra of LN were studied and compared with those expected by selection rules. It was shown that the spectra are strongly sensitive to the polarization direction and that obtained lines are in agreement with Raman selection rules. We establish a nearly complete table of the frequency of all A_1 and E modes, for TO and LO components It was seen as well that a small misorientation of the sample or polarizers can lead to the presence of leakages of other symmetry. It is shown indeed that the asymmetry is strongly reduced after dividing the Raman intensity by the population factor $n(\omega) + 1$associated with first-order Stokes scattering. This effect is particularly large for low-frequency phonon lines. The powder of congruent LN was measured as well and it was shown that Raman spectra are insensitive to the polarization choice (crossed or parallel polarizers). In addition, it was shown that both spectra are exactly similar to the non-polarized spectrum. In order to investigate the resistance to photorefractivity, Zr doped LN samples with different Zr content were studied by Raman spectroscopy. The frequency changes of Raman lines between samples as obtained by fitting procedure are quite small (1 cm^{-1}). The additional statistical treatment was applied on same spectra (chemometrics). We showed that this method provides the frequency shift behavior for each mode and each sample and it is in agreement with those obtained by classical fitting procedure. Utilizing Raman technique and chemometrics method the optical damage threshold of Zr doped LN crystals was determined and is near 2mol%, which is in agreement with results reported in literature obtained by other techniques. The site occupation of Zr ions was interpreted. It was shown that the Principal Component Analysis (PCA) can be used in order to help to determine the threshold. These results provide a possibility to use the PCA to derive the relative change in the spectra among many samples and to deduce a hierarchy of these samples using the classical fitting procedure.

For investigations of the influence of the photorefractive effect on the Raman spectra, Fe doped samples were used performing time dependence Raman measurements in back- and forward- scatterings. It was shown that the selection rules do not completely hold in forward scattering and forbidden lines of other symmetries and quasi-modes were detected. This is

explained by defocusing of the scattered beam linked to photorefractive effect of the Fe doped LN. In addition Raman lines show a frequency shift with time in backward and forward scatterings. It is shown that this shift is due to piezoelectric strain and is originated by photo-induced space charge field. The frequency shift of $A_1[TO_4]$ was analyzed. Performing a calibration experiments and utilizing the obtained calibration value between the frequency shift and the applied external electric field, space charge field values of each sample were calculated. The values are sensitive to the concentration of Fe in LN as expected. In addition it is shown that the space charge field is one order of magnitude higher in forward scattering comparing with this for backscattering which is due to the difference of the excitation wavelength. So photo-induced space charge field can be characterized utilizing Raman spectroscopy and can be observed by calculating the frequency shift of Raman lines.

Perspectives

Next step of the work is to give more quantitative view on obtained results. Thus several physical parameters can be deduced from the evaluation of the space charge field deduced from Raman data. Indeed the concentration of Fe^{3+} can be reduced from the saturation value of the space charge field as:

$$[Fe^{3+}] = \frac{\mu e}{\kappa_{ph} h\nu r} * \frac{1}{E_{sat}}$$

As well as using the time constant of space charge field we can obtain the photoconductivity values for each sample: $\boldsymbol{\sigma_{pc}} = \frac{\boldsymbol{\varepsilon \varepsilon_0}}{\boldsymbol{\tau}}$

For different configuration as a function on propagation and polarization directions we obtained different direction of defocusing. In addition it could be interesting to study the physical origins of the defocusing, specially to explain the difference of configurations X(YZ)X and X(ZY)X.

In forward Raman measurements for the configuration X(YY)X (Y(XX)Y) the activation of $A_1[TO]$ modes were detected and the integrated intensity of the $A_1[TO_4]^*$ activated has a saturated form with time (figure P.1). It will be interesting to exploit these results and find out

the link with photorefractive phenomenon and use new technic in order to characterize photorefractive properties.

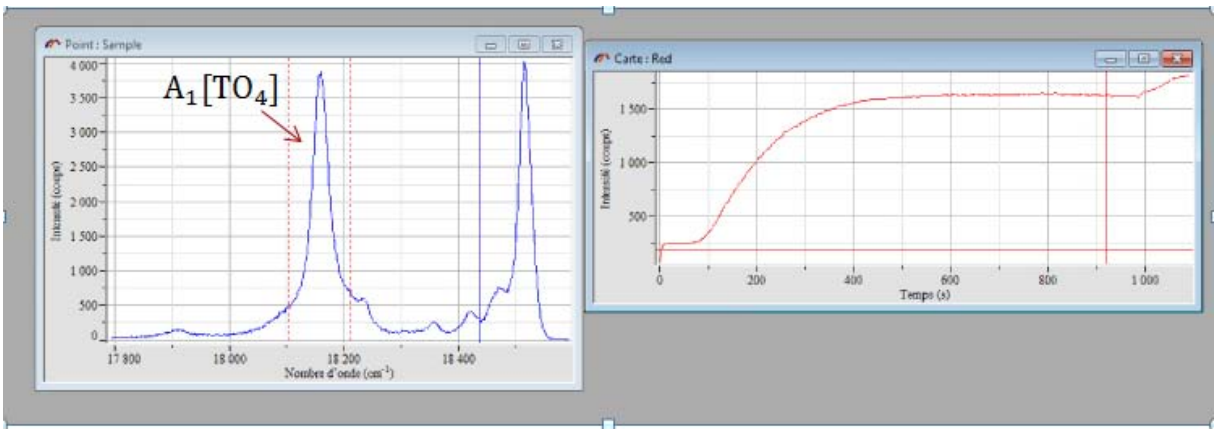

Figure P. 1 *- Activated $A_1[TO_4]^*$ and it's integrated intensity as a function on time. For the configuration X(ZZ)X*

At last, dopants relevant for laser emission after cations could be interesting to be studied. Thus doping LN with Cr and Ho ions leads to obtain a laser crystal, so it will be interesting to study them by Raman spectroscopy in order to investigate non-linear properties and the influence of Cr and Ho ions on the structure of LN.

Appendix A

Temperature dependence of Raman scattering and anharmonic properties in $LiNbO_3$

A.I – Introduction

Here we study in more detail the temperature dependence of modes A_1 polarized along the FE c axis but also the optical phonons E corresponding to ionic motions in the plane normal to c. At first the different origins of asymmetry in line shapes are considered before deriving from the fitting procedure the temperature dependences of phonon-frequency and -damping. Our measurements were recorded from low temperature (93 K) to establish a clear assignment of all detected lines, up to very high temperature (673 K), but much below T_c.

Frequency and damping of each optical phonon were then plotted as function of temperature and their dependences were analyzed in terms of contributions coming from normal volume and anharmonic effects.

A.II – Experimental

Raman measurements were performed with the 633 nm exciting line of a He–Ne laser at a power of 50 mW.. LinKam LTS420 set up was used with a temperature controller within 2 K. According to C3v point group of LN, 4 Raman active phonons with A_1 symmetry and 9 Raman active phonons with E symmetry are expected. To detect A_1[TO] and E[TO] transverse optical (TO) phonons, Y(ZZ)Y and Y(ZX)Y backscattering configurations were used, respectively. These configurations are chosen because they allow in principle discrimination between the two phonon symmetries. Raman spectra recorded at various temperatures within both scattering configurations are shown in figs. A.1 and A.2.

At low temperature Fig. A.1 displays the four lines corresponding to the expected A_1[TO] phonons whereas Fig. A.2 exhibits seven peaks for E[TO] phonons. A clear assignment of different Raman lines to first-order phonons was achieved at low temperature (93 K) in both spectra so that their dependences on T can be studied without ambiguity. As expected Raman peaks broaden with increasing temperature so that several peaks are not longer well detected at very high temperature. Moreover second-order scattering is enhanced at high temperature and causes additional broadening. But its effect is relatively small in the temperature range under study. At temperature above 800 K its influence becomes dominant and the Raman spectrum consists only into very wide bands [2] leading to some ambiguous interpretations of the spectra

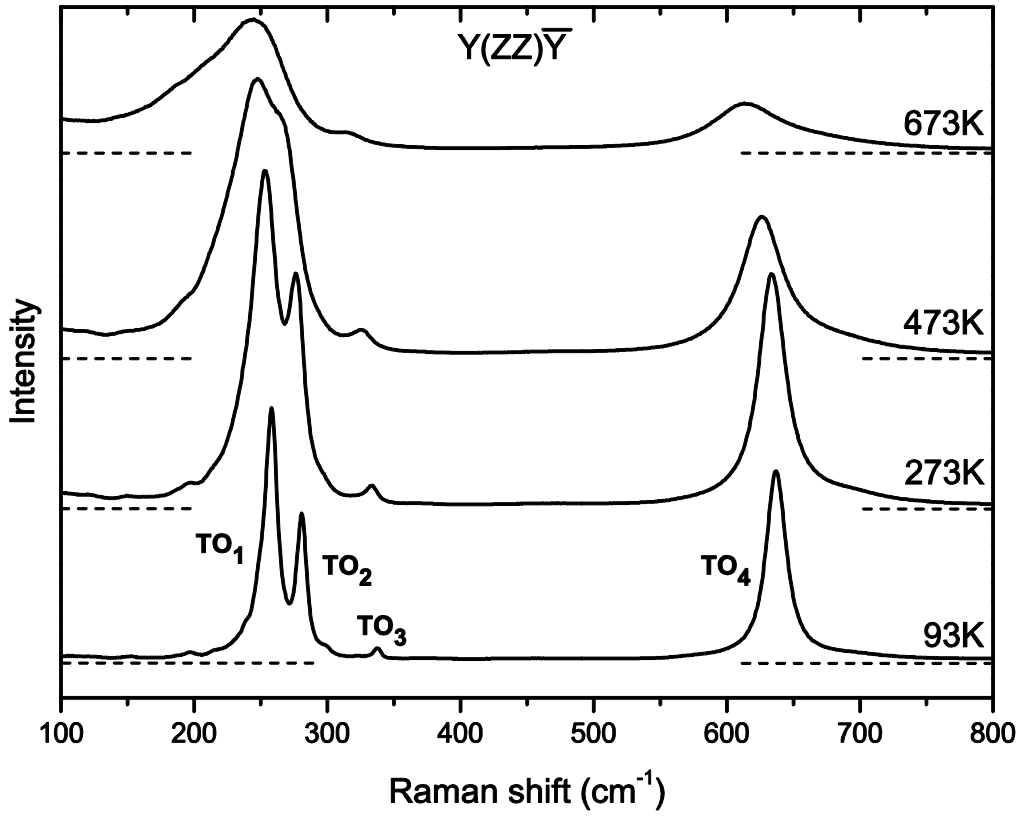

Figure A.1 *– A_1[TO] Raman spectrum of LN recorded at several temperatures*

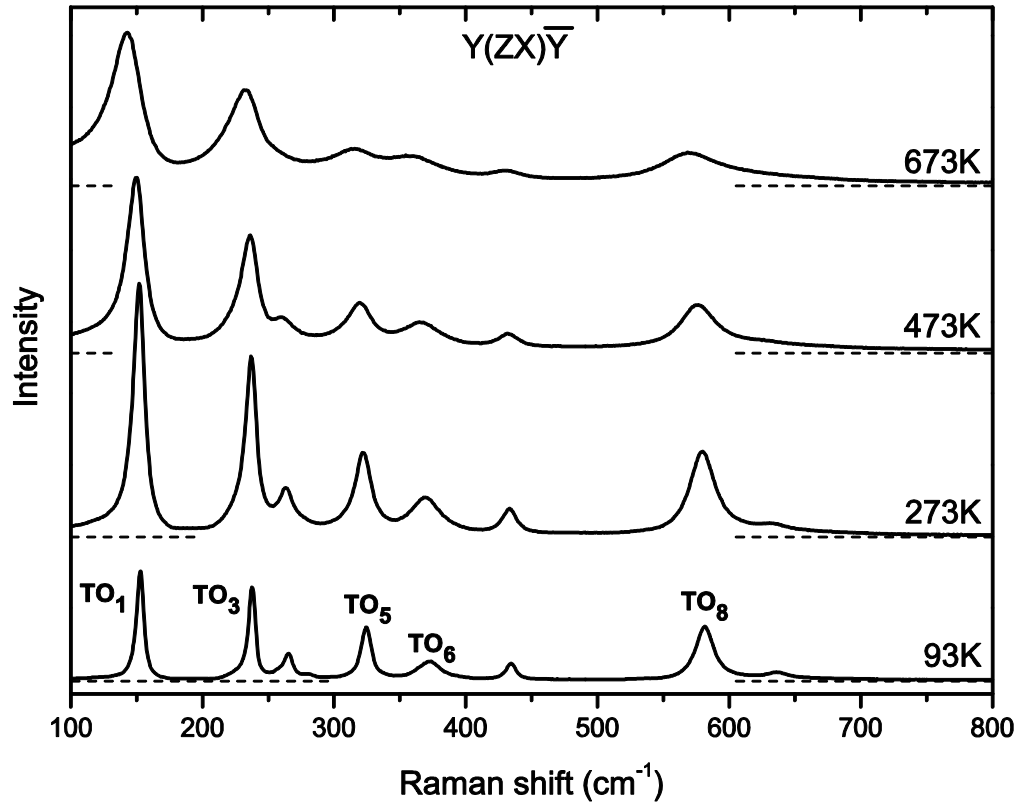

Figure A.2 *– E[TO] Raman spectrum of LN recorded at several temperatures*

A. III – Results

Figure A.3 shows the lowest frequency E[TO_1] Raman spectrum recorded at different temperatures. A clear down-shift of the maximum and increase of the width is detected on heating for this peak.

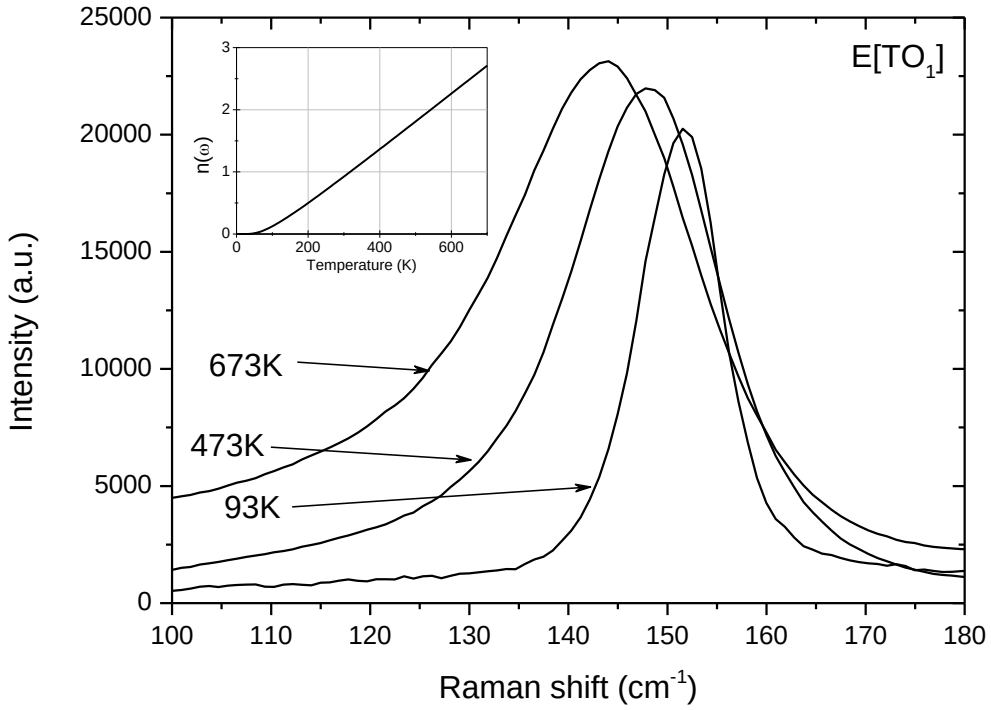

Figure A.3 *– Lowest-frequency E[TO_1] Raman spectra recorded at different temperatures.* ***Inset****: temperature dependence of Bose-Einstein population factor for ω(E[TO_1]) at room temperature*

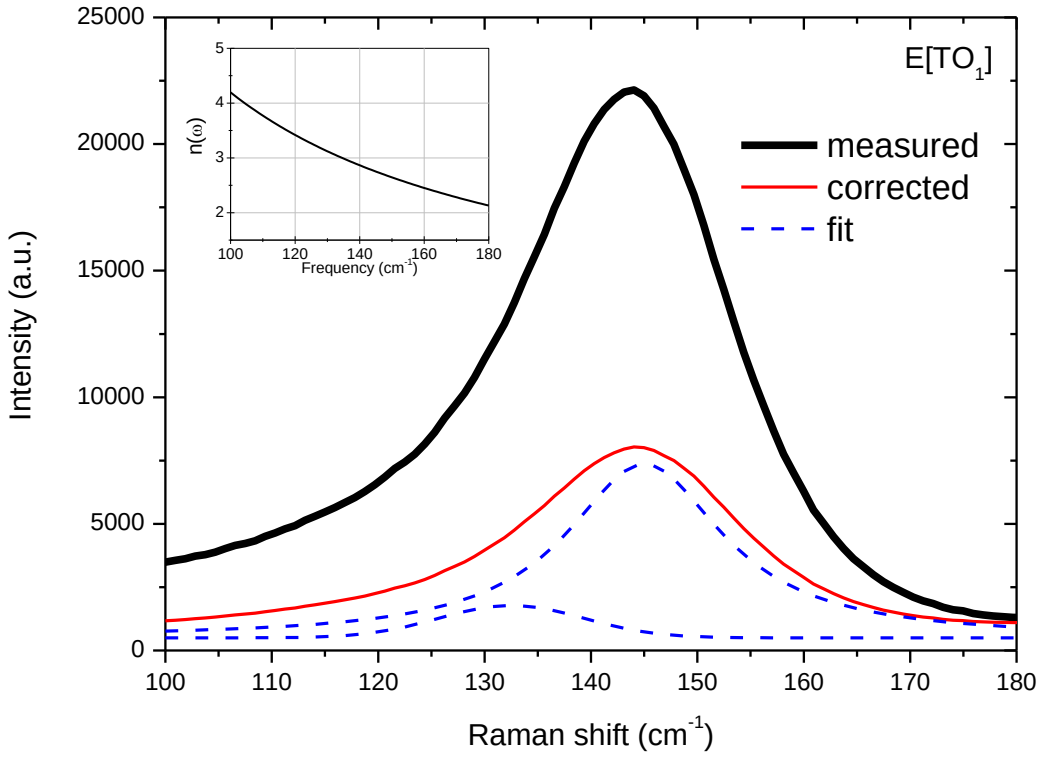

Figure A.4 *– Lowest frequency E[TO_1] Raman spectrum at 673K. This spectrum is then divided by the Bose-Einstein population factor (reported in the inset) and finally fitted to two Lorentzian functions*

As a consequence, the line shape Raman profile has to be carefully analyzed to distinguish between the different origins of asymmetry: the population factor, the occurrence of peak with a different symmetry and the presence of second-order bands. Our Raman spectra, after correction by the population factor, are fitted to a sum of lorentzians. The frequency and the damping of each A1[TO] and E[TO] phonons are derived from this fit so that their dependences on temperature are plotted in Figs. A.5 and A.6. The changes with temperature are much larger for A1 phonons than E modes. This is true for frequency and damping as well. The frequency decrease is strong and nearly linear with temperature for A1 mode in the whole temperature range whereas the frequency change is much smaller in E phonons and is observed above 400 K only (Fig. A.7). The damping of A_1[TO] exhibits a large and rapid increase with temperature showing a deviation from the linear behavior above 400 K whereas the damping increase of E phonon is nearly linear with T. The T dependences

of both frequency and damping of each A1 and E phonon are interpreted and discussed below from a model accounting for different contributions and described here.

A. IV – Anharmonic behavior : model and calculations

The temperature dependence of j-th optical phonon frequency results from the combination of various effects as:

$$\omega_j(T) = \omega_j(0) + \Delta\omega_j(ent) + \Delta\omega_j(anh) \quad \text{(A.1)}$$

where $\omega_j(0)$ is the frequency value assumed at 0 K, $\Delta\omega_j(ent)$ and $\Delta\omega_j(anh)$ are the shifts due to the entropy driven part of the volume expansion and anharmonic effects, respectively. The first shift results from entropic part of volume or thermal expansion effect and can be expressed as:

$$\Delta\omega_j(ent) = \omega_j(0) g_j \int_0^T \alpha(T')dT' \quad \text{(A.2)}$$

where g_j is the Gruneisen parameter ($-\frac{V}{\omega_j}\frac{\partial\omega}{\partial V}$, with V cell volume) and α is the thermal expansion coefficient of the cell.

The linear thermal expansion coefficient relates the change in a material's linear dimensions to a change in temperature. It is the fractional change in length per degree of temperature change. Ignoring pressure, we may write:

$$\propto_L = \frac{1}{L}\frac{dL}{dT} \quad \text{(A.3)}$$

where *L* is the linear dimension (e.g. length) and *dL / dT* is the rate of change of that linear dimension per unit change in temperature. The change in the linear dimension can be estimated to be:

$$\frac{\Delta L}{L} = \propto_L \Delta T \quad \text{(A.4)}$$

For congruent LN the thermal expansion coefficients are:

$$\alpha_a = 15x10^{-6}/^0C$$

$$\alpha_c = 7.5x10^{-6}/^0C$$

The relative change of the frequency with temperature is assumed to be linear as:

$$\frac{d\omega_i}{\omega_i} = KdT \qquad \text{(A.5)}$$

The Gruneisen parameter g is expressed as:

$$g = -\frac{V}{\omega_i}\frac{\partial \omega_i}{\partial V} \qquad \text{(A.6)}$$

The physical meaning of the parameter can also be extended by combining thermodynamics with a reasonable microphysics model for the vibrating atoms within a crystal. When the restoring force acting on an atom displaced from its equilibrium position is linear in the atom's displacement, the frequencies ωi of individual phonons do not depend on the volume of the crystal or on the presence of other phonons, and the thermal expansion (and thus γ) is zero. When the restoring force is non-linear in the displacement, the phonon frequencies ωi change with the volume V. The Gruneisen parameter of an individual vibrational mode i can then be defined as (the negative of) the logarithmic derivative of the corresponding frequency ω_i.

$$V = a^2c$$

$$dV = 2acda + a^2dc$$

$$\frac{dV}{V} = \frac{2acda + a^2dc}{a^2c} = \frac{2da}{a} + \frac{dc}{c}$$

From the equation of Gruneisen parameter (A.6):

$$\frac{\partial \omega_i}{\omega_i} = -g\frac{dV}{V} = -g\left(\frac{2da}{a} + \frac{dc}{c}\right) = -g\left(\frac{2\alpha_a}{K}\frac{d\omega_i}{\omega_i} + \frac{\alpha_c}{K}\frac{d\omega_i}{\omega_i}\right) = -g\frac{(2\alpha_a + \alpha_c)}{K}\frac{d\omega_i}{\omega_i}$$

So:

$$\gamma = -\frac{K}{2\alpha_a + \alpha_c} \qquad \text{(A.7)}$$

As α_a and α_c are linear within the temperature range under study [3] we have:

$$\Delta\omega_j(ent) = \omega_j(0)g_j\alpha T = \omega_j(0)K_jT \qquad \text{(A.8)}$$

where $K = g_j\alpha$ is a parameter for each j mode. The anharmonic term in the equation (A.1) is assuming to come from the third-order anharmonic potential [4,5]. Within this model the TO

phonon decays into two phonons of lower frequency [5, 6]. Due to momentum conservation, these phonons have opposite wave vectors and belong to the same mode, and due to energy conservation their frequencies equal to half of the considered TO phonons [6–8].

Within this assumption the anharmonic term can be written as:

$$\Delta\omega_j(anh) = -D\left\{1 + 2n\left(\frac{\omega_j(0)}{2}\right)\right\} \qquad \text{(A.9)}$$

where D is a coefficient depending on the third-order process and n is the Bose-Einstein population factor. Therefore according to equation (A.1) the temperature dependence of each optical phonon frequency can be fitted to (the index j is hereafter omitted)

$$\omega(T) = \omega(O) + \omega(0)KT - D\left\{1 + 2n\left(\frac{\omega_j(0)}{2}\right)\right\} \qquad \text{(A.10)}$$

with only two adjusted parameters $\omega(0)$ and D. $K = g\alpha$ is a constant for each phonon as deduced from Gruneisen and thermal dilatation coefficients issued from literature [2,3,9]. Due to the quasi linear T dependence of n(ω) (see insert of Fig. A.3) a linear change of phonon frequency is expected with T. It is to be stressed that both terms (entropic and anharmonic) are negative (note that g and therefore K is negative) and have to contribute to phonon frequency diminishing.

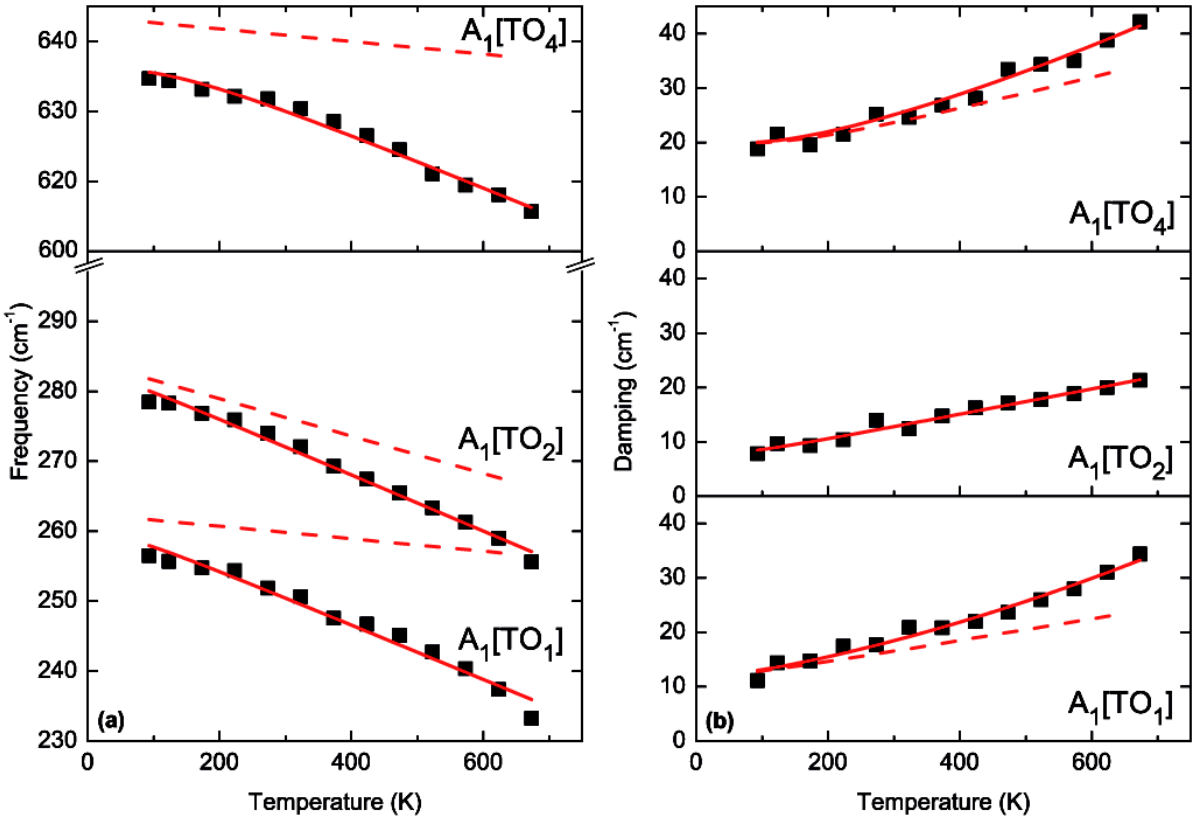

Figure A.5 *– Temperature dependence of the frequency (part a) and damping (part b) of $A_1[TO]$ phonons in LN. Dots are experimental data and continuous lines are fits to equations 5 and 6, respectively. Dashed lines correspond to calculations when the last term in these equations is neglected*

The temperature change of the phonon damping can be expressed and fitted to

$$\Delta\gamma(T) = \gamma(0) + B\left\{1 + 2n\left(\frac{\omega(0)}{2}\right)\right\} + CT^2 \quad \text{(A.11)}$$

where the first term corresponds to the residual linewidth including spectrometer resolution. Due to the effects other than the anharmonicity, its value at the O K limit depends on the defects or impurities only. The second and third terms come from 3- and 4- phonon processes via parameters B and C, respectively. By contrast to the frequency dependence, in which only the term coming from the third-order potential is needed for fitting (see equation A.10), here for the damping, the fourth potential introducing a quadric dependence is necessary to reproduce the temperature dependence especially at high temperature as shown below. Experimental T dependences of phonon frequency and damping are fitted to eqs A.10 and A.11 respectively.Results are reported in fig A.6 for A1 phonons and fig A.7 for E modes.

Only phonons for which the behavior can be unambiguously studied as function of T are reported. For E phonon frequency data are fitted in the range above 375 K since below this temperature the frequency is almost T independent (the change is about 1 cm^{-1} only). Fitted values of the parameters ω(0), D, γ(0), B and C are reported in Table A.1.

Modes	ω(273K) (cm^{-1})	G	K ($-10^{-6}K^{-1}$)	D (cm^{-1})	ω(0) (cm^{-1})	γ(273K) (cm^{-1})	γ(0) (cm^{-1})	B (cm^{-1})	C ($10^{-5}cm^{-1}K^{-1}$)
A1TO1	251.9	0.9	34	2.9	262.5	15.1	10.3	1.9	2.0
A1TO2	274	2.5	94	1.4	284.3	17.7	05.5	2.4	0.0
A1TO4	631.8	0.4	14	7.0	643.6	14.0	11.8	7.4	1.6
ETO1	151.4	1.3	49	0.8	159	08.3	07.1	0.2	1.4
ETO3	236.1	0.2	07	0.5	238.4	10.0	07.2	0.3	2.6
ETO5	321.2	1.1	43	0.1	324.6	13.1	11.3	0.0	4.2
ETO6	368.6	2.0	75	0.0	377.9	17.0	14.9	0.1	2.6
ETO8	578.4	0.8	30	1.5	587.2	17.4	04.4	8.9	0.0

Table A.1 *– Values of the parameters D, B, C, ω(0) and γ(0) deduced from the fits of experimental data to Eqs. A.10 and A.11. g is the Gruneisen parameter value given in literature [9] (except for $E[TO_6]$ where g is arbitrary fixed to 2). The experimental values of the frequency and damping at 273K are also reported for comparison with the respective fitted values at 0K*

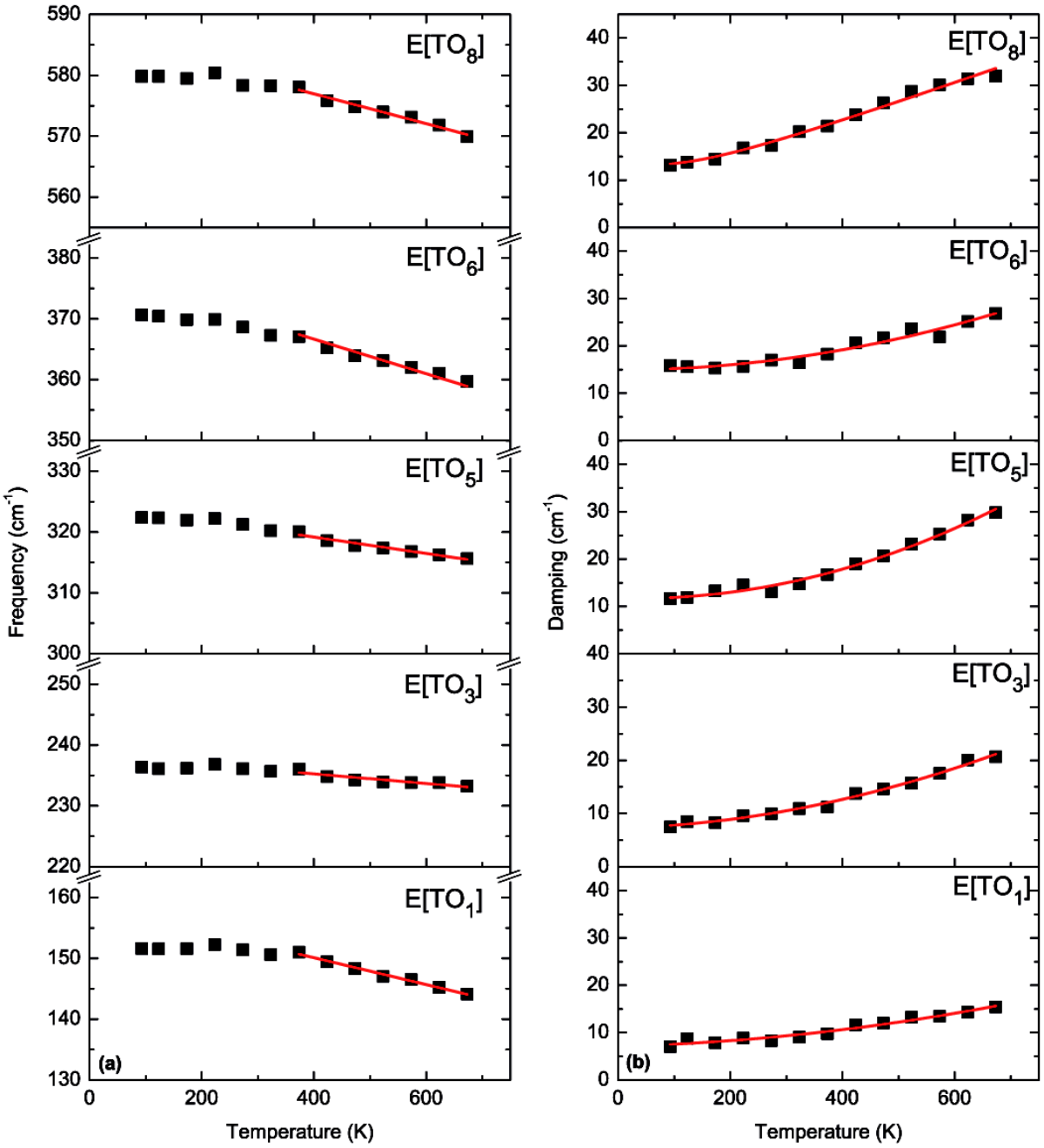

Figure A.6 *– Temperature dependence of the frequency (part a) and damping (part b) of E[TO] phonons in LN. Dots are experimental data and continuous lines are fits to equations A.10 and A.11, respectively*

A. V – Discussion and conclusion

As shown in figs. A.6 and A.7 a fairly good agreement is achieved between experimental data and calculations in temperature plots of both frequency and damping for all A1 and E phonons as well. This result is remarkable since obtained with a relatively simple model from two or three adjusted parameters for frequency and damping, respectively. It is to be mentioned that the value of the parameter $\omega(0)$ derived from fit of frequency plot is then introduced as one constant in the treatment of the T dependence of the damping.

Results (presented in Table A.1) pointed out that anharmonic parameters D and B related to third-order potential are very large for each A_1 phonon. By contrast these coefficients are small in all E[TO] phonons, except the E[TO_8] which shows values close to those of A1. The strong anharmonic contribution in A1 phonons is emphasized in Fig. A.6a showing the large difference in the dependence of frequency between the experimental data and the calculated plots if only the entropic term is considered in eq. A.10. This is especially observed in TO_1 and TO_4 whereas the entropic term is nearly sufficient to describe the T dependence of the A_1[TO_2] frequency. The fourth order-potential (parameter C) present in damping only has very small values in all E and A1 modes. This contribution is shown to increase with growing T, as seen in Fig. A.6.b.

Our results are consistent with ab initio calculations reported by Caciuc et al. [1]. From local-density approximation they computed total energy for different modes and they demonstrated a large anharmonicity of A_1[TO_1] and A_1[TO_4] phonons, while TO_2 and TO_3 modes (this last mode was not considered in our study) are nearly entropic. The origin of this strong anharmonic behaviour can be related to ionic motion pattern associated with the different modes. Thus TO1 is an out-ofphase motion of Nb and O ions along the z axis whereas the TO4 corresponds to a stretching motion of oxygen octahedra [10]. It is to be noted that a vibration similar to A_1[TO_4] is associated with E[TO_8] which was found in our study to be anharmonic as well. This large anharmonicity within ionic motions along the FE axis c is also in accordance with calculations of Inbar and Cohen [11], predicting large double well potentials for oxygen displacements towards Nb ions, in agreement with a main order–disorder character of the FE–PE phase transition.

A. VI – References

[1] V. Caciuc, A.V. Postnikov, G. Borstel, *"Ab initio structure and zone-center phonons in LiNbO3"* Phys. Rev. B 61, 8806 (2000)

[2] S.H. Yao, J.Y. Wang, H. Liu, T. Yan, D.H. Yu, Y.F. Chen "*Mechanism of the abnormal thermal expansion of nearly stoichiometric LiNbO3"* J. Cryst. Growth 318, 951 (2011)

[3] X. Xu, T. Chong, S. Solanki, X. Liang, S. Yuan "*Anisotropic thermal expansion of stoichiometric lithium niobate crystals growth along the normal direction of facets"* Opt. Mater. 26, 489 (2004)

[4] M. Balkanski, R.F. Wallis, E. Haro "*Anharmonic effects in light scattering due to optical phonons in silicon"* Phys. Rev. B 28, 1928 (1983)

[5] A.S. Pine, P.E. Tannenwald "*Temperature dependence of Raman linewidth and shift in α-quartz"* Phys. Rev. 178, 1424 (1969).

[6] A. Perakis, E. Sarantopoulou, Y.S. Raptis, C. Raptis " *Temperature dependence of Raman scattering and anharmonicity study of MgF2"* Phys. Rev. B 59, 775 (1999)

[7] J.F. Kong, W.Z. Shen, Q.X. Guo " *Raman-scattering probe of anharmonic effects dure to temperature and composition in InGaN"* Physica Status Solidi (B) 250, 329 (2013)

[8] P.G. Klemens "*Anharmonic decay of optical phonons »* Phys. Rev. 148, 845 (1966)

[9] A. Jayaraman, A.A. Ballman "*Effect of pressure on the Raman modes in LiNbO3 and LiTaO3*" J. Appl. Phys. 60, 1208 (1986)

[10] A.V. Postnikov, V. Caciuc, G. Borstel "*Structure optimization and frozen phonons in LiNbO3"* J. Phys. Chem. Solids 61, 295 (2000)

[11] I. Inbar, R.E. Cohen "*Comparison of the electronic structures and energetics of ferroelectric LiNbO3 and LiTaO3"* Phys. Rev. B 53, 1193 (1996).

Appendix B
Fitting procedure of Raman lines

Fitting procedure of Raman lines

In our work it was necessary to fit the Raman lines of the main part of obtained spectra. In order to fit the peaks we used the *Fityk 0.9.8* software. As a function we utilized the Lorentzian:

$$f(\omega, \omega_0, \gamma, I) = \left[\frac{\gamma^2}{(\omega-\omega_0)^2+\gamma^2}\right] xI \qquad \text{(B.1)}$$

After correcting the baseline of the spectra by the software and performing a single fit we observe 3 parameters: ω_0 which shows the position of the peak and corresponds to the frequency of the phonon, γ which is the linewidth and shows the phonon damping and I is the height of the line and shows the intensity.

In figure B.1 an example of the fitted spectra is presented:

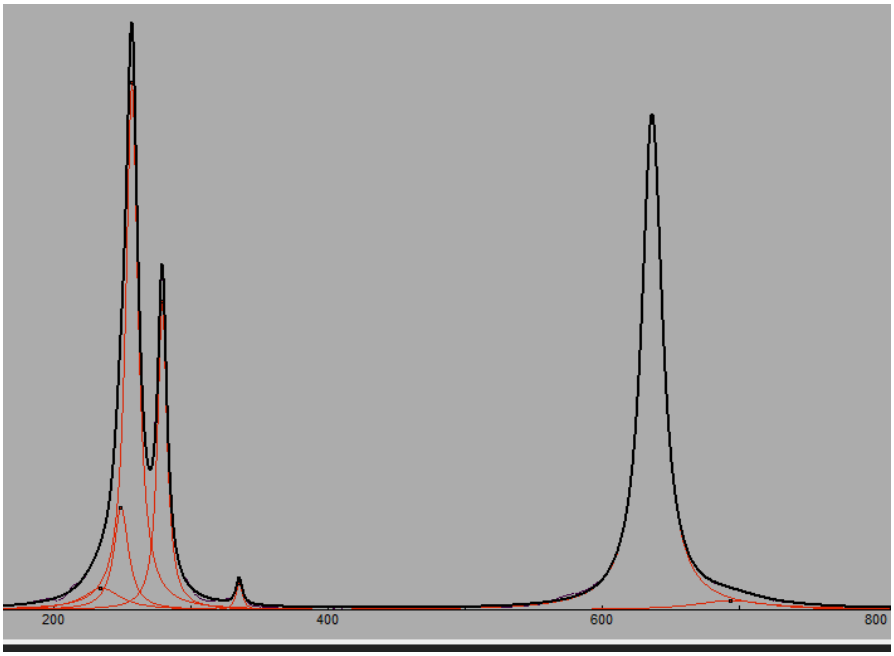

Figure B. 1 *– Fitted Raman spectra of congruent LN for Y(ZZ)Y configuration*

In the case of the presence of asymmetries of the peaks there is a necessity to use an additional peak or peaks in order to limit the error of the fit. In addition when we have a number of spectra to fit in order to have comparable results between them the additional peaks can be fixed with nearly same parameters for all fitted spectra, which was done for the fitting of Zr doped LN Raman spectra. Additional peaks were fixed by their positions and linewidths for all fitted spectra (in the figure, the additional peaks are near 220cm^{-1}, 240cm^{-1} and 700cm^{-1}).

Table of figures

List of tables